Monthly Notices
of the
ROYAL ASTRONOMICAL SOCIETY

MNRAS **483,** 70–118 (2019)
Advance Access publication 2018 October 31

doi:10.1093/mnras/sty2942

A catalogue of Galactic supernova remnants in the far-infrared: revealing ejecta dust in pulsar wind nebulae

H. Chawner,[1]★ K. Marsh,[1] M. Matsuura,[1]★ H. L. Gomez,[1]★ P. Cigan,[1] I. De Looze,[2] M. J. Barlow,[2] L. Dunne,[1] A. Noriega-Crespo[3] and J. Rho[4,5]

[1]*School of Physics and Astronomy, Cardiff University, Queens Buildings, The Parade, Cardiff, CF24 3AA, UK*
[2]*Department of Physics and Astronomy, University College London, Gower Street, London WC1E 6BT, UK*
[3]*Space Telescope Science Institute, 3700 San Martin Drive, Baltimore, MD 21218, USA*
[4]*SETI Institute, 189 N. Bernardo Ave, Suite 100, Mountain View, CA 94043, USA*
[5]*SOFIA Science Center, NASA Ames Research Center, MS 232, Moffett Field, CA 94035, USA*

Accepted 2018 October 26. Received 2018 October 26; in original form 2018 April 11

ABSTRACT

We search for far-infrared counterparts of known supernova remnants (SNRs) in the Galactic plane ($10^\circ < |l| < 60^\circ$) at 70–500 μm using the *Herschel* Infrared Galactic Plane Survey (Hi-GAL). Of 71 sources studied, we find that 29 (41 per cent) SNRs have a clear FIR detection of dust emission associated with the SNR. Dust from 8 of these is in the central region, and 4 indicate pulsar wind nebulae (PWNe) heated ejecta dust. A further 23 have dust emission in the outer shell structures which is potentially related to swept-up material. Many Galactic SNe have dust signatures but we are biased towards detecting ejecta dust in young remnants and those with a heating source (shock or PWN). We estimate the dust temperature and mass contained within three PWNe, G11.2–0.3, G21.5–0.9, and G29.7–0.3, using modified blackbody fits. To more rigorously analyse the dust properties at various temperatures and dust emissivity index β, we use point process mapping (PPMAP). We find significant quantities of cool dust (at 20–40 K) with dust masses of $M_\mathrm{d} = 0.34 \pm 0.14\,\mathrm{M}_\odot$, $M_\mathrm{d} = 0.29 \pm 0.08\,\mathrm{M}_\odot$, and $M_\mathrm{d} = 0.51 \pm 0.13\,\mathrm{M}_\odot$ for G11.2–0.3, G21.5–0.9, and G29.7–0.3, respectively. We derive the dust emissivity index for the PWN ejecta dust in G21.5–0.3 to be $\beta = 1.4 \pm 0.5$ compared to dust in the surrounding medium where $\beta = 1.8 \pm 0.1$.

Key words: stars – ISM: supernova remnants – infrared: ISM – submillimetre: ISM.

1 INTRODUCTION

Historically, evolved stars have been considered the main source of dust in galaxies, especially Asymptotic Giant Branch stars (low- and intermediate-mass stars in the final stages of evolution) (e.g. Dwek 1998). However, the injection rate from evolved stars falls short by up to an order of magnitude if they are to explain the mass of dust which we observe in the interstellar medium (ISM) of galaxies (e.g. Morgan & Edmunds 2003; Matsuura et al. 2009). This is especially problematic in dusty high redshift galaxies for which the lifetime of such stars is close to, or longer than, the dust production timescale (Morgan & Edmunds 2003; Dwek, Galliano & Jones 2007; Michałowski et al. 2010; Gall, Hjorth & Andersen 2011; Rowlands et al. 2014; Mancini et al. 2015; Michałowski 2015). There is a long-standing debate as to whether dust formed in supernovae (SNe) may survive to make up this shortfall. SNe provide ideal conditions for dust formation as there is an abundance of heavy elements in the ejecta and the temperature drops quickly with expansion. Models suggest that core-collapse SNe can quickly produce substantial amounts of heavy materials (Todini & Ferrara 2001; Nozawa et al. 2003).

One unresolved question is how much of the ejecta dust will survive the harsh environment of an SNR. Simulations of dust destruction in the ISM and SNe suggest that sputtering is responsible for a large amount of dust destruction (e.g. Jones et al. 1997; Bocchio, Jones & Slavin 2014; Micelotta, Dwek & Slavin 2016) and destruction rates of up to $3.7 \times 10^{-2}\,\mathrm{M}_\odot\,\mathrm{yr}^{-1}$ have been estimated for SNRs in the Magellanic Clouds (Temim et al. 2015). Nevertheless, the mass of dust that survives destructive processes is dependent on a number of factors including the grain size (Nozawa et al. 2007), the SN type (e.g. Kozasa et al. 2009; Nozawa et al. 2010; Biscaro & Cherchneff 2016), and the clumpiness of the ejecta (e.g. Biscaro & Cherchneff 2016). Observations of dust in a range of SNRs are therefore crucial in confirming whether dust can survive destructive processes and, if so, how much dust is injected into the ISM.

Along with line and continuum emission from gas, infrared dust emission is thought to be one of the key cooling processes of super-

★ E-mail: chawnerhs@cardiff.ac.uk (HC); matsuuram@cardiff.ac.uk (MM); gomezh@cardiff.ac.uk (HLG)

nova remnants (SNRs) (Ostriker & Silk 1973; Draine 1981; Dwek 1987). Infrared emission contains important information about the dust within an SNR and can help us to determine whether ejecta dust can survive to be injected into the ISM. However, confusion with the ISM makes SNRs extremely difficult to detect in the Galactic plane and was a problem for surveys using the Infrared Astronomical Satellite (*IRAS*), which observed at 12–100 μm (Arendt 1989; Saken, Fesen & MIchael 1992). Infrared surveys of SNRs in the Milky Way were completed by Reach et al. (2006, hereafter R06) and Pinheiro Goncalves et al. (2011, hereafter PG11) using *Spitzer* IRAC (3.6–8 μm) and MIPS (24 and 70 μm) data, respectively. However, shorter infrared wavelengths may miss any cool dust component that might exist in SNRs and therefore we may underestimate the amount of dust formed after the SN explosion (e.g. Barlow et al. 2010).

With the advent of *Herschel Space Observatory* (Pilbratt et al. 2010), massive quantities of colder (<50 K) SN ejecta dust have been detected in a handful of core collapse remnants. *Herschel* detected filaments of supernova ejecta dust in the Crab Nebula at temperatures of 27–35 K with a mass of up to 0.47 $M_\odot$ (Gomez et al. 2012b; Owen & Barlow 2015), an order of magnitude larger than that estimated using *Spitzer* data up to 70 μm (Temim et al. 2012). The filamentary dust is likely heated by non-thermal, synchrotron radiation from the pulsar wind nebula (PWN) (e.g. Davidson & Fesen 1985; Macalpine & Satterfield 2008).

Similarly to the Crab Nebula, the PWN G54.1+0.3 was discovered to have a shell of SN-condensed dust. Analysis of the 15–870 μm emission from *Herschel*, *Spitzer* and APEX suggests a minimum total dust mass of 0.07–1.1 $M_\odot$ (Temim et al. 2017; Rho et al. 2018), thought to be heated by the PWN or nearby cluster stars.

Dust in the O-rich SNR Cassiopeia A was discovered using *IRAS* and the Infrared Space Observatory finding a warm dust mass of 10^{-4}–10^{-2} $M_\odot$ (e.g. Braun, Gull & Perley 1987; Dwek 1987; Arendt, Dwek & Moseley 1999; Douvion, Lagage & Pantin 2001). Orders of magnitude more dust at colder temperatures were then detected by Dunne et al. (2003, 2009), with later *Herschel* and *Spitzer* data showing dust in two regions: a warm dust component in the outer, reverse shock region, and a central region of cold (<25 K), unshocked ejecta dust (Barlow et al. 2010). The total dust mass is as high as 0.3–1.0 $M_\odot$ (Dunne et al. 2003; Rho et al. 2008; Barlow et al. 2010; De Looze et al. 2017). However, a *Herschel* and *Spitzer* study of the more evolved O-rich remnant, G292.0+1.8, found that the IR emission is dominated by pre-existing dust in the circumstellar medium (CSM) (Ghavamian & Williams 2016). There is immense debate whether reverse shocks destroy newly formed ejecta dust (e.g. Lau et al. 2015; Biscaro & Cherchneff 2016; Micelotta et al. 2016).

In contrast to CCSNe, the only *Herschel* observations of Type Ia SNRs to date (with a sample size of 2) found that any dust emission seen is due to ISM/CSM dust, suggesting that they do not produce significant amount of dust in their ejecta (Gomez et al. 2012a). Nevertheless, Lau et al. (2015) detected 0.02 $M_\odot$ of warm ~100 K) dust within the 10^4 yr old Sgr A SNR, suggesting that the dust has survived the reverse shock.

Outside of the Milky Way, observations of SN 1987A in the Large Magellanic Cloud with *Herschel* and the Atacama Large Millimetre Array found ~0.5 $M_\odot$ of cold (<25 K) ejecta dust (Matsuura et al. 2011, 2015; Indebetouw et al. 2014; Dwek & Arendt 2015).

The above discussion suggests that core-collapse SNe can produce significant quantities of dust that would help explain high-redshift dust masses. However, this is based on SN dust formation only being verified in a limited number of sources. Therefore a more complete survey is required to establish the importance of SN as dust producers, and to investigate how the dust content varies across SNR types, evolutionary stages, and environment. In this paper we present a survey of SNRs detected at far-infrared (FIR) wavelengths ($\geq$70 μm) with *Herschel* to complement previous SNR dust surveys by R06 and PG11. In Section 2 we introduce the survey, the detected sources, and discuss our selection bias. In Section 3 we derive dust masses of SNRs with signatures related to ejecta dust emission and in Section 4 we use a more advanced technique to further study dust properties in these sources. Section 5 lists our conclusions.

2 SURVEY FOR FAR INFRARED SUPERNOVA REMNANT EMISSION

To make a catalogue of FIR SNRs, we use data obtained by the Photodetector Array Camera and Spectrometer (PACS; Poglitsch et al. 2010) and the Spectral and Photometric Imaging Receiver (SPIRE; Griffin et al. 2010) on board the *Herschel* Space Observatory (hereafter *Herschel*) (Pilbratt et al. 2010) during the *Herschel* Infrared Galactic Plane Survey (Hi-GAL; Molinari et al. 2010). Hi-GAL mapped a 2° latitude strip of the Galactic Plane using two PACS and three SPIRE wavebands centred on 70, 160, 250, 350 and 500 μm. In order to provide a comparison with R06, we study 71 remnants within the region where $10^\circ < |l| < 60^\circ$ and $|b| \leq 1$, which is covered by Hi-GAL I. There are a total of 127 SNRs in this area based on the radio catalogue from Green (2014). *Herschel* has a diffraction limited angular resolution of 5.0–35.9 arcsec, 30 times better than the *IRAS* resolution of $\sim 6 - 8'$ (Saken et al. 1992). Also, the PACS 70 μm maps have an angular resolution of 6.4 arcsec, an improvement over that of the MIPS 70 μm maps of 18 arcsec (Carey et al. 2009). Higher angular resolution is important to resolve SNR dust features from the foreground/background or surrounding ISM. At all wavelengths, the map noise is dominated by Galactic Plane cirrus confusion (Molinari et al. 2013).

Table 1 lists the 71 Galactic SNRs from HiGal studied in this survey. Each remnant was first inspected as a false colour image combining the 70, 160, and 250 μm *Herschel* wavebands, which are regridded and convolved to the resolution of the 250 μm band (Fig. A1). A circle was overlaid to show the SNR radio size (from the Green (2014) catalogue) and X-ray location (the radio location from Green's catalogue is used where X-ray is not available). Various colour scales were applied in order to reveal any FIR structures potentially related to the SNR. We also assessed *Herschel* images in individual bands if any potential SNR dust emission was detected in the initial inspection. The level of FIR detection was then determined by comparing the structure in the *Herschel* images with that at MIR wavelengths using *Spitzer* (R06 and PG11), X-ray and/or radio wavelengths where possible. See Fig. A2 for the IRAC and MIPS images of our sample. Where available, VLA 20 cm images from the Multi-Array Galactic Plane Imaging Survey (MAGPIS) (Helfand et al. 2006)[1] were used (Fig. A2) for sources within the range $|b| < 0.8^\circ$, $5^\circ < l < 48.5^\circ$; 1420 MHz images from the Canadian Galactic Plane Survey (CGPS) were used for sources in the range $52^\circ < l < 192^\circ$ (Taylor et al. 2003); and 0.843 GHz images from the MOST SNR catalogue for sources within the range $245^\circ < l < 48.5^\circ$ (Whiteoak & Green 1996).

Detection levels were assigned on the basis of the classification scheme adopted by R06. That is: 1 = detection (FIR emission that

[1]The MAGPIS database is available at https://third.ucllnl.org/gps/

Table 1. Supernova remnants in the Hi-GAL I Survey ($|l| < 60°$).

SNR	Name	Size[a] (arcmin)	PWN[b] (FIR)	Age (kyr)	SN Type	Ref[c]	GLIMPSE[d]	MIPSGAL[e]	Hi-GAL[f]	Dust features[g]	Comparison[h]
G10.5–0.0		6					–	1	2		R
G11.1–1.0		18×12					–	–	1	Shell	OR
G11.1–0.7		11×7					–	3	3		R
G11.1+0.1		12×10					–	1	1	Western shell	R
G11.2–0.3		4	Y (Y)	1.4–2.4	Type cIIb or Ibc	1	1	1	1	Shell Central region (PWN)	RX
G11.4–0.1		8					3	3	3		R
G11.8–0.2		4					–	2	3		
G12.0–0.1		7	Y (N)	0.3–3.0	Core collapse	2	3	3	3		
G12.5+0.2		6×5					–	1	3		
G14.1–0.1		6×5					–	1	1		
G14.3+0.1		5×4					–	1	1	Partial shell	R
G15.9+0.2		7×5		≤ 2.4	Core collapse	3; 4	3	1	1	Partial shell	RX
G16.4–0.5		13					–	1	1	Central region	R
G16.7+0.1		4	Y (N)	2.1	Core collapse	5	3	2	3		R
G17.0–0.0		5					–	2	3		
G17.4–0.1		6					–	3	2		R
G18.1–0.1		8		5		6	–	4	3		R
G18.6–0.2		6	? (N)	13	Core collapse	7	–	1	1	Outer filaments	R
G18.8+0.3	Kes 67	17×11		16		8	3	3	3		R
G19.1+0.2		27					–	3	3		
G20.0–0.2		10	Y (N)		Core collapse	9; 10	3	3	3		R
G20.4+0.1		8					–	1	1	Shell	R
G21.0–0.4		9×7					–	3	3		R
G21.5–0.9		5	Y (Y)	0.87	Type IIP or Ib/Ic	10; 11	–	1	1	Central region (PWN)	X
G21.5–0.1		5					–	1	1	Central region	R
G21.6–0.8		13					–	–	3		
G21.8–0.6	Kes 69	20		5		12	1	1	3		R
G22.7–0.2		26	? (N)				1	2	3		R
G23.6+0.3		10?					3	1	2		R
G27.4+0.0	4C-04.7 Kes 73	4		0.75–2.1	SN IIL/b	13; 14	3	1	2		R
G27.8+0.6		50×30	? (N)	35–55	Core collapse	15; 16	3	3	4		
G28.6–0.1		13×9					3	1	3		R
G29.6+0.1		5		<8		17; 18	4	3	2		R
G29.7–0.3	Kes 75	3	Y (Y)	<0.84	Type Ib/c	18; 19	3	1	1	Central region (PWN) Partial shell	RX
G31.9+0.0	3C391	7×5		4		20	1	1	1	Partial shell Northwestern radio bar	R
G32.4+0.1		6					–	2	3		
G32.8–0.1	Kes 78	17		6		21; 22	3	3	3		
G33.2–0.6		18					3	2	1	Western shell	R
G33.6+0.1	Kes 79	10		4.4–6.7	Type II	22; 23	2	1	2		R
G34.7–0.4	W44	35×27	Y (N)	2	Core collapse	24; 25	1	1	1	North and western shell Central filaments	R
G35.6–0.4		15×11		2.3		25; 26	–	1	2		R
G39.2–0.3	3C396	8×6	Y (N)	7		26; 27	1	1	1	Western shell	R

Table 1 – *continued*

SNR	Name	Size[a] (arcmin)	PWN[b] (FIR)	Age (kyr)	SN Type	Ref[c]	GLIMPSE[d]	MIPSGAL[e]	Hi-GAL[f]	Dust features[g]	Comparison[h]
G41.1–0.3	3C397	4.5×2.5		1.35–1.75	Type Ia	27; 28	1	1	3		R
G43.3–0.2	W49B	4×3		1–4	Bipolar Ib/Ic	29; 30	1	1	1	Fe/radio loop H_2 filament	R
G54.1+0.3		12?	Y (Y)	2	Core collapse	31	3	3	1	PWN southern rim	
G54.4–0.3	(HC40)	40		95		32	1	1	1	Outer filaments	
G55.0+0.3		20×15?		≤1900		33	2	2	2		
G296.8–0.3	1156–62	20×14		2–10		34	3	1	3		
G304.6+0.1	Kes 17	8		28–64	Core collapse	35	1	1	1	Western shell	
G310.6–0.3	Kes 20B	8					2	3	3		
G310.8–0.4	Kes 20A	12					1	1	1		
G311.5–0.3		5		23		36	1	1	1	Shell	
G332.0+0.2		12					4	3	3		
G332.4–0.4	RCW 103	10		2	Type IIP	37; 38	1	1	1	Southern arc	X
G332.4+0.1	MSH 16–51 Kes 32	15		3		39	2	2	3		
G336.7+0.5		14×10					4	1	3		R
G337.2–0.7		6		0.75–3.5	Type Ia	40; 41	4	1	2		X
G340.4+0.4		10×7		3.1		42	4	3	3		
G340.6+0.3		6		2.6		42	2	1	1	Shell	R
G341.2+0.9		22×16	Y (N)	32.6	Core collapse	43	4	3	3		
G341.9–0.3		7		5		42	4	3	3		
G342.0–0.2		12×9		11.7		42	3	3	3		
G344.7–0.1		8		3	Type Ia	44; 45	1	1	1	North-central region	R
G345.7–0.2		6					4	1	2		
G346.6–0.2		8		47	Type Ib/Ic/II	36	1	2	2		
G347.3–0.5	RX J1713.7–3946	65×55		1.59–2.1	Type Ib/c	46	3	3	3		
G348.5–0.0		10?					1	1	1	Arc	R
G348.5+0.1	CTB37A	15?		32–42		36	1	1	1	Northern arc Breakout region	R
G348.7+0.3	CTB 37B	17?		5	Core collapse	47	3	1	1	North-eastern shell	R
G349.2–0.1		9×6					3	3	4		
G349.7+0.2		2.5×2		1.8		48	1	1	1	Eastern shell	R

Notes.
[a]Radio size from Green's catalogue. [b]'Y' indicates that a source contains an associated PWN, '?' indicates an unconfirmed PWN candidate. FIR detection of the PWN is indicated in brackets.
[c]References for SNR age and SN type: [1]Borkowski, Reynolds & Roberts (2016), [2]Yamauchi, Bamba & Koyama (2014b), [3]Reynolds (2006), [4]Klochkov et al. (2016), [5]Helfand, Agueros & Gotthelf (2003b), [6]Leahy, Green & Tian (2014), [7]Voisin et al. (2016), [8]Dubner, Giacani & Reynoso (1999), [9]Petriella, Paron & Giacani (2013), [10]Bietenholz & Bartel (2008), [11]Bocchino et al. (2005), [12]Tian & Leahy (2008), [13]Kumar et al. (2014), [14]Chevalier (2005), [15]Reich, Furst & Sofue (1984), [16]Misanovic, Kargaltsev & Pavlov (2010),[17]Gaensler, Gotthelf & Vasisht (1999), [18]Leahy & Tian (2008), [19]Morton et al. (2007), [20]Chen et al. (2004), [21]Zhou & Chen (2011), [22]Zhou et al. (2016), [23]Sato et al. (2016), [24]Wolszczan, Cordes & Dewey (1991), [25]Zhu et al. (2013), [26]Harrus & Slane (1999), [27]Leahy & Ranasinghe (2016), [28]Yamaguchi et al. (2015), [29]Pye et al. (1984); Smith et al. (1985); Hwang, Petre & Hughes (2000), [30]Lopez et al. (2013), [31]Bocchino, Bandiera & Gelfand (2010), [32]Park et al. (2013), [33]Matthews, Wallace & Taylor (1998), [34]Gaensler, Manchester & Green (1998), [35]Combi et al. (2010b), [36]Pannuti et al. (2014), [37]Nugent et al. (1984); Carter, Dickel & Bomans (1997), [38]Frank, Burrows & Park (2015), [39]Vink (2004), [40]Rakowski et al. (2006), [41]Takata et al. (2016), [42]Caswell et al. (1983), [43]Frail, Goss & Whiteoak (1994), [44]Giacani et al. (2011), [45]Yamaguchi et al. (2012), [46]Tsuji & Uchiyama (2014), [47]HESS Collaboration (2008b), and [48]Tian & Leahy (2014). Level of detection for each SNR is listed for the following surveys: [d]*Spitzer* GLIMPSE (IRAC, Reach et al. 2006), [e]*Spitzer* MIPSGAL (MIPS, Pinheiro Goncalves et al. 2011), [f]*Herschel* Hi-GAL (PACS & SPIRE, this work). [g]Location of FIR detected dust features. [h]Waveband of previous detection to which FIR structure is compared: O = optical, R = radio, X = X-ray. Detection level of remnants: 1 = likely detection, 2 = possible detection, 3 = unlikely detection but confused, 4 = not detected, – = unstudied.

Table 2. Summary of the level 1 detected sample in this work. [a]The total number for this classification is larger than the number of level 1 detected sources as dust in some SNRs in detected in both outer and inner regions. [b]SNRs for which there is evidence that the detected central region is associated with the confirmed PWN.

Detection Type		Number Detected
SNR region[a]	Shell / outer shock region	23
	Inner ejecta region	8
	Confirmed PWN[b]	4
Age (kyr)	$\leq$1	2
	1 $<$Age $\leq$ 10	12
	10 $<$Age $\leq$ 20	1
	$>$20	4
	Unknown	9
SN Type	Type Ia	1
	Core collapse	11
	Unknown	13

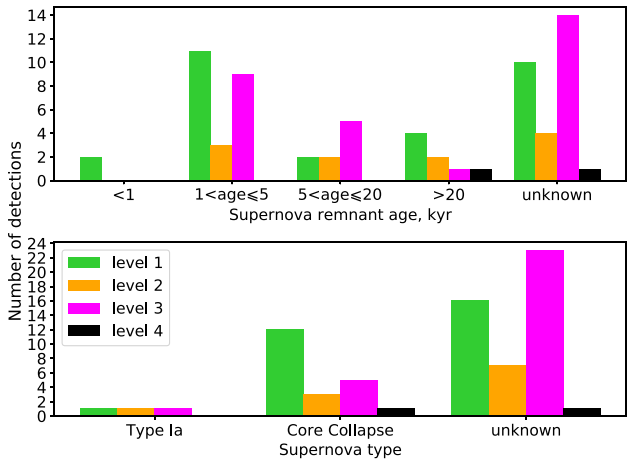

Figure 1. Source types detected in the sample. *Top*: Number of detections of sources of different ages. *Bottom*: Number of detections of different SN types.

is clearly correlated with radio, MIR, or X-ray structures and can be distinguished from ISM), 2 = possible detection (FIR emission in the region of the SNR, potentially related to radio, MIR, or X-ray structures but confused with ISM), 3 = unlikely detection (detection of FIR emission but probably unrelated to the SNR), and 4 = not detected in the FIR. In Section 2.1 we summarize our findings based on Figs A1 and A2 and in Section 2.2 we provide individual notes on each of the level 1 and level 2 detected sources.

Of the 29 SNRs detected in this survey, 13 are in common with R06 and 21 with PG11. R06 detected 18 of 95 SNRs from GLIMPSE and PG11 detected 39 of 121 SNRs from the MIPSGAL Survey; their classifications of our sample are listed in Table 1. We detect 1 additional SNR, G11.1–1.0, which was not in the PG11 or R06 samples.

2.1 Summary of the sample

Table 2 and Fig. 1 give a summary of the types of SNRs detected in this study. Of our new FIR detections, we observe dust emission from the shell / outer shock region of 23 SNRs, and within the inner ejecta region (interior to the reverse shock) of eight sources. We detect 1 Type Ia (G344.7–0.1) and 11 core collapse SNe; the

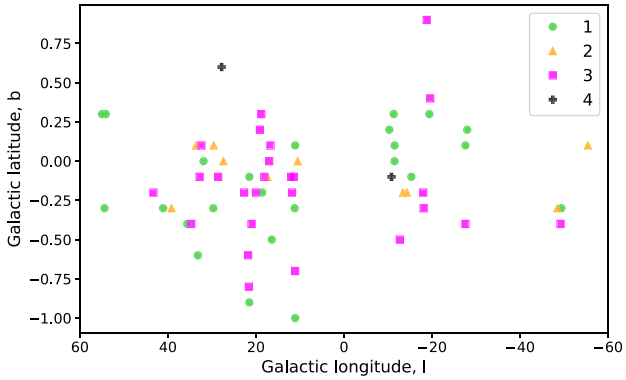

Figure 2. Location of sources from our sample within the Galactic Plane. We do not see any bias in the location of detected sources.

emission from the Type Ia SNR is thought to arise from a shocked cloud in front of the SNR rather than the ejecta (see Section 2.2 for more details). Of the SNRs in our survey with SN type classification, 87 per cent are core collapse with only three Type Ia SNe. This adds 27 new sources to the current sample of three Galactic objects (four including LMC) with confirmed cool dust ($<$50 K). Fig. 1 demonstrates that we are biased towards detecting young SNRs as those aged $\leq$5 kyr make up 61 per cent of the sources in our survey which have estimated ages. We are least likely to detect sources that do not have an estimated age. These sources make up a large proportion of the fainter sources in our sample, making up 53 per cent of sources with a 1 GHz flux below 5 Jy. Furthermore, the majority of these sources are not very well studied and there are few images available to compare morphology.

Fig. 2 compares the location of the sources on the sky with their assigned detection level in this work to check if there is any bias due to location (e.g. due to higher levels of confusion expected towards the Galactic centre). We see little evidence for any such bias.

We find that five PG11 detections are only a level 2 with *Herschel* and a further four are level 3 in this study. Some of these differences are due to limitations of observing at FIR wavelengths. In many cases the FIR emission is too confused to distinguish between the ISM and any SNR-related emission that may be at a similar temperature. Furthermore, the *Spitzer* data ($\leq$24 μm) has higher angular resolution ($<$2 aracsec at 3.6–8.0 μm and 6 arcsec at 24 μm) than that of *Herschel* and so may be better at resolving dust structures that emit at both MIR and FIR wavelengths. An example of this issue is G27.4+0.0 (Fig. 3) from which PG11 detected clear structure at 24 μm, similar to the X-ray structure (fig. 22 in PG11). We detect some emission at 70 μm that may be associated with the SNR. However, extensive interstellar dust emission to the west of the SNR makes any related dust emission difficult to distinguish from the local ISM in *Herschel* wavebands. We note that synchrotron radiation may also contribute at the long wavelengths but since the majority of our detected sources are brightest at the shortest *Herschel* wavelengths, the synchrotron contamination is minimal. We also do not expect the *Herschel* flux to be dominated by line emission; studies of line intensity in two SNRs found a negligible contribution in the *Herschel* wavebands (Gomez et al. 2012b; De Looze et al. 2017).

We detect FIR emission from four out of the nine confirmed PWN sources in our sample: G11.2–0.3, G21.5–0.9, G29.7–0.3, and G54.1+0.3. The discovery of cold dust in G54.1+0.3 has previously been reported based on FIR and MIR observations (Temim et al. 2017; Rho et al. 2018). We do not detect dust features related to the 4 'unconfirmed' PWN candidates in our sample (G12.0–0.1,

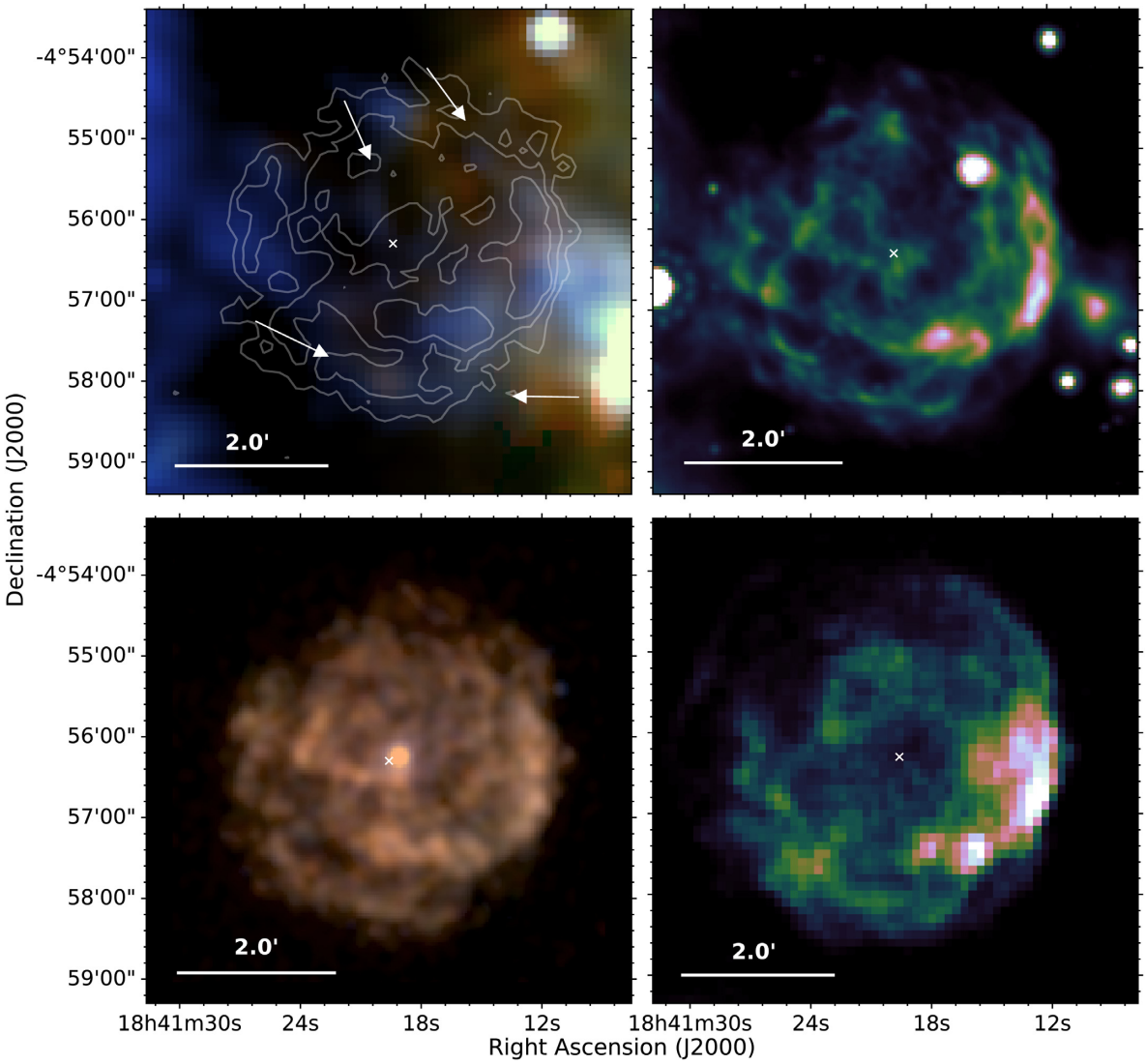

Figure 3. G27.4 + 0.0 – *Top-left*: *Herschel* colour image with X-ray contours overlaid, colours are red = 250 μm, green = 160 μm, and blue = 70 μm. The same *Herschel* colour combinations are used in Figs 4–31. The white arrows indicate emission at 70 μm, which may be associated with SNR filaments detected at other wavelengths. However, extensive dust emission to the west makes the region very confused and FIR emission cannot be conclusively distinguished from the local ISM. There is no dust emission detected at other *Herschel* wavelengths, which corresponds to the X-ray contours. *Top-right*: *Spitzer* MIPS 24 μm image. *Bottom-left*: *Chandra* three-colour image, colours are red = 0.8–1.7 keV, green = 1.7–2.6 keV, and blue = 2.6–7.0 keV. The pulsar PSR J1841–0456 can be seen at the centre of the SNR. *Bottom-right*: VLA 20 cm radio image. The white cross shows the X-ray coordinates of the SNR centre.

G18.6–0.2, G22.7–0.2, and G27.8+0.6). The four detected PWNe all have ages less than 2.5 kyr, which could indicate a lack of dust in older PWNe due to destruction by the reverse shock at later times. However, this is a limited sample making it difficult to come to general conclusions, especially since the reverse shock in G11.2–0.3 has already passed the ejecta material (Borkowski et al. 2016). Both G29.7–0.3 and G54.1+0.3 were classified as level 3 detections by R06 but have been classified here as level 1 detections. The *Herschel* dust emission is clear in the images due to the dust temperature being above the typical ISM dust, likely due to heating by the central PWN. There is no IRAC detection of the PWNe associated with G11–0.2 or G21.5–0.9. It may be that this source of heating does not increase the dust temperature by an adequate amount for strong emission in the IRAC wavebands.

Clearly there are limitations to detecting SNRs in the FIR and we have quite complex selection effects. We easily detect dust in SNRs where the dust is at a different temperature to the local ISM or where there is little contaminating foreground/background dust. This biases us towards younger SNRs, or those with a source of heating, such as a PWN or shock heating. A further selection effect arises from the availability of radio and X-ray data as these images are used to visually compare FIR structures and determine if any FIR structures correlation with the X-ray and radio structures associated with the SNR. If radio and X-ray data are unavailable, it can be difficult to clearly distinguish SN and ISM material.

2.2 Results for individual remnants

Here we provide notes on individual sources for which we detect dust within the SNR (shell or inner ejecta) in the *Herschel* three-colour images. Detected remnants (level 1 in Table 1) are in bold and possible detections (level 2 in Table 1) in italic. *Herschel* FIR

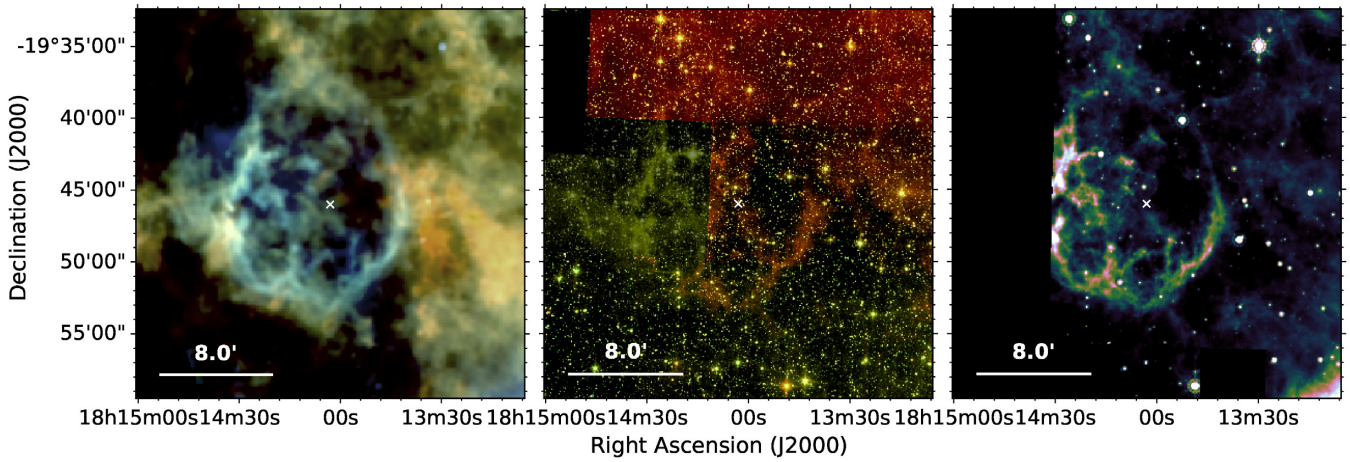

Figure 4. G11.1–1.0 – *Left*: *Herschel* colour image. *Middle*: *Spitzer* IRAC four-colour image, colours are red = 8.0 μm, yellow = 5.8 μm, green = 4.5 μm, and blue = 3.6 μm. *Right*: *Spitzer* MIPS 24 μm image. In both images, filaments of dust are seen at the outer edges of the shocks. The white cross shows the radio coordinates of the SNR centre from Green (2014).

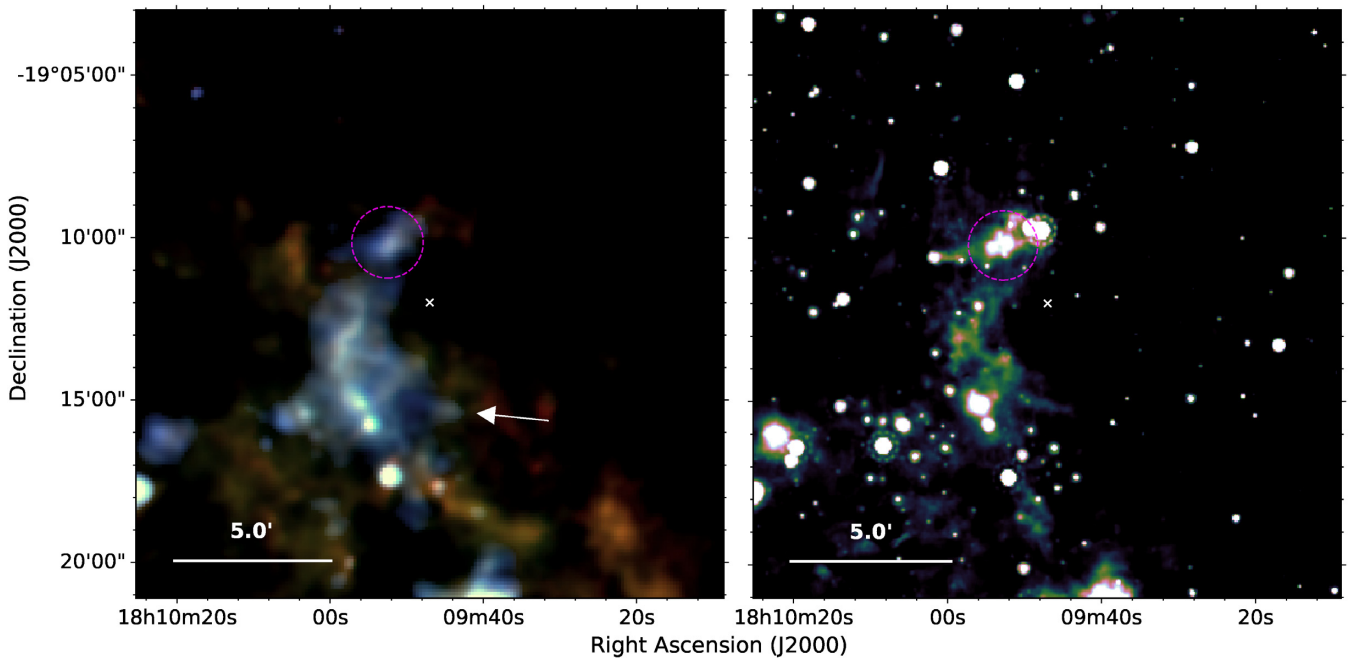

Figure 5. G11.1 + 0.1 – *Left: Herschel* three-colour image. *Right: Spitzer* MIPS 24 μm image. Dust is seen in an arc, with small clumps to the east of the remnant at the outer shock (blue in the *Herschel* image). The white cross shows the radio coordinates of the SNR centre from Green (2014).

and *Spitzer* NIR / MIR images for the entire sample are shown in Figs A1 and A2.

G10.5–0.0: Brogan et al. (2006) detected a partial radio shell at a wavelength of 90 cm from this remnant that has a potential X-ray counterpart (Sugizaki et al. 2001). PG11 classified this source as a level 1 MIR detection as there is 24 μm emission, which roughly coincides with radio structures in places. There is FIR emission to the north of the 24 μm structure, close to a radio peak at $\alpha = 18^{\rm h}09^{\rm m}02.4^{\rm s}$, $\delta = -19°48'06.2''$ although we do not see a convincing likeness to the radio structure (Fig. A2). There are also FIR peaks at $\alpha = 18^{\rm h}09^{\rm m}07.4^{\rm s}$, $\delta = -19°46'18''$ and $\alpha = 18^{\rm h}09^{\rm m}06.8^{\rm s}$, $\delta = -19°47'09.8''$, which do not correlate with any radio emission.

G11.1–1.0 (Fig. 4): Unstudied by both R06 and PG11, we detect a shell of FIR dust emission in Fig. 4. This is brightest in the south-eastern region that is detected across all of the *Herschel* bands. The structure is very similar to that in the 90 cm radio (Brogan et al. 2006) and Hα (Stupar & Parker 2011), especially in the filaments near to $\alpha = 18^{\rm h}14^{\rm m}29^{\rm s}$, $\delta = -19°43'53''$, $\alpha = 18^{\rm h}14^{\rm m}30^{\rm s}$, $\delta = -19°49'00''$, and $\alpha = 18^{\rm h}13^{\rm m}56^{\rm s}$, $\delta = -19°49'38''$. There is also bright 24 μm and IRAC (5.8 and 8.0 μm) emission from the shell coinciding with the *Herschel* emission, although the entire structure is not covered by the 4.5 and 8.0 μm GLIMPSE bands or the 24 μm band.

G11.1+0.1 (Fig. 5): This region is very confused however, there is FIR dust emission in a partial shell structure detected to the east of

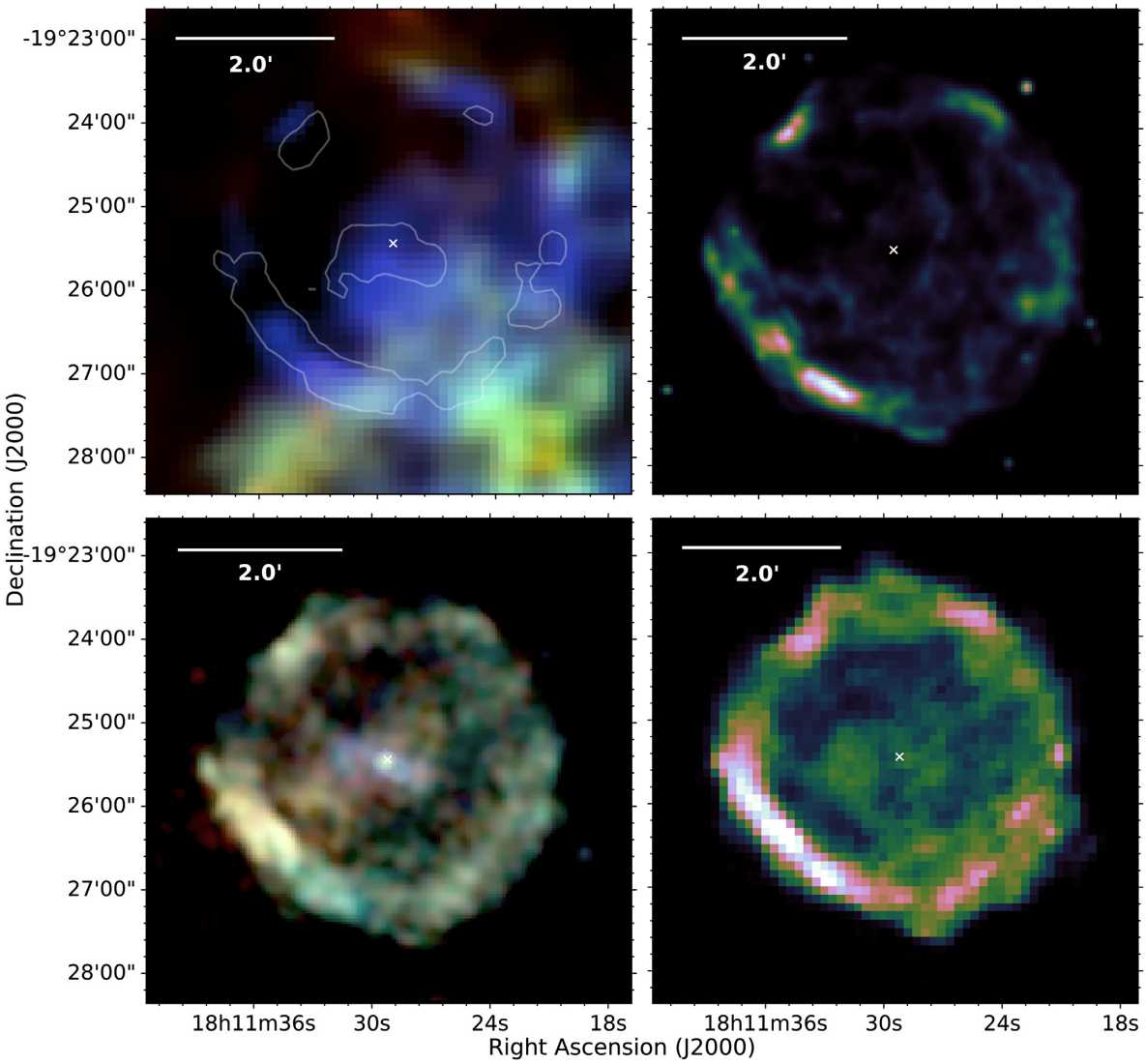

Figure 6. G11.2–0.3 – *Top-left*: *Herschel* three-colour image with X-ray contours overlaid showing the location of the PWN and outer shocks, due to interaction with surrounding ISM / CSM. Dust is clearly seen in a bright ring and south of the pulsar and its nebula. *Top-right*: *Spitzer* MIPS 24 μm image. *Bottom-left*: *Chandra* three-colour image, colours are red = 0.8–1.2 keV, green = 1.2–2.0 keV, and blue = 2.0–10.0 keV. *Bottom-right*: VLA 20 cm radio image. The white crosses show the X-ray coordinates of the SNR centre, which is at the location of the central pulsar.

this remnant, which correlates with 90 cm radio emission detected by Brogan et al. (2004). Emission is detected across all *Herschel* bands from a clump centred at $\alpha = 18^{\rm h}09^{\rm m}53^{\rm s}$, $\delta = -19^\circ10'21''$ and a much fainter extended filament near to $\alpha = 18^{\rm h}09^{\rm m}46^{\rm s}$, $\delta = -19^\circ15'12''$. Unstudied by R06, this remnant was also a level 1 detection by PG11, who detected 24 μm emission at the locations of bright radio knots.

G11.2–0.3 (Fig. 6): This core-collapse remnant has a composite radio morphology that is very similar to the X-ray shell (Vasisht et al. 1996; Chevalier 2005). Also associated with the SNR is a central pulsar (AX J1811.5–1926) at $\alpha = 18^{\rm h}11^{\rm m}29.22^{\rm s}$, $\delta = -19^\circ25'27.6''$ (Kaspi et al. 2001), which has almost the same energy as expected at birth. X-ray morphology indicates that the surrounding PWN has been compressed and all ejecta have been reheated by the passage of the reverse shock (Torii et al. 1997; Borkowski et al. 2016). Detection of 1.644 μm [FeII] emission from the shell and knots surrounding the PWN indicates the presence of shocked CSM and ejecta material (Koo et al. 2007; Moon et al. 2009).

Expansion rates suggest that this is a young SNR with an estimated age of around 1400–2400 yr (Tam & Roberts 2003; Borkowski et al. 2016). R06 suggested that, because of this young age, IRAC emission from shocked gas in filaments near $\alpha = 18^{\rm h}11^{\rm m}35^{\rm s}$, $\delta = -19^\circ26'23''$ may originate from ejecta. PG11 detected the same filaments as diffuse, unresolved MIPS emission, and a shell that correlates with X-ray structures. Almost identical to the X-ray and 24 μm structure, we detect a ring of dust emission that is especially bright at 70 μm in Fig. 6. The southern rim of the SNR is the brightest region at 70 μm, as well as in the X-ray and MIR (MIPS and IRAC). The emission in this region is much more confused at the longer *Herschel* bands. There is also bright dust emission in the central region centred at $\alpha = 18^{\rm h}11^{\rm m}29^{\rm s}$, $\delta = -19^\circ25'54''$ which coincides with X-ray emission from the central pulsar and its nebula. We suggest that this could be ejecta dust heated by the PWN. We checked ^{12}CO (J = 3→2) data from the CO High Resolution Survey (COHRS; Dempsey, Thomas & Currie 2013) and found no detection from the SNR or surrounding ISM clouds.

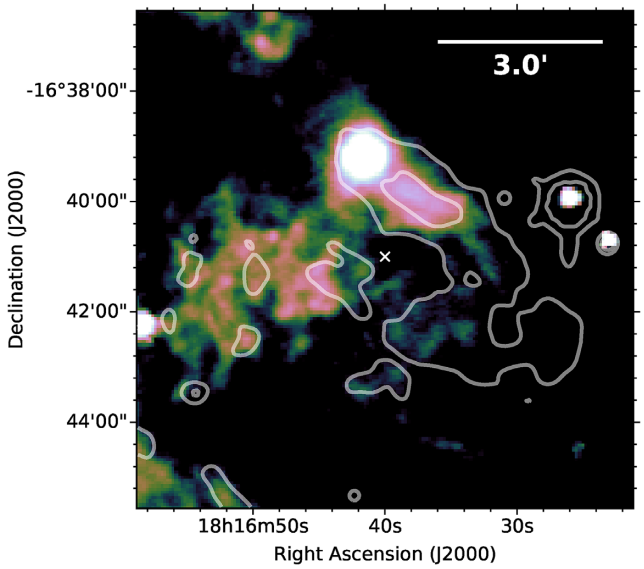

Figure 7. G14.1–0.1 – *Herschel* 70 μm image with 24 μm contours overlaid. The magenta cross shows the radio coordinates of the SNR centre from Green (2014).

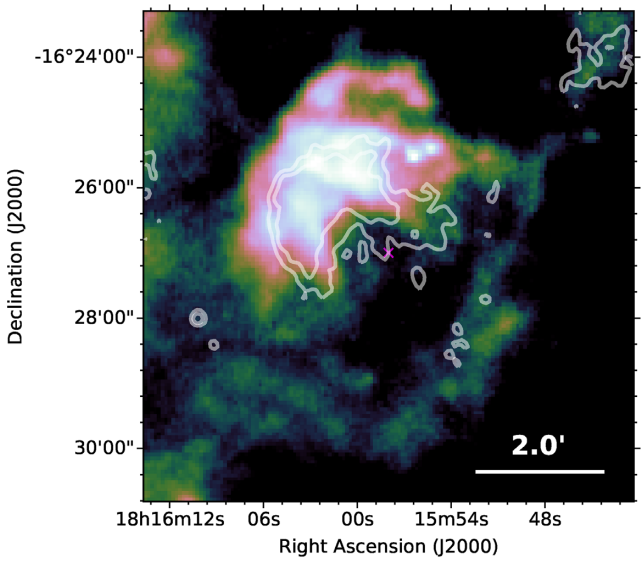

Figure 8. G14.3+0.1 – *Herschel* 70 μm image with 24 μm contours overlaid. The magenta cross shows the radio coordinates of the SNR centre from Green (2014).

G14.1–0.1 (Fig. 7): PG11 detected a horse-shoe shape of 24 μm emission roughly matching the radio shell structure (Brogan et al. 2004). There is diffuse 70 μm emission to the north-east of the shell and an FIR peak coinciding with a radio peak at roughly $\alpha = 18^{h}16^{m}41.6^{s}, \delta = -16^{\circ}39'11''$.

G14.3+0.1 (Fig. 8): We clearly observe 70 μm emission coincident with the radio partial shell structure detected by Brogan et al. (2006). There is emission in the longer *Herschel* wavebands, however the structure is different and association with the SNR is unclear.

G15.9+0.2 (Fig. 9): This relatively young source ($\leq$2400 yr) is the remnant of a CCSN and contains the neutron star CXOU J1818 (Reynolds 2006; Klochkov et al. 2016). Strong lines in the X-ray

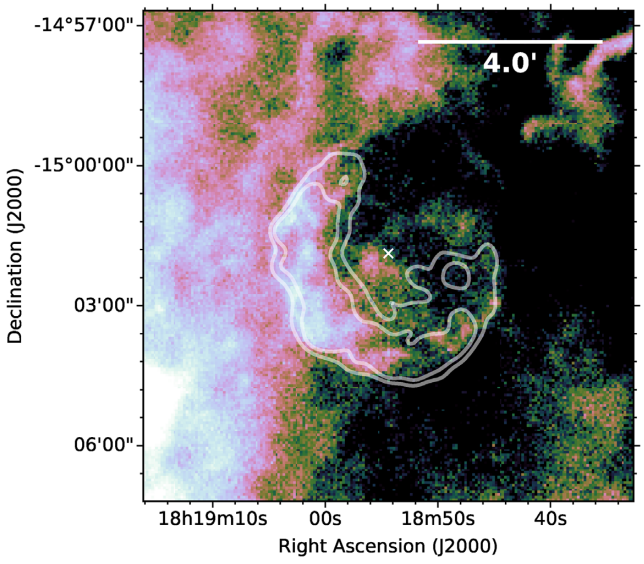

Figure 9. G15.9+0.2 – *Herschel* 70 μm image with X-ray contours overlaid. Dust is detected at 70 μm in a partial shell that is brightest to the east. The white cross shows the radio coordinates of the SNR centre from Green (2014).

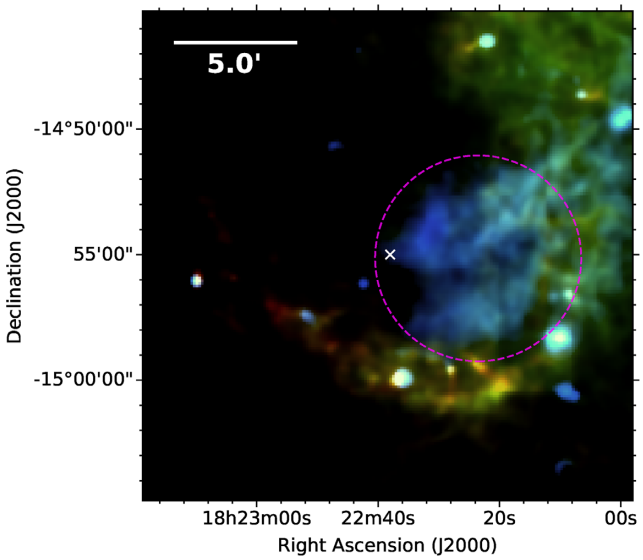

Figure 10. G16.4–0.5 – *Herschel* three-colour image. Diffuse dust emission is detected in the central region in blue as indicated by the magenta circle. A ridge of dust is detected at wavebands of 250 μm and greater along the southern edge of the remnant that probably is not associated. The white cross shows the radio coordinates of the SNR centre from Green (2014).

indicate the presence of ejecta. This source is undetected by IRAC; however, the 24 μm structure closely correlates with the X-ray and radio. A partial shell of dust is detected around the eastern and south-eastern edge of this remnant at the location of the X-ray and radio emission.

G16.4–0.5 (Fig. 10): Unstudied by R06, PG11 classified this SNR as a level 1 MIPS detection. This SNR has a partial radio shell morphology (Brogan et al. 2006). A region of diffuse dust emission at 70 μm is detected towards the centre of the remnant, identified by a magenta circle in Fig. A2, which corresponds to emission at 24 μm. A 4′ long filament centred on $\alpha = 18^{h}22^{m}17^{s}, \delta =$

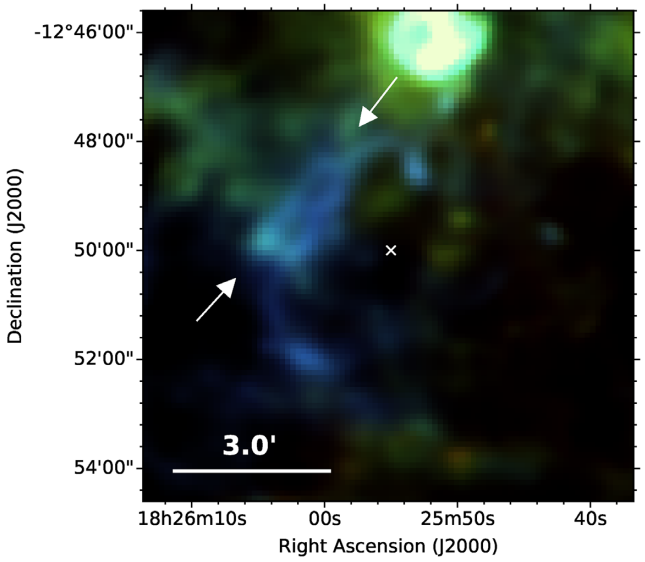

Figure 11. G18.6–0.2 – *Herschel* three-colour image. A partial shell of dust is detected at the eastern edge of this remnant, at the same location as radio structures. Two parallel filaments of dust are detected in the north-eastern shell, between the two arrows. The white cross shows the radio coordinates of the SNR centre from Green (2014).

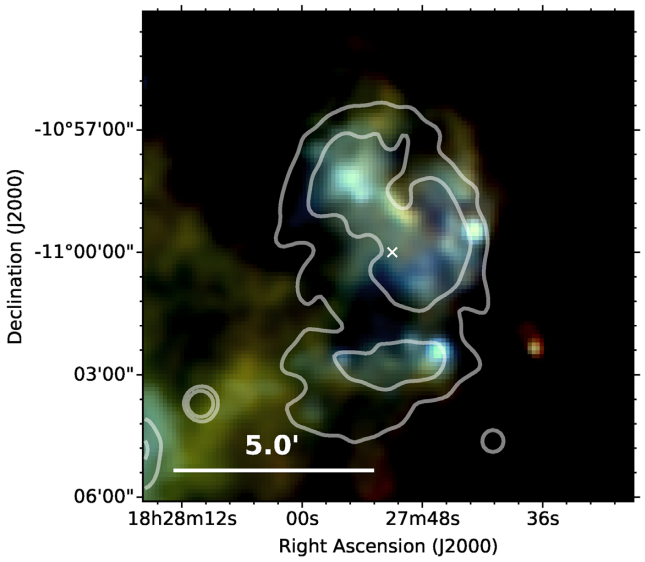

Figure 12. G20.4+0.1 – *Herschel* three-colour image with 20 cm VLA contours overlaid. FIR emission is detected within the contours at all *Herschel* wavelengths. The white cross shows the radio coordinates of the SNR centre from Green (2014).

$-14°52'51''$ is detected across all five *Herschel* wavebands and coincides with MIPS (PG11) and IRAC emission.

There is bright emission in all *Herschel* bands along the southern ridge (red structure in Fig. 10). This emission seems to be of a similar temperature to, or cooler than, the surrounding ISM and association with the SNR is unlikely.

G17.4–0.1: This SNR has a partial shell radio structure. The region is confused in the FIR and it is difficult to distinguish any SNR emission from that of the ISM. There is a bright FIR region to the west of the SNR that coincides with 24 μm emission and a radio peak detected by Brogan et al. (2006), although the morphology is different and the association is unclear.

G18.6–0.2 (Fig. 11): Voisin et al. (2016) suggested that the pulsar PSR J1826−1256 may be associated with this remnant as their estimated distances are similar. Although there is dust emission in the region of the pulsar in Fig. 11 at $\alpha = 18^{h}26^{m}08.2^{s}$, $\delta = -12°56'46''$, it is indistinguishable from the local ISM and unclear as to whether any of this is associated to the PSR J1826−1256. Dust emission is detected at 70 μm from the eastern region of this shell-type SNR that is brightest from two parallel filaments detected near to $\alpha = 18^{h}26^{m}00^{s}$, $\delta = -12°49'26''$ and $\alpha = 18^{h}26^{m}02^{s}$, $\delta = -12°49'08''$. The morphology seems to correlate with 90 cm radio emission from Brogan et al. (2006) and the partial shell detected by PG11. At 160 μm the region is too confused to determine if any emission is associated with the SNR, and in the longer *Herschel* wavebands there is no evidence of SNR emission.

G20.4+0.1 (Fig. 12): PG11 detected emission correlating with the radio shell of this SNR. We detect FIR emission at all *Herschel* wavelengths that lies within the radio contours, as shown in Fig. 12.

G21.5–0.9 (Fig. 13): This Crab-like remnant has a pulsar (PSR J1833–1034) at its centre with a non-thermal X-ray halo (Camilo et al. 2006). Properties of the PWN, the pulsar, and the shell suggest that the remnant is $\lesssim$1000 yr old (Camilo et al. 2006) and H I and CO observations tell us that this SNR is at a distance of 4.8 kpc (Tian & Leahy 2008). Emission at all *Herschel* bands is detected at $\alpha = 18^{h}33^{m}33.8^{s}$, $\delta = -10°34'14''$, slightly offset from the location of the central pulsar and its wind nebula as shown by X-ray contours in Fig. 13. This is more confused with the local environment at longer wavebands. PG11 also made a level 1 detection of the central region. We suggest that dust in this region is heated by the PWN. We checked ^{13}CO (J = 1→0) data from the Galactic Ring Survey (GRS; Jackson et al. 2006) and found no CO detection towards the SNR.

G21.5–0.1 (Fig. 14): Dust is observed in a filled shell from this remnant at all *Herschel* wavelengths, which correlates with the 24 μm emission (PG11) and the 90 cm radio structure detected by Brogan et al. (2006). Filaments of dust are indicated in Fig. 14. This includes an ∼2.5′ bright filament detected to the east, centred near $\alpha = 18^{h}31^{m}01^{s}$, $\delta = -10°09'54''$, which is also detected in the MIR. Another FIR-detected filament is centred near $\alpha = 18^{h}30^{m}41.5^{s}$, $\delta = -10°10'47''$ and is roughly 1.6′ long. Although unstudied by R06, PG11 detected MIPS and IRAC emission along the southern ridge.

Nevertheless, the origin of this emission requires further study. Anderson et al. (2017) suggest that this is a H II region that has been incorrectly classified as an SN structure. This is because the entire structure coincides with the WISE H II region G21.560–0.108 and PG11 derived a high MIR to radio flux ratio indicative of H II regions.

G23.6+0.3: PG11 detected an elongated region of 24 μm emission at the location of the SNR radio structure. However, they argue that the SNR morphology more closely resembles that of a H II region than an SNR, and the nature of this object should therefore be reconsidered. There is FIR emission in the region of the radio structure, however this is offset (A2).

G27.4+0.0: This shell-type SNR is thought to have been produced by a very massive progenitor ($\gtrsim$20 $M_{\odot}$) between 750 and 2100 yr ago (Kumar et al. 2014). Although there is a very good detection at 24 μm, the region is confused at *Herschel* wavelengths (Fig. 3). We find some evidence of dust emission at 70μm in the region which may be associated with X-ray and 24μm SNR filaments. However, we cannot definitively conclude this as there is

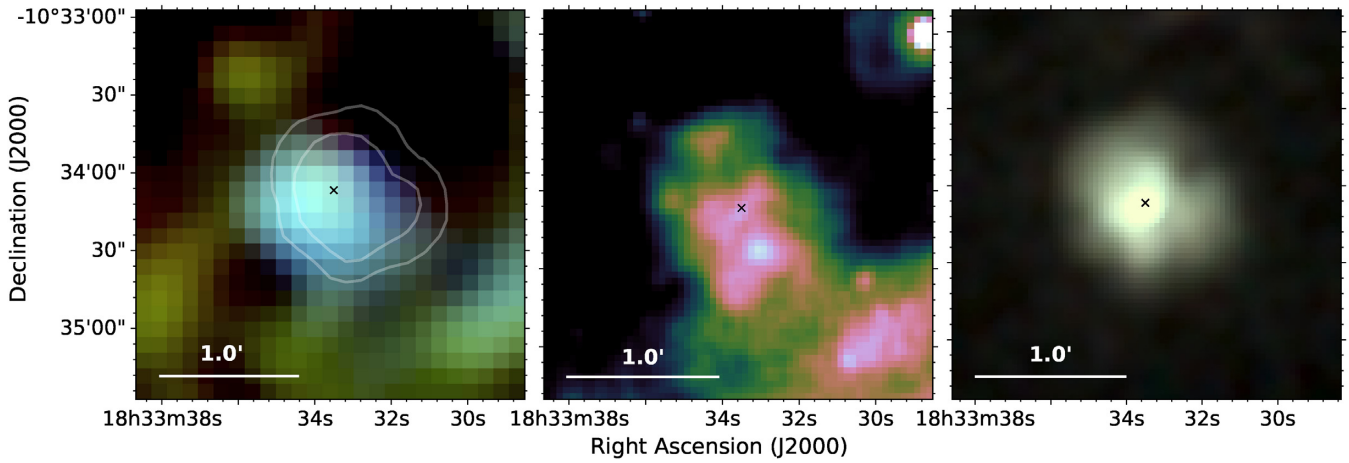

Figure 13. G21.5–0.9 – *Left*: *Herschel* three-colour image with X-ray contours overlaid to show the location of the pulsar and PWN. Dust is observed in a clump in the central area, at the location of the PWN. *Middle*: *Spitzer* MIPS 24 μm image. *Right*: *Chandra* colour image (red = 1.0–2.1 keV, green = 2.1–4.0 keV, and blue = 4.0–10.0 keV). The black crosses show the X-ray coordinates of the SNR centre.

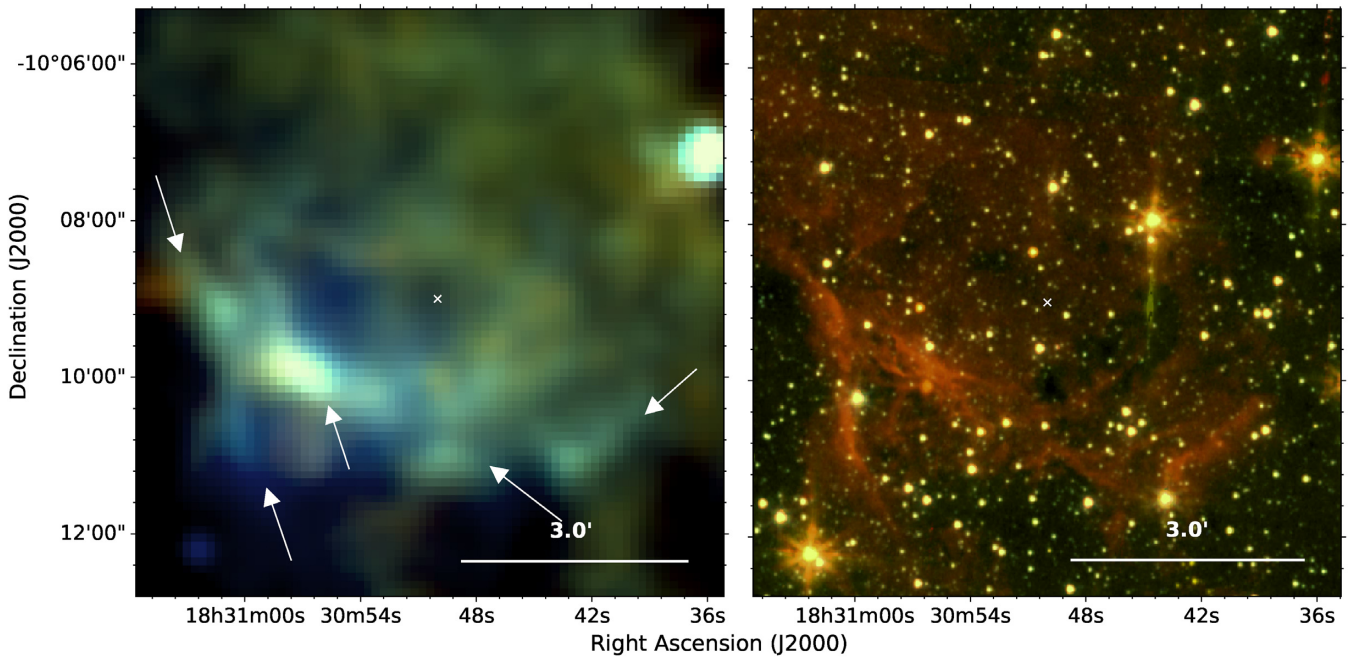

Figure 14. G21.5–0.1 – *Left*: *Herschel* three-colour image. Dust is observed in the central region in a filled shell. The arrows indicate filaments of dust that correlate with the IRAC detection by Reach et al. (2006). *Right*: *Spitzer* IRAC four-colour image, colours are red = 8.0 μm, yellow = 5.8 μm, green = 4.5 μm, and blue = 3.6 μm. The white cross shows the radio coordinates of the SNR centre from Green (2014).

extensive interstellar dust emission to the west confusing the region at FIR wavelengths.

G29.6+0.1: This is a young remnant (< 8000 yr; Gaensler et al. 1999) with a non-thermal radio shell and an associated compact source (AX J1845−0258) which is likely a pulsar (Gaensler et al. 1999; Vasisht et al. 2000). Broad molecular lines have been detected towards the remnant, suggesting that it is interacting with a molecular cloud (Kilpatrick, Bieging & Rieke 2016). Numerous young stellar objects are detected in this field, including FIR bright sources at $\alpha = 18^{h}44^{m}51^{s}$, $\delta = -02^{\circ}55'18''$, $\alpha = 18^{h}44^{m}53.3^{s}$, $\delta = -02^{\circ}56'03''$, and $\alpha = 18^{h}44^{m}49.2^{s}$, $\delta = -02^{\circ}58'15''$ (Veneziani et al. 2013). There is also FIR emission across all *Herschel* and *Spitzer* bands coincident with the radio source at $\alpha = 18^{h}44^{m}55.1^{s}$, $\delta = -02^{\circ}55'36.9''$ (Gaensler et al. 1999). The radio shell is not detected by IRAC or MIPS, although at *Herschel* wavelengths there is emission that may be associated (Figure A2). However, contamination from local ISM to the southwest makes it difficult to distinguish SNR emission.

G29.7–0.3 (Fig. 15): It is possible that this SNR resulted from a Wolf–Rayet star that exploded as a type Ib/c SN after clearing an ∼10 pc bubble (Morton et al. 2007). CO observations of an associated molecular cloud put the remnant at a kinematic distance of ∼10.6 kpc, at the far side of the Sagittarius arm (Su et al. 2009). Although there is bright MIPS emission from this remnant in both a partial shell and central region (level 1 by PG11), there is no clear emission at IRAC wavelengths from the SNR (level 3

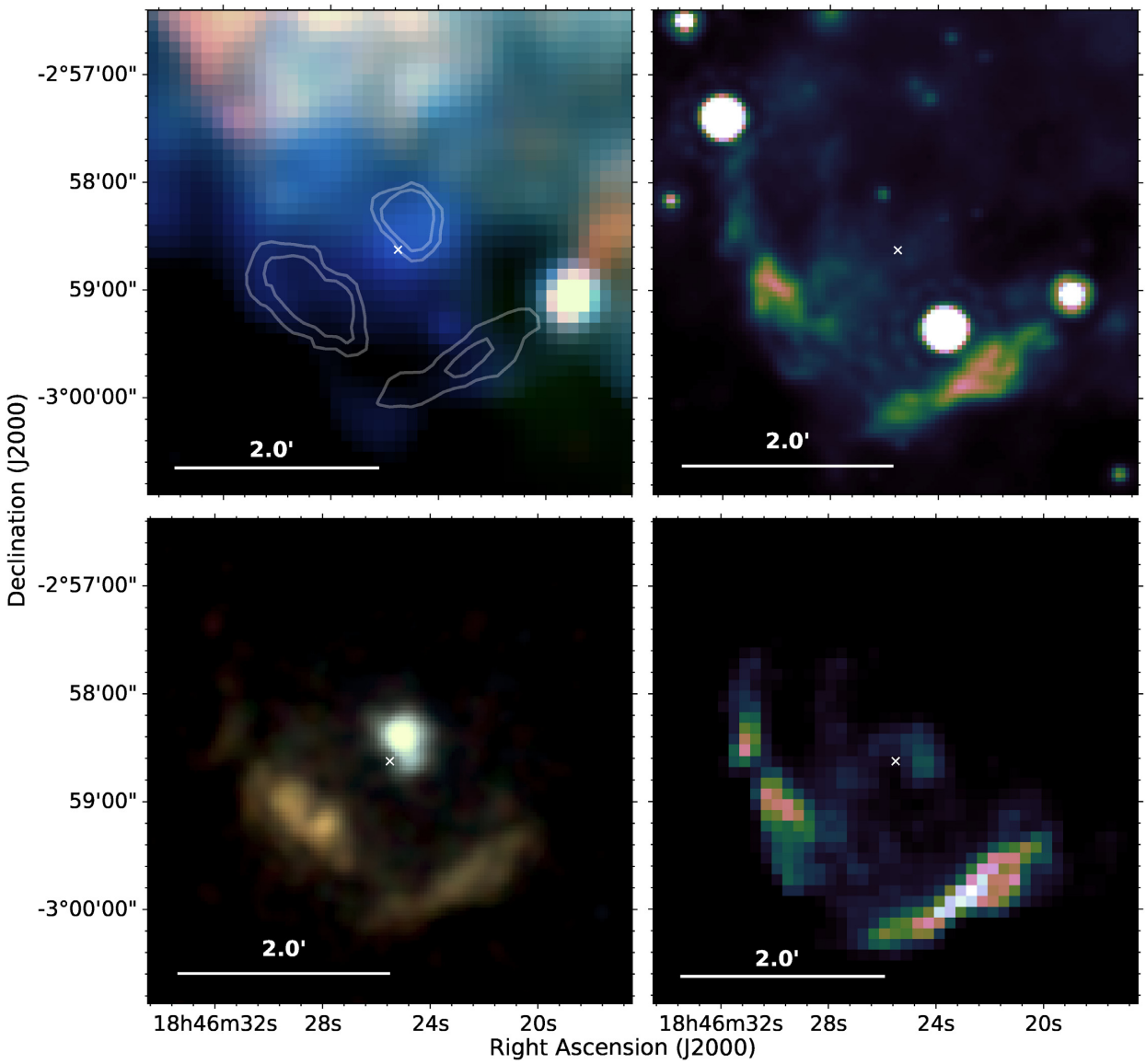

Figure 15. G29.7–0.3 (Kes 75) – *Top-left*: *Herschel* three-colour image with X-ray contours from *Chandra* overlaid. Dust is detected in a central clump at the same location as the pulsar and PWN. *Top-right*: *Spitzer* MIPS 24 μm image. *Bottom-left*: *Chandra* colour image (red = 1.0–1.7 keV, green = 1.7–2.6 keV, and blue = 2.6–8.0 keV). *Bottom-right*: VLA 20 cm radio image. The white crosses show the X-ray coordinates of the SNR centre.

by R06). It was suggested that the lack of IRAC emission from the shell is due to shock destruction of small dust grains (Morton et al. 2007). At 70 μm in Fig. 15 we detect a region of diffuse dust emission centred at $\alpha = 18^{\rm h}46^{\rm m}24.9^{\rm s}, \delta = -02^\circ58'30''$, at the same location as X-ray emission from the PWN and the central pulsar (Helfand, Collins & Gotthelf 2003a). At the longer *Herschel* wavelengths there is too much confusion to distinguish if there is any cold dust in the SNR. There is FIR emission from the shell region coinciding with a bright 24 μm structure, however this is much less bright and difficult to detect in some regions. The object detected at $\alpha = 18^{\rm h}46^{\rm m}19^{\rm s}, \delta = -02^\circ59'03''$ is a young stellar object (Veneziani et al. 2013).

3C 391, G31.9+0.0 (Fig. 16): This is a young mixed-morphology SNR with an incomplete radio shell structure (Goss et al. 1979). Both R06 and PG11 classified this SNR as a level 1 detection. R06 found MIR emission originating from shocked molecular gas at $\alpha = 18^{\rm h}49^{\rm m}23^{\rm s}, \delta = -00^\circ57'38''$ and $\alpha = 18^{\rm h}49^{\rm m}29^{\rm s}, \delta = -00^\circ55'00''$, at the ends of the SNR's bright semicircular radio shell. The southern patch is coincident with one of two 1720 MHz OH masers detected in the SNR where the remnant seems to be breaking into the edge of a molecular cloud (Frail et al. 1996). The MIR patches are well detected by *Herschel* in Fig. 16; the southern patch is detected at all *Herschel* bands, however the northern patch is detected only at 70 and 160 μm. Beyond these points, FIR emission extends into an arc around the northwestern shell in all *Herschel* bands, although there is confusion at bands other than 70 μm.

R06 discussed a bar of shocked, ionized gas from which both R06 and PG11 concluded that there was a contribution of [Fe II] 5.34 μm line emission. This bar coincides with the brightest part of the radio shell and is also detected in the FIR at 70 and 160 μm near to $\alpha = 18^{\rm h}49^{\rm m}16^{\rm s}, \delta = -00^\circ55'03''$. The FIR emission is likely associated with dust rather than line emission considering the high luminosity of dust at 70–160 μm as in the cases of the Crab, Cas A

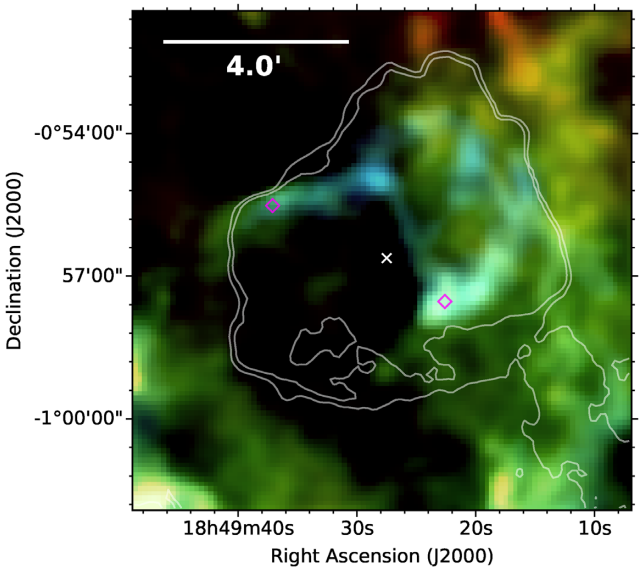

Figure 16. SNR 3C391 (G31.9+0.0) – *Herschel* three-colour image with X-ray contours overlaid. The two diamonds indicate the locations of the two OH masers (Frail et al. 1996). Dust is detected at the outer edges of the shock in a semicircular shell. The white cross shows the X-ray coordinates of the SNR centre.

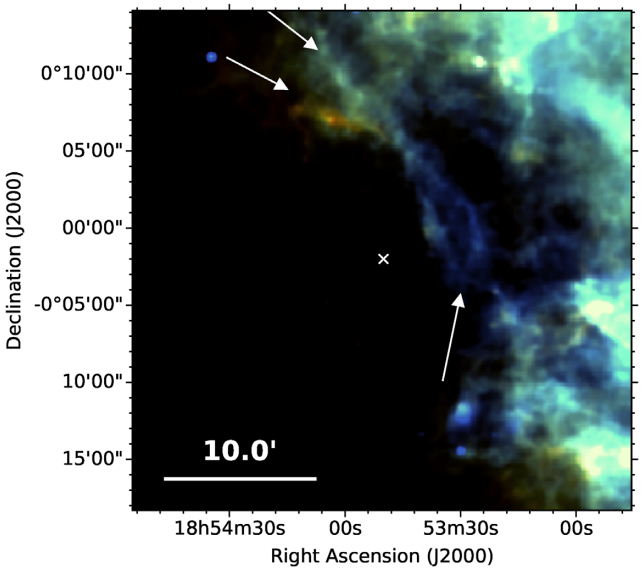

Figure 17. G33.2–0.6 – *Herschel* three-colour image. Dust is detected in filaments in an arc towards the western shell of the SNR, indicated by the lower arrow. Two filaments seem to extend to from this arc as indicated by the upper arrows; a filament extending to the north is detected in all *Herschel* wavebands, and a cooler filament extending to the north-east is detected in all but 70 μm. The white cross shows the radio coordinates of the SNR centre.

(Gomez et al. 2012b; De Looze et al. 2017), and three SNRs studied ourselves in Section 3.

G33.2–0.6 (Fig. 17): A partial shell is detected to the western edge of this remnant that has a higher temperature than the surrounding medium as seen in Fig. 17. This arc corresponds to the 1465 MHz radio structure detected by Dubner et al. (1996). Most noticeable are two filaments; the inner one is $\sim$5′ with a midpoint near $\alpha = 18^{\rm h}53^{\rm m}35^{\rm s}$, $\delta = -00^\circ00'36''$, and the outer filament is $\sim$15.5′ near

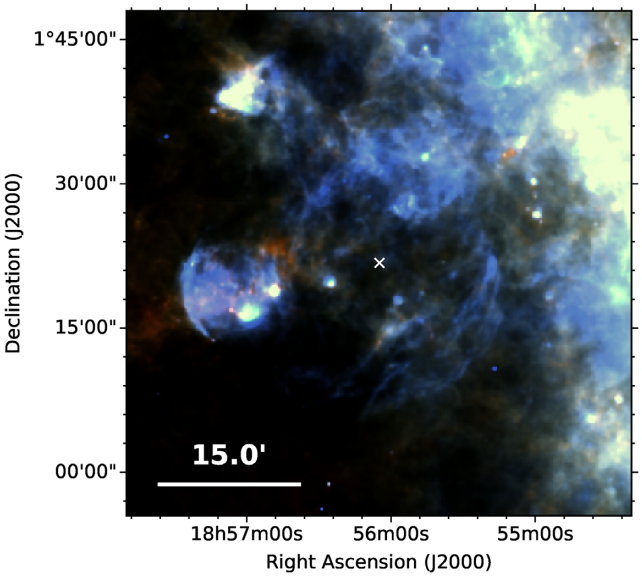

Figure 18. SNR W44 (G34.7–0.4) – *Herschel* three-colour image. Dust is seen in filaments at the outer edges of the shock and is brightest to the west. The bright patch of emission to the east is likely an H II region (Rho et al. 1994). The white cross shows the X-ray coordinates of the SNR centre.

to $\alpha = 18^{\rm h}53^{\rm m}43^{\rm s}$, $\delta = +00^\circ04'22''$. These filaments are detected at *Spitzer* wavelengths, although neither R06 nor PG11 classified this source as a clear detection. FIR emission is also detected at the location of the compact *IRAS* source (IRAS 18509−0015) to the south-west of the SNR at $\alpha = 18^{\rm h}53^{\rm m}29^{\rm s}$, $\delta = -00^\circ12'03''$. To the north of the remnant there are two filaments detected, one cooler that is visible in red in Fig. 17, and another warmer filament extending to the north that is visible in blue and is detected in all *Herschel* wavebands. Both of these filaments are outside of the region of radio emission; we therefore cannot confidently determine whether these are associated with the remnant.

Kes 79, G33.6+0.1: This mixed-morphology SNR is most likely in the Sedov–Taylor phase of evolution, with an age of 4.4–6.7 kyr (Zhou et al. 2016). CO observations suggest that the remnant is interacting with molecular clouds to the east (e.g. Green & Dewdney 1992; Zhou et al. 2016). PG11 detected 24 μm emission corresponding to the X-ray filaments to the east and the brightest X-ray contours.

Although there are FIR features that may correspond to the SNR (Figure A2) this isn't clear; the region is confused and there is extensive FIR emission from the local ISM. A circle of FIR emission of radius $\sim$0.66′ at $\alpha = 18^{\rm h}52^{\rm m}39^{\rm s}$, $\delta = +00^\circ41'59''$ coincides with an IR bubble (Simpson et al. 2012) and an X-ray dark region. There are also FIR point sources corresponding to MIR sources that may be protostars (Reach et al. 2006) in an infrared dark cloud along the eastern edge. There is no dust emission in the region of the X-ray point source.

W44, G34.7–0.4 (Fig. 18): This large core-collapse SNR has a well-defined radio shell that is centrally filled by thermal X-ray emission (Jones, Smith & Angelini 1993; Rho et al. 1994) and was a level 1 detection by both R06 and PG11. Similar to the MIR structure, the FIR dust emission traces the radio elliptical shell, although the FIR is fainter towards the south. At MIR wavelengths shocked H_2 is detected along the eastern border (Reach, Rho & Jarrett 2005) where the SNR is interacting with a molecular cloud (Giacani et al. 1997; Yusef-Zadeh et al. 2003; Reach et al. 2006).

We detect 70 and 160 μm emission at this edge, which is possibly from shock-heated dust. We also detect bright FIR filaments at the western edge, closely following the radio structure. There is some potential detection of emission at the longer *Herschel* wavebands, however the emission is much more confused. The patch of bright emission to the east, centred at $\alpha = 18^{h}57^{m}05^{s}, \delta = +01^{\circ}18'40''$ is probably an H II region (Rho et al. 1994). We do not detect emission in the region of the pulsar, PSR B1853 + 01, which is located at $\alpha = 18^{h}56^{m}10.65^{s}, \delta = +01^{\circ}13'21.3''$.

G35.6–0.4: Recently re-classified as an SNR rather than a H II region, this shell-type remnant is likely around 30 000 yr old and at a distance of 3.6 ± 0.4 kpc (Green 2009; Zhu et al. 2013). PG11 classed this as a level 1 detection although there is not a convincing likeness between IR and radio emission. There is FIR structure to the south-east of the SNR, which does not have a similar morphology to radio emission (Zhu et al. 2013). A 3.5′ rim of dust at $\alpha = 18^{h}58^{m}12^{s}, \delta = +02^{\circ}08'47''$ may be associated with the radio structure, although this is unclear.

FIR emission is detected from the planetary nebula PN G35.5–0.4 at $\alpha = 18^{h}57^{m}59.5^{s}, \delta = +02^{\circ}07'07''$ whose distance has been estimated as 3.8 ± 0.4 kpc (Zhu et al. 2013). There is also dust emission coinciding with a molecular clump towards the centre of the gamma-ray source HESS J1858 + 020 at $\alpha = 18^{h}58^{m}21^{s}, \delta = +02^{\circ}05'12''$ (HESS Collaboration 2008b). A YSO embedded in this clump probably belongs to a larger molecular cloud which is interacting with G35.6–0.4 and a nearby H II region (Paron et al. 2011).

3C 396, G39.2–0.3 (Fig. 19): There was a level 1 detection of this SNR by both R06 and PG11. Similar to the MIR detection described by R06, FIR emission from this SNR is mainly detected from three regions:

A bright region of emission in Fig. 19 at $\alpha = 19^{h}04^{m}26^{s}, \delta = +05^{\circ}27'55''$ (within the magenta circle) coincides with the radio blowout tail (see Patnaik et al. 1990, figs 1 and 2) that extends out of the east shell and over the top of the SNR. FIR emission from the tail is detected in the five *Herschel* bands. High radio polarization and bright emission in the longer *Herschel* channels is consistent with synchrotron-dominated FIR emission in the region. Cruciani et al. (2016) found a significant correlation between the FIR and radio, 1.5 GHz, emission in this region, although they could not rule out that this is due to diffuse interstellar emission.

Filamentary emission is detected on the western side of this remnant, near to $\alpha = 19^{h}03^{m}56^{s}, \delta = +05^{\circ}25'46$, across all of the *Herschel* bands, although at bands longer than 70 μm this is very confused with ISM emission. It is suggested that MIR emission at the same location originates from shocked, ionized gas (Reach et al. 2006), suggesting that the FIR emission in this region could originate from warm, shocked dust.

FIR emission is detected at all *Herschel* wavelengths to the east of the SNR in a region of very high radio polarisation. At 70 and 160 μm this is resolved into two filaments at $\alpha = 19^{h}04^{m}17^{s}, \delta = +05^{\circ}27'07''$ and $\alpha = 19^{h}04^{m}19^{s}, \delta = +05^{\circ}26'33''$ (bottom panel of Fig. 19).

W49B, G43.3–0.2 (Fig. 20): W49B is the first bipolar Type Ib/Ic SNR discovered in the Milky Way, which contributes to its rather unique radio barrel-hoop structure (Moffett & Reynolds 1994; Lopez et al. 2013). X-ray emission is dominated by ejecta emission that suggests that the SNR is young (Hwang et al. 2000). The radio/IR morphologies seem anticorrelated with the X-ray emission.

Both R06 and PG11 detected this SNR to level 1. The FIR emission at 70, 160, and 250μm in Fig. 20 follows the MIR and radio morphology. The emission is especially bright to the southwest

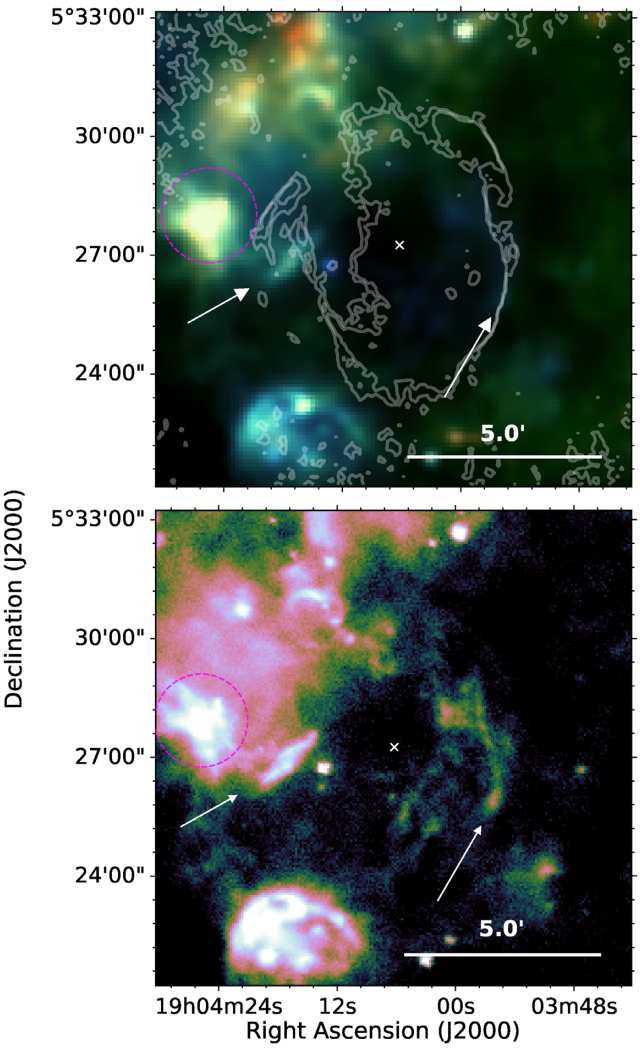

Figure 19. SNR 3C 396 (G39.2–0.3) – *Top: Herschel* three-colour image with radio (20 cm) contours overlaid. *Bottom: Herschel* 70 μm image. Within the magenta circle, FIR emission is detected at the location of a blowout tail detected at 1465 MHz (Patnaik et al. 1990). Filamentary dust is detected at the western outer edges of the shocks and in regions of very high radio polarisation, as indicated by the arrows. The white cross shows the X-ray coordinates of the SNR centre.

where there is a detection in all *Herschel* wavebands although in the longer wavebands it is very confused. At 70–250 μm we detect an ∼1′ filament of emission centred at $\alpha = 19^{h}11^{m}07^{s}, \delta = +09^{\circ}07'01''$. R06 detected MIR emission due to ionic shocks from this filament, as we detect FIR continuum emission, it is likely that this is from shock-heated dust. R06 also established that MIR emission in the outer shell to the east and southwest is from shocked molecular gas where the SNR is interacting with a molecular cloud that encapsulates the wind-blown bubble surrounding the SNR (Keohane et al. 2007).

G54.1+0.3 (Fig. 21): Described as a 'close cousin' of the Crab Nebula, this remnant has a central PWN and an IR shell 1.5′ from the pulsar (Koo et al. 2008). Timing measurements of the central pulsar suggest a characteristic age of 2900 yr (Camilo et al. 2002) and CO and HI observations suggest a distance of 6.2 kpc (Leahy, Tian & Wang 2008).

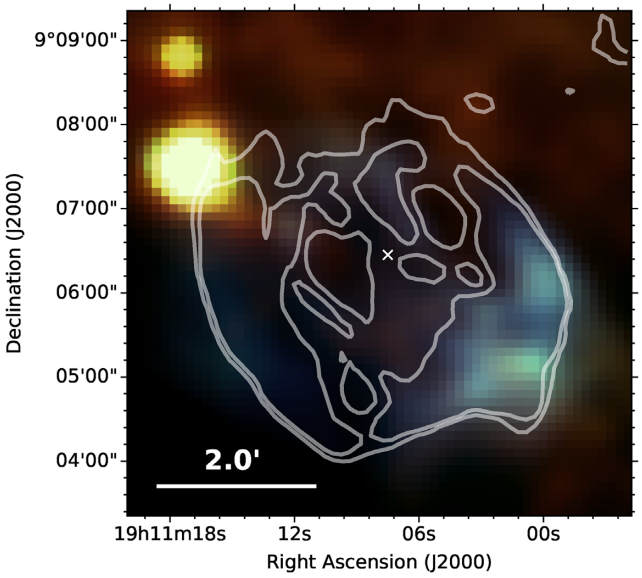

Figure 20. W49B (G43.3–0.2) – *Herschel* three-colour image overlaid with radio 20 cm contours. Shock heated dust is seen in filaments in a barrel-hoop structure. The white cross shows the X-ray coordinates of the SNR centre.

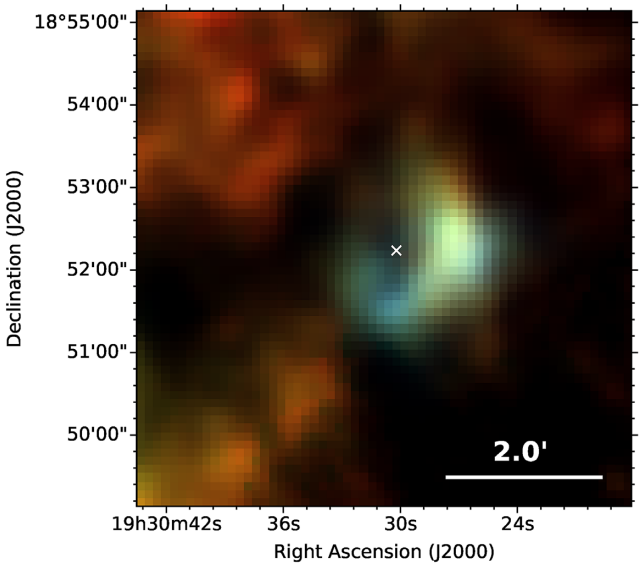

Figure 21. G54.1+0.3 – *Herschel* three-colour image with X-ray contours from *Chandra* overlaid. Dust is observed in a central region at the location of the PWN. The white cross shows the X-ray coordinates of the SNR centre. For details on the discovery of dust in this source, see Temim et al. (2017) and Rho et al. (2018).

Both R06 and PG11 classified this SNR as a level 3 detection, although there is bright 24 μm emission at the location of the PWN. Temim et al. (2017) detected an infrared shell to the south and west of the PWN. They completed a detailed analysis of MIR and FIR emission from the shell in the region of the PWN and found that their models require a minimum dust mass of 1.1 $\pm$ 0.8 $M_\odot$. Rho et al. (2018) fit the FIR-mm SED to derive a total dust mass of $0.08-0.9 M_\odot$ depending on the grain composition. It is thought that the reverse shock has not yet reached this shell, which might originate from dust in the SN ejecta potentially heated by early-type stars (Temim et al. 2010). However, the origin of the emission

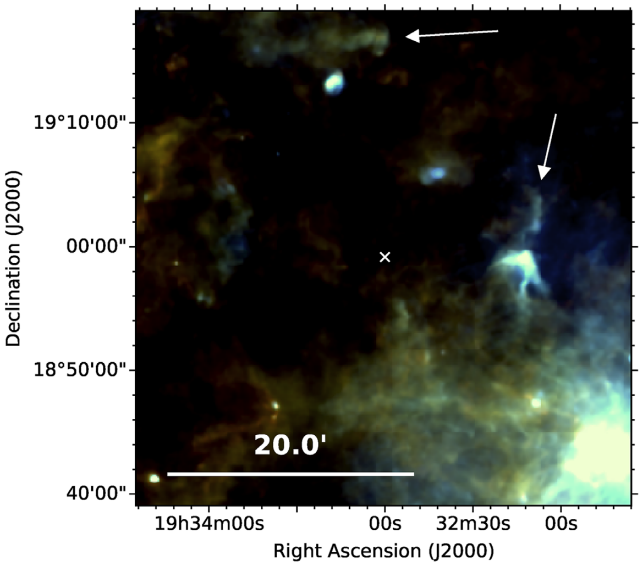

Figure 22. G54.4–0.3: *Herschel* three-colour image. Filaments of dust are observed at the outer edges of the shocks, as indicated by the white arrows. The white cross shows the X-ray coordinates of the SNR centre.

requires further investigation as Anderson et al. (2017) suggest that the structure is a mistakenly classified H II region, although faint, diffuse radio emission in the centre area may be associated with the SNR.

G54.4–0.3 (Fig. 22): This SNR is located in an extended cluster of young population I objects from which molecular material was blown in to a shell by stellar winds before the supernova exploded (Junkes, Furst & Reich 1992). R06 detected two MIR filaments likely corresponding to the location of shocks propagating into the bubble and/or molecular cloud, although their MIR colours are consistent with photo-dissociation regions (R06). The same filaments are detected by PG11 and across the five *Herschel* wavebands as shown in Fig. 22 at $\alpha = 19^{\rm h}32^{\rm m}08^{\rm s}$, $\delta = +19^\circ02'56''$ and $\alpha = 19^{\rm h}33^{\rm m}13^{\rm s}$, $\delta = +19^\circ16'20''$.

G55.0+0.3: This shell-type remnant is at an estimated distance of 14 kpc and is highly evolved, aged around 1.9×10^6 yr (Matthews et al. 1998). Like R06 and PG11 at MIR wavelengths, we detect an arc of FIR emission near to $\alpha = 19^{\rm h}32^{\rm m}05^{\rm s}$, $\delta = +19^\circ46'41''$, which could be associated with the eastern shell (Fig. A2). However, it is difficult to disentangle SNR and ISM emission, making an association unclear.

Kes 17, G304.6+0.1 (Fig. 23): This middle-aged SNR (28–64 kyr; Combi et al. 2010b) is interacting with several massive molecular clouds causing bright filaments to the west by shock compression (Combi et al. 2010b). R06 attributed MIR emission in the shell to molecular shocks. As shown in Fig. 23, there is bright FIR emission in this region across all of the *Herschel* bands which is likely due to dust heated by shocked gas. There is also some diffuse 70 μm emission along the southern ridge and longer wavelength emission towards the south east, although it is unclear whether this is associated with the SNR.

G310.8–0.4 (Fig. 24) This SNR has a bright eastern radio shell at 0.843 GHz, which is less defined to the west (Whiteoak & Green 1996). R06 and PG11 detected emission coinciding with radio contours to the south-east and part of the structure in the north-west. A 4.4′ rim of diffuse FIR emission is detected near $\alpha = 14^{\rm h}00^{\rm m}44^{\rm s}$, $\delta = -62^\circ19'03''$, which may be associated with

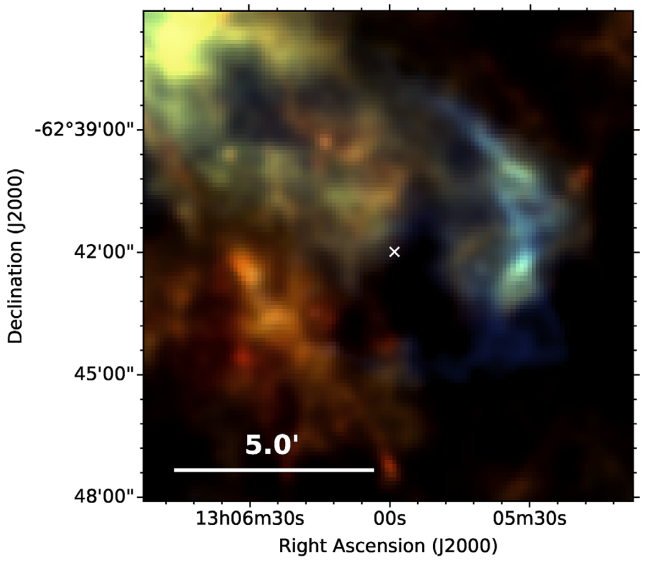

Figure 23. Kes 17 (G304.6+0.1) - *Herschel* three-colour image. An arc of dust is seen on filaments to the western edge of the outer shocks. The white cross shows the radio coordinates of the SNR centre from Green (2014).

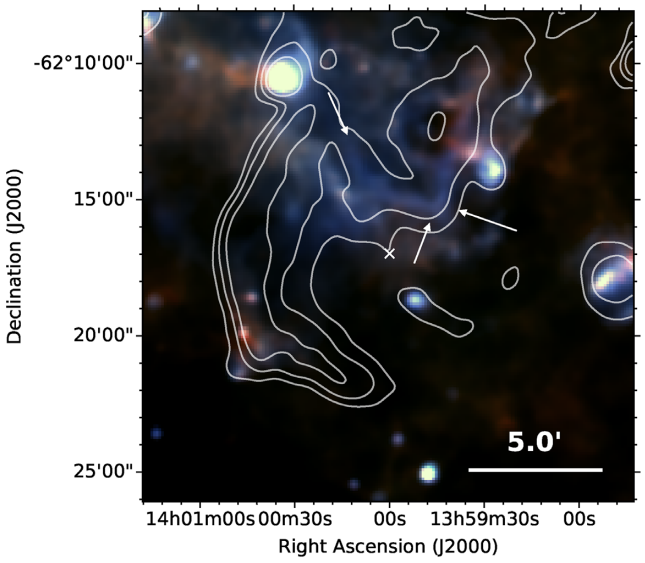

Figure 24. G310.8–0.4 – *Herschel* three-colour image with radio contours from MOST overlaid. The arrows indicate FIR emission that correlates with radio structure.

the SNR (Fig. A2). However, this is unclear as the region is very confused in FIR and potentially related emission cannot be distinguished from the local ISM. A filament of FIR emission to the north of the SNR seems to correlate with radio emission, as indicated by the arrows.

G311.5–0.3 (Fig. 25): This shell-type SNR is clearly detected by *Herschel* in Fig. 25 as a shell of dust emission similar to that detected by R06 and PG11. Detection of H_2 emission suggests that this SNR is interacting with molecular clouds (Andersen et al. 2011) and R06 suggested that MIR emission is from shocked gas. At 70 μm the FIR shell is brightest along the south west ridge, especially near $\alpha = 14^{h}05^{m}22^{s}, \delta = -61^{\circ}58'06''$. However, in the longer wavelength *Herschel* images the brightest emission is towards the eastern and south-eastern edge of the shell. Like R06

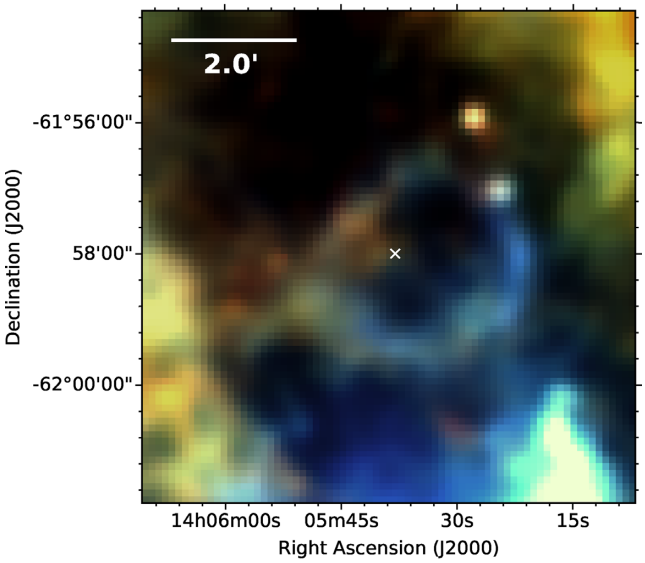

Figure 25. G311.5–0.3 – *Herschel* three-colour image. A ring of dust emission is detected at the outer edges of the shocks. The white cross shows the X-ray coordinates of the SNR centre.

we detect bright sources near $\alpha = 14^{h}05^{m}24.3^{s}, \delta = -61^{\circ}57'07''$ and $\alpha = 14^{h}05^{m}23.5^{s}, \delta = -61^{\circ}56'58''$, although at the *Herschel* resolution these two sources are unresolved.

RCW 103, G332.4–0.4 (Fig. 26): This shell-type remnant is at a distance of ∼3.1 kpc and the expansion velocity suggests an age of around 2000 yrs (Carter et al. 1997). The associated compact central object, 1E 161348–5055, which does not have a detected PWN (e.g. Tuohy & Garmire 1980; Reynoso et al. 2006) is most likely a magnetar with an extremely long period of 6.67 hrs (Rea et al. 2016). X-ray emission across the SNR is dominated by shocked CSM with weaker emission from metal-rich ejecta and has been suggested to have had an ∼18–20 $M_{\odot}$ progenitor with high mass-loss rate (Frank et al. 2015). The SNR is interacting with a molecular cloud on its southern side (Oliva, Moorwood & Danziger 1990; Oliva et al. 1999).

There is an ∼1.7′ rim of 70 μm emission along the southern edge of the SNR in Fig. 26, near $\alpha = 16^{h}17^{m}36^{s}, \delta = -51^{\circ}06'13''$, which is undetected in the other *Herschel* bands. This coincides with X-ray and MIR structure detected by R06 and PG11 and is at a higher temperature than FIR structures to the east. The more resolved IRAC image suggests that this region consists of two emitting areas dominated by ionic and molecular shocks.

G337.2–0.7: PG11 detected 24 μm emission from filaments in this SNR that form two shell-type features, corresponding to X-ray structure. Although there is some emission at 70 μm (Fig. A2) it is unclear whether this is associated with the SNR. There is a FIR region to the north-east coinciding with 24 μm emission, however this does not correspond to the X-ray structure and it is unlikely to be associated with the SNR.

G340.6+0.3 (Fig. 27): This shell-type SNR is at a distance of 15 kpc, on the other side of the Galaxy (Kothes & Dougherty 2007). Like PG11, we detect a shell of dust, as seen in Fig. 27, which correlates with the 1.4 GHz radio shell (Caswell et al. 1983). This emission is not seen in the IRAC wavebands (Fig. A2); some MIR emission is detected in the region but is not clearly associated with the SNR.

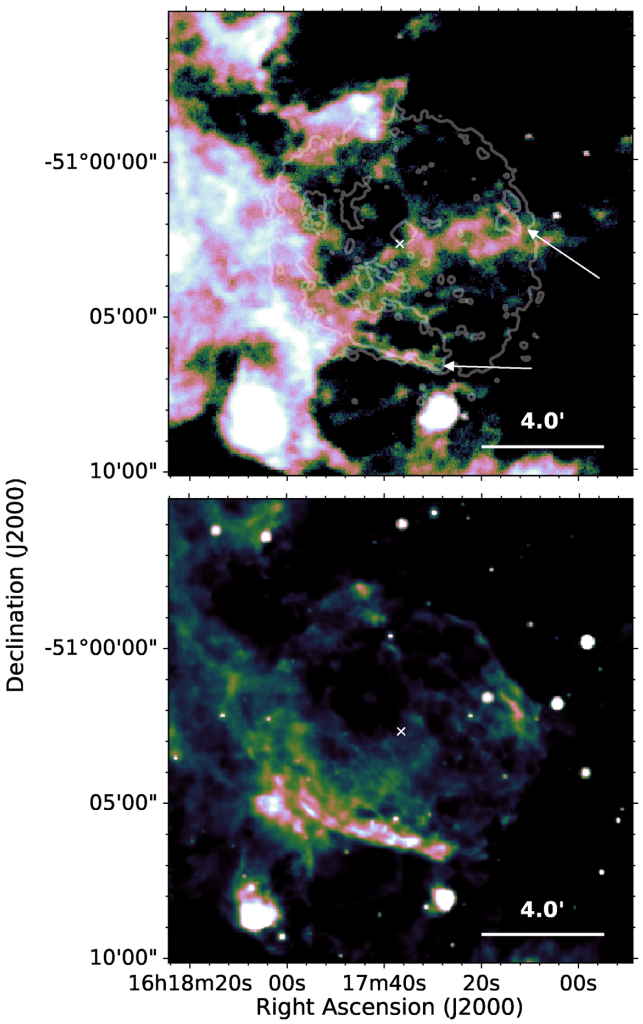

Figure 26. RCW 103, G332.4–0.4 – *Top*: *Herschel* 70 μm image with X-ray contours overlaid. An arc of dust in the south coincides with X-ray structure and filaments to the north-west correspond with dust emission at 24 μm, as indicated by the arrows. *Bottom*: *Spitzer* MIPS 24 μm image. The white cross shows the X-ray coordinates of the SNR centre.

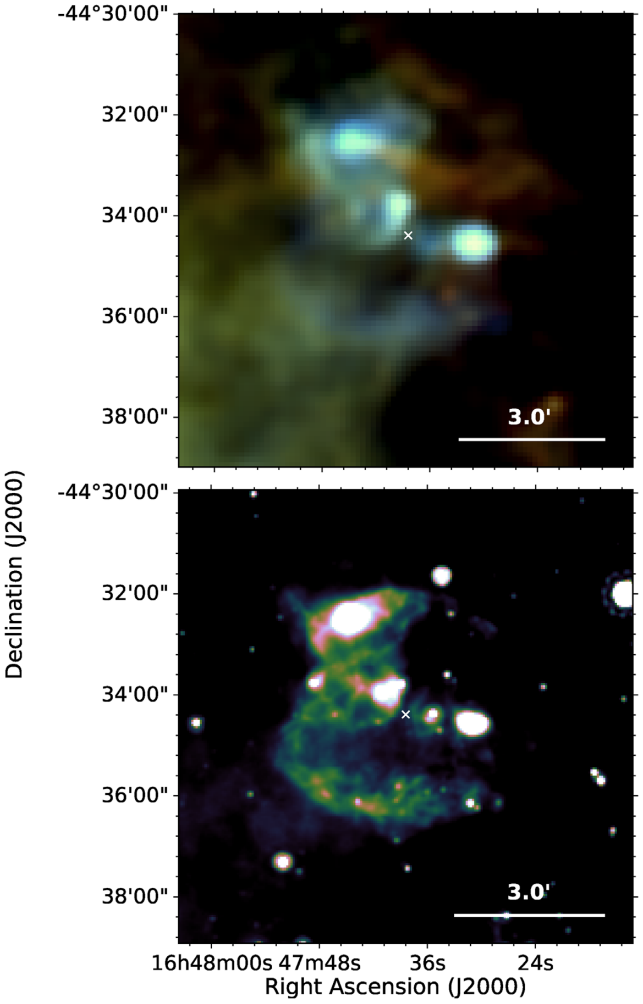

Figure 27. G340.6+0.3 – *Top*: *Herschel* three-colour image. A shell of dust is seen, which is brightest along the southern edge. *Bottom*: *Spitzer* MIPS 24 μm image. The white cross shows the X-ray coordinates of the SNR centre.

G344.7–0.1 (Fig 28): This relatively young SNR (∼3000 yr) has an estimated distance of 14 kpc (Yamaguchi et al. 2012) and is classified as a mixed-morphology remnant, having thermal X-ray emission that completely fills the radio shell (Yamauchi et al. 2005; Combi et al. 2010a; Giacani et al. 2011). The radio emission is brightest towards the northwestern side where the remnant is expected to be interacting with a molecular cloud (Combi et al. 2010b). Strong Fe K-shell ejecta emission and the abundance pattern of α-elements suggest that this is a Type Ia SNR (Yamaguchi et al. 2012). The SNR contains a large mass of hydrogen ($\gtrsim$150 $M_\odot$), which implies that the SNR is dominated by swept-up ISM.

R06 detected an irregular MIR structure to the north of the SNR originating from shocked ionized gas, which coincides with a central radio peak (Giacani et al. 2011). We also detect FIR emission from this structure in Fig 28, centred at $\alpha = 17^h03^m55^s, \delta = -41°40'43''$, although the *Herschel* detection is less resolved. It is likely that this emission arises from the interaction between the SN shock and a molecular cloud in front of the SNR (Giacani et al. 2011).

G345.7–0.2: This SNR has a faint disc radio morphology and a peak close to the pulsar PSR J1707–4053, which is probably unrelated (Taylor, Manchester & Lyne 1993; Whiteoak & Green 1996). We detect a diffuse region of 70 μm emission (Fig. A2) centred at $\alpha = 17^h07^m39^s, \delta = -40°54'31''$, extending roughly 2′ which correlates with MIPS 24 μm and 0.843 GHz radio emission (Whiteoak & Green 1996). We find no other evidence of SNR-related emission in the region. We suggest that the SNR centre is offset from that of Green (2014) and the bar detected could be part of a structure extending to the east.

G346.6–0.2: R06 detected a narrow rim of emission connecting three OH 1720 MHz masers along the southern shell. There is FIR emission that potentially corresponds to this structure (Fig. A2), however the region is very confused as there is extensive dust emission to the north and west of the SNR.

G348.5–0.0 (Fig. 29): Originally thought to be a jet associated with CTB 37A, this was classified by Kassim, Weiler & Baum (1991) as a separate partial shell remnant. H I 21-cm absorption measurements suggest that this remnant is at a distance of ≤6.3 kpc (Tian & Leahy 2012). In Fig. 29 we detect an ∼1.7′ arc of dust emission centred at $\alpha = 17^h15^m03.5^s, \delta = -38°33'30''$. This is detected across all *Herschel* wavebands, although it is very con-

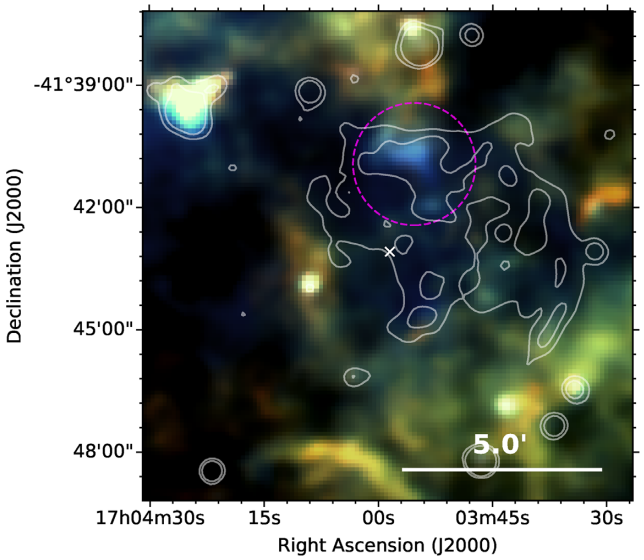

Figure 28. G344.7–0.1 – *Herschel* three-colour image. A region of dust emission is detected to the north of the remnant (within the magenta circle), centred at $\alpha = 17^{\rm h}03^{\rm m}55^{\rm s}, \delta = -41^{\circ}40'43''$. MIPS 24 μm contours are overlaid. The white cross shows the X-ray coordinates of the SNR centre.

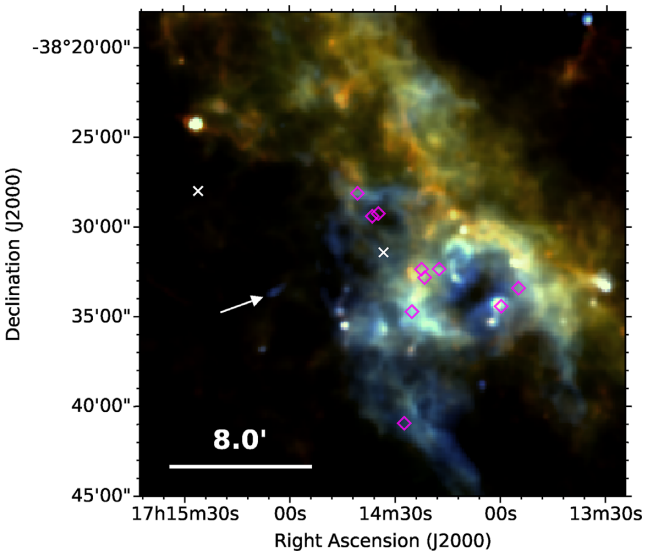

Figure 29. G348.5–0.0 and CTB 37A, G348.5+0.1 – *Herschel* three-colour image. The diamonds indicate the locations of OH 1720 MHz masers (Frail et al. 1996). Dust emission from G348.5–0.0 is detected as indicated by the arrow, and emission from CTB 37A is detected along the north-western edges of the remnant. The white crosses show the radio and X-ray coordinates of the centres of G348.5–0.0 (north-east) and G348.5+0.1 (south-west), respectively.

fused for $\lambda > 160\,\mu$m. R06 suggested that this MIR emission is dominated by emission lines from shocked gas.

The OH 1720 MHz masers at $\alpha = 17^{\rm h}14^{\rm m}34.8^{\rm s}, \delta = -38^{\circ}29'16''$ and $\alpha = 17^{\rm h}14^{\rm m}36.5^{\rm s}, \delta = -38^{\circ}29'25''$ have a significantly different velocity to the other eight in the region which are associated with CTB 37A (Frail et al. 1996). It is suggested that these two are related to a nearby molecular cloud (Reynoso & Mangum 2000) lying to the west of G348.5–0.0 with which the remnant is likely to be interacting. We do not detect FIR emission at the location of these masers.

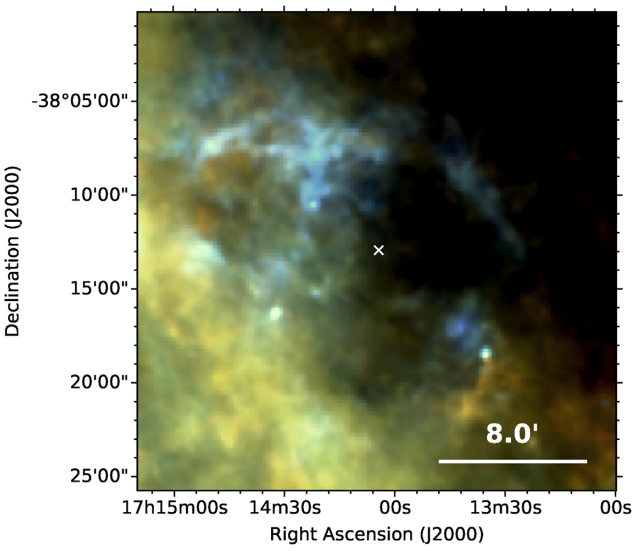

Figure 30. CTB 37B, G348.7+0.3 – *Herschel* three-colour image. Dust emission is detected in a partial shell structure around the northern edge of the remnant. The white cross indicates the X-ray coordinates of the SNR centre.

CTB 37A, G348.5+0.1 (Fig. 29): Recently classified as a mixed morphology remnant (Sezer et al. 2011; Yamauchi et al. 2014a), this SNR has a radio shell-like structure in the north and a 'breakout' to the south-west, and has thermally dominated central X-ray emission. At a distance in the range of 6.3–9.5 kpc, its proximity to both G348.5–0.0 and CTB 37B is coincidental (Tian & Leahy 2012). There are eight OH 1720 MHz masers associated with the SNR that have a similar velocity to incident CO (1–0) clouds detected by Reynoso & Mangum (2000), which are to the north-west and centre of the SNR.

The *Herschel* emission in Fig. 29 is very confused. Similar to R06, we detect dust emission along the northern edge in an ~4.3′ arc centred at $\alpha = 17^{\rm h}14^{\rm m}35^{\rm s}, \delta = -38^{\circ}28'22''$ and filaments along the western edge near to $\alpha = 17^{\rm h}14^{\rm m}46^{\rm s}, \delta = -38^{\circ}32'33''$. Emission in the northern region coincides with an OH 1720 MHz maser and is suggested by R06 to originate from shocked molecular gas where the SNR has encountered very dense gas. We also detect dust emission in the region of the 'breakout' structure to the south of the SNR.

CTB 37B, G348.7+0.3 (Fig. 30): This relatively young (~4900 yr; HESS Collaboration 2008b) SNR has a non-thermal radio shell (Whiteoak & Green 1996) and a magnetar that is slightly off-centre (Halpern & Gotthelf 2010). 21 cm H I absorption indicates a distance of ~13.2 kpc (Tian & Leahy 2012).

The region around the SNR is confused due to bright emission from IR bubbles at $\alpha = 17^{\rm h}14^{\rm m}38.2^{\rm s}, \delta = -38^{\circ}10'18''$ and $\alpha = 17^{\rm h}13^{\rm m}40.3^{\rm s}, \delta = -38^{\circ}17'33''$. We detect dust emission in Fig. 30 around the northern edge of the SNR, which coincides with the radio structure and is at a higher temperature than the surrounding medium.

G349.7+0.2 (Fig. 31): The radial velocities of OH 1720 MHz masers suggest that this shell-type SNR is at a large distance of 22 kpc (Frail et al. 1996), making it one of the most X-ray luminous Galactic remnants (Slane et al. 2002). X-ray temperature fits give an age of 2800 yr. The presence of OH 1720 MHz masers and shocked molecular gas imply that the SNR is interacting with a molecular cloud. The MIR SNR shell is much brighter to the eastern

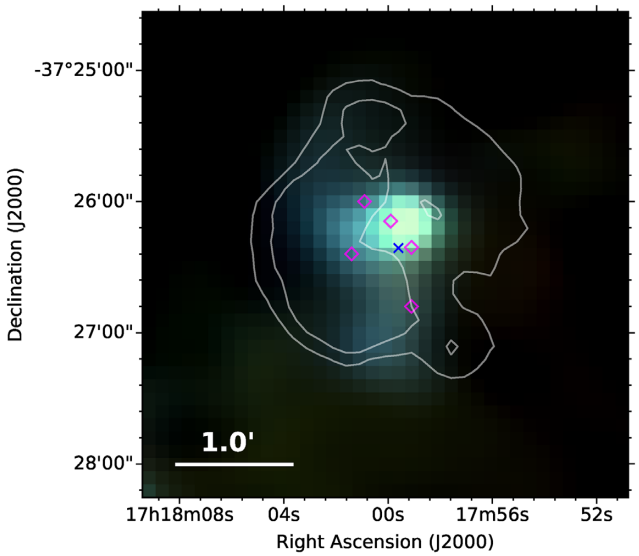

Figure 31. G349.7+0.2 – *Herschel* three-colour image with X-ray contours overlaid. The five OH masers are indicated by diamonds (Frail et al. 1996). Dust emission is observed at the western edge, where the remnant is interacting with a dense cloud. The blue cross shows the X-ray coordinates of the SNR centre.

side where a shock is propagating into the edge of a roughly cylindrical cloud (Reach et al. 2006). Like the MIR, the FIR emission in Fig. 31 peaks in the region of the OH 1720 MHz masers, near $\alpha = 17^{\rm h}18^{\rm m}00^{\rm s}, \delta = -37^{\circ}26'09''$.

3 THE MASS OF DUST IN G11.2–0.3, G21.5–0.9, AND G29.7–0.3

As discussed in Section 2.2, we detect four SNRs with dust in the central region associated with PWN-heated ejecta. The dust mass in G54.1+0.3 has been studied in detail, and so in this section we determine the dust masses for the three new PWNe detected in this paper (G11.2–0.3, G21.5–0.9, and G29.7–0.3).

The flux density for the central region (PWN) of each SNR was estimated using aperture photometry on MIR-FIR images from *Spitzer* MIPS (24 μm) and *Herschel*. The IRAC images are not used as we do not see emission from the SNRs in the region of the PWN in these wavebands and the measured emission is dominated by unrelated point sources. Apertures of 1.9′, 1.7′, and 1.2′ in diameter were centred at $\alpha = 18^{\rm h}11^{\rm m}29^{\rm s}, \delta = -19^{\circ}25'54'', \alpha = 18^{\rm h}33^{\rm m}34.2^{\rm s}, \delta = -10^{\circ}34'18.5''$, and $\alpha = 18^{\rm h}46^{\rm m}25^{\rm s}, \delta = -02^{\circ}58'30''$ for G11.2–0.3, G21.5–0.9, and G29.7–0.3 respectively.

The background ISM level for G21.5–0.9 was estimated using an annulus around the source as the local environment seems reasonably uncluttered. For G11.2–0.3 and G29.7–0.3, eight apertures were placed around the SNRs so as to avoid the shell and the bright cloud to the south of G11.2–0.3, and to avoid the young stellar object to the west of G29.7–0.3. Areas were selected to cover a range of flux levels to account for fluctuations in the ISM within the image cut-out. The background-subtracted fluxes are given in Table 3. Due to large variations in the ISM level, the background subtraction is the largest source of uncertainty in our estimation of dust mass.

Flux calibration uncertainties are assumed as a percentage of the measured flux in each band; that is 4 per cent for MIPS (Engelbracht et al. 2007), 7 per cent for PACS (Balog et al. 2014), and 5.5 per cent for SPIRE data (Bendo et al. 2013). Uncertainty in the ISM level is estimated as the standard deviation of the background ISM values.

Table 3. Background subtracted flux measured for each SNR at FIR wavelengths.

Wavelength, μm	Flux, Jy		
	G11.2–0.3	G21.5–0.9	G29.7–0.3
24	5.6 ± 0.3	0.19 ± 0.02	0.20 ± 0.03
70	47.7 ± 6.7	4.1 ± 0.3	5.6 ± 1.0
160	71.9 ± 15.7	6.6 ± 0.7	3.2 ± 4.0
250	26.6 ± 5.5	3.0 ± 0.9	0.55 ± 2.10
350	10.1 ± 3.0	1.5 ± 0.8	0.19 ± 1.15
500	2.3 ± 0.9	1.2 ± 0.4	0.02 ± 0.20

3.1 Synchrotron emission

A power-law synchrotron radiation spectrum, from charged particles accelerated in a magnetic field, can be detected across the electromagnetic spectrum. The contribution varies across SNR type. PWNe and Crab-like remnants tend to have a very flat radio spectrum and a steeper X-ray spectrum due to synchrotron losses, whereas shell-type SNRs have a much steeper radio spectrum.

In order to estimate the dust mass, first non-thermal synchrotron emission must be removed from the IR fluxes. The synchrotron flux density at a frequency, ν, can be fitted by equation (1),

$$S_\nu = S_{\nu_0}\left(\frac{\nu}{\nu_0}\right)^\alpha \quad (1)$$

where S_{ν_0} is the synchrotron flux density at frequency ν_0, and α is the spectral index that describes the flux density dependence on frequency. We use a least squares fitting routine to estimate α. Like the Crab Nebula, the power-law slope may break in the FIR region (e.g. Arendt et al. 2011; Gomez et al. 2012b), in which case we would be overestimating the synchrotron contribution to the MIR and FIR fluxes.

The uncertainty in α is estimated using a Monte Carlo technique by producing 1000 sets of normally distributed radio flux values, using the measured flux at each frequency as mean and flux uncertainty as standard distribution. Fitting a power law to each set gives 1000 values of α and the standard deviation is used as the uncertainty in the estimated value.

The integrated synchrotron flux values for the SNR PWN regions and spectral index from the fit are given in Table 4. A least squares fit to G11.2–0.3 radio data (Kothes & Reich 2001) of the central compact object gives a spectral index of $\alpha = -0.10 \pm 0.08$. A single power law cannot fit the spectra for G21.5–0.9 (Salter et al. 1989b) as the slope breaks at 40 GHz due to synchrotron losses. Fitting to radio data between 70 and 143 GHz (Salter et al. 1989a, 1989b; Planck Collaboration XXIX 2016), *Spitzer* MIPS (24 μm) and *Herschel* (500 μm) data, gives a spectral index of $\alpha = -0.53 \pm 0.01$. Whereas at lower frequencies (Morsi & Reich 1987; Bietenholz & Bartel 2008), the fitting routine gives a flat spectral index of $\alpha = -0.032 \pm 0.034$. A least squares fit to radio data of the Crab-like component of G29.7–0.3 (Salter et al. 1989b) gives a spectral index of $\alpha = -0.43$. It has been suggested that there may be a spectral break at around 55 GHz, in which case our synchrotron flux in FIR wavebands will be overestimated (Bock & Gaensler 2005).

The synchrotron contribution to the SNR SEDs is only significant for G21.5–0.9, for which it contributes between 9.5 and 96.7 per cent (160 and 500 μm, respectively) of the background subtracted flux

Table 4. The synchrotron flux measured for each SNR at radio wavelengths, and estimated synchrotron flux at Spitzer and Herschel bands.

SNR	Frequency (GHz)	Flux (Jy)	Ref	Spectral Index [a]	Wavelength (μm)	Estimated Synchrotron Flux (Jy)[b]
G11.2–0.3	1.4	0.11 ± 0.02	1	-0.10 ± 0.08	24	$(43 \pm 40) \times 10^{-3}$
	32	0.08 ± 0.02	1		70	$(46 \pm 44) \times 10^{-3}$
					160	$(48 \pm 44) \times 10^{-3}$
					250	$(50 \pm 44) \times 10^{-3}$
					350	$(51 \pm 44) \times 10^{-3}$
					500	$(52 \pm 43) \times 10^{-3}$
G21.5–0.9	327×10^{-3}	7.3 ± 0.7	2	-0.032 ± 0.038	24	0.23 ± 0.05
	1.43	7.0 ± 0.4	2		70	0.40 ± 0.08
	5	6.7 ± 0.3	3		160	0.63 ± 0.13
	32	5.6 ± 0.3	4	-0.56 ± 0.02	250	0.80 ± 0.16
	70	4.3 ± 0.6	5		350	0.95 ± 0.18
	84.2	3.9 ± 0.7	6		500	1.16 ± 0.22
	90.7	3.8 ± 0.4	7			
	100	2.7 ± 0.5	5			
	141.9	2.5 ± 1.2	7			
	143	3.0 ± 0.4	5			
G29.7–0.3	1.4	0.35	6	−0.43	24	9.64×10^{-3}
	4.9	0.25	6		70	15.2×10^{-3}
	5.0	0.28	8		160	21.7×10^{-3}
	15	0.17	6		250	26.3×10^{-3}
	89	0.08	9		350	30.4×10^{-3}
					500	35.4×10^{-3}

Notes.
[a]The spectral index is estimated by fitting a power law to the radio fluxes on the same line and below.
[b]The FIR synchrotron flux is estimated by extrapolating the fitted power law to FIR wavelengths. Radio fluxes for the core are taken from: [1]Kothes & Reich (2001); [2]Bietenholz et al. (2011); [3]Bietenholz & Bartel (2008); [4]Morsi & Reich (1987); [5]Planck Collaboration XXXI (2016); [6]Salter et al. (1989b); [7]Salter et al. (1989a); [8]Becker & Helfand (1984); and [9]Bock & Gaensler (2005).

at each wavelength. For G29.7–0.3, the contribution at 500 μm is ∼59 per cent, however for the other wavebands it is less than 9 per cent, and for G11.2–0.3 the contribution in all wavebands it is less than 3.5 per cent.

3.2 Dust emission

After removing the synchrotron contribution from the SNR SEDs, we assume that the remaining thermal FIR flux takes the form of a modified blackbody:

$$F_\nu = \frac{M_{\rm dust} B_\nu(T) \kappa_\nu}{D^2}, \tag{2}$$

where F_ν is the flux at a given wavelength, $M_{\rm dust}$ is the mass of dust, $B_\nu(T)$ is the Planck function at temperature T, κ_ν is the dust mass absorption coefficient, and D is the distance to the source. The dust mass absorption coefficient, κ_ν, describes the effective surface area for extinction per unit mass:

$$\kappa_\nu = \frac{3 Q_\nu}{4 a \rho}, \tag{3}$$

where a is the dust grain radius, ρ is the grain material density, and Q_ν describes the emission efficiency and is dependent on both the frequency and the material type. The frequency dependence of κ_ν is given by

$$\kappa_\nu = \kappa_{\nu_0} \left(\frac{\nu}{\nu_0} \right)^\beta, \tag{4}$$

where β is the dust emissivity index, which describes how the emissivity varies with frequency. In this study we assume $\kappa_{\lambda_0} = 0.07 \pm 0.02$ m^{2}kg^{-1} for $\lambda_0 = 850$ μm (Dunne et al. 2000; James et al. 2002; Clark et al. 2016). In this function we assume that κ_ν can be estimated using a constant emissivity index of $\beta = 1.9$ (indicative of normal interstellar dust grains; Planck Collaboration XIV 2014).

The mass and temperature of the dust in the remnants are evaluated by a least squares fit to the flux values at wavelengths between 24 and 500 μm; we attempt both a single and double temperature modified blackbody fit. In order to derive physical estimates, the temperature and mass are constrained. A cold dust component must have a temperature of $15 < T_{\rm c} < 50$K, a warm component must have a temperature of $50 < T_{\rm w} < 150$K, and there must be a positive dust mass. We assume distances of 4.4 (Green 2004), 4.7 (Camilo et al. 2006), and 10.6 kpc (Su et al. 2009) for G11.2–0.3, G21.5–0.9, and G29.7–0.3, respectively. The best-fitting SEDs for all three PWNe are shown in Figs 32–34.

The 1σ uncertainties in the derived mass and temperature are estimated in a similar way to the uncertainty in α in Section 3.1. A modified blackbody is fit to 1000 sets of flux values to give distributions dust mass and temperature estimates. The uncertainties in the fit parameters are taken as the 16th and 84th percentiles. The largest source of uncertainty is the background subtraction; there is a large variation in the ISM level across the regions surrounding the SNRs making an estimate of the ISM contribution very uncertain. The best fit and median values derived for dust temperature and mass are shown in Table 5.

G11.2–0.3: We find that the thermal FIR emission between 24 and 500 μm for this SNR is best described by the sum of two modified blackbodies with best-fitting parameters for the cold temperature $T_{\rm c} = 27.3$ K, and warm temperature $T_{\rm w} = 180$ K. The cold component requires a best-fitting mass of $M_{\rm d} = 0.9\,{\rm M}_\odot$ and the warm component requires a mass of $M_{\rm d} = 7.9 \times 10^{-6}\,{\rm M}_\odot$, as seen in Fig. 32.

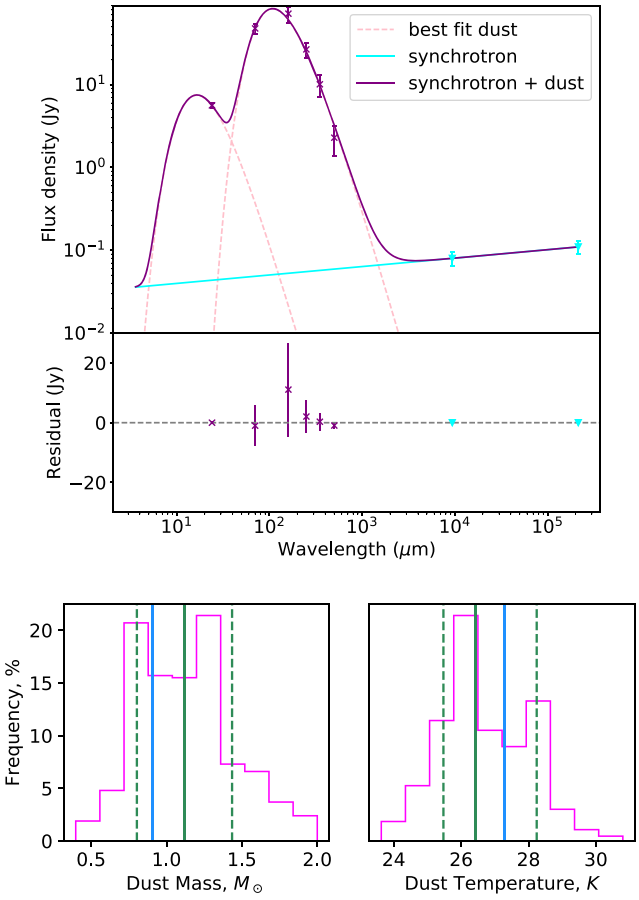

Figure 32. *Top*: Far-infrared SED of G11.2–0.3. The dashed pink lines are the two-temperature components fitted to the FIR fluxes. The solid cyan line is the synchrotron component fit to the radio flux of the compact object (cyan points). The solid purple line is the total SED of all components. *Bottom*: The distribution of source masses obtained by the Monte Carlo routine where SEDs were fit to 1000 normally distributed samples of flux values. The dashed green lines indicate the 1σ uncertainties and the solid green line is the median value. The solid blue line indicates the best-fitting value. The best-fitting and median values derived for dust temperature and mass are shown in Table 5.

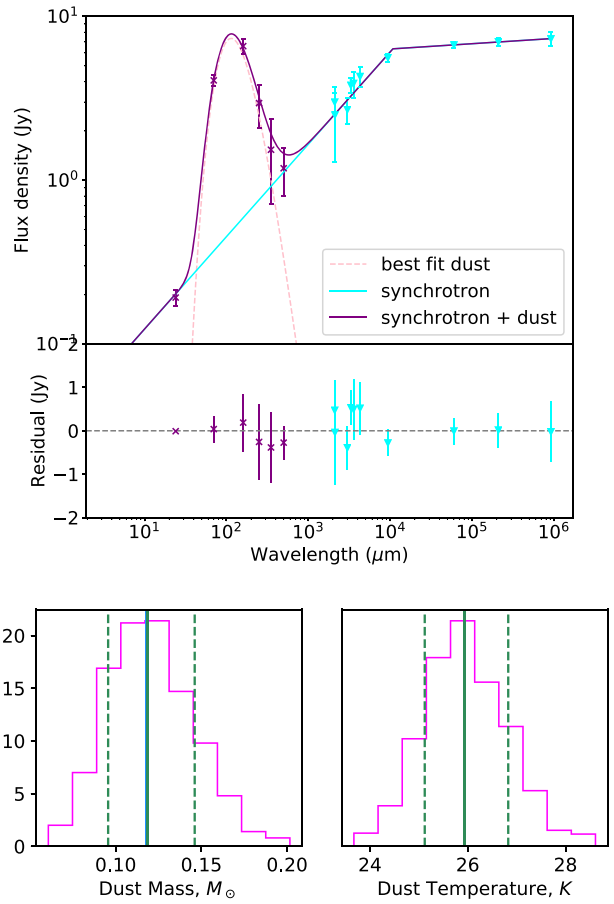

Figure 33. *Top*: Far-infrared SED of G21.5–0.9. *Bottom*: The distribution of source masses obtained by the Monte Carlo routine where SEDs were fit to 1000 normally distributed samples of flux values. The colour schemes are the same as for Fig. 32. The best-fitting and median values derived for dust temperature and mass are shown in Table 5.

There is large uncertainty in the mass and temperature of the warmer dust component as this peak mostly depends only on the 24 μm flux. This makes the position of the SED peak extremely uncertain, giving a wide range of possible temperatures and masses. The Monte Carlo method gives a skewed distribution of possible values for the cold dust mass and temperature. There is a tail of high dust masses, skewing the median to values > 1 M$_\odot$.

G21.5–0.9: We find that the global thermal emission in this SNR is well described by a single temperature dust component with a best-fitting temperature of $T = 25.9$ K and best-fit mass of $M_\mathrm{d} = 0.12$ M$_\odot$ as seen in Fig. 33. The Monte Carlo method gives roughly Gaussian-shaped distributions of dust masses and temperatures and the result from this analysis is in agreement with the best-fitting result.

G29.7–0.3: The thermal emission in this SNR can be fitted by a single temperature dust component with a best-fitting temperature of $T = 45.7$ K and dust mass of $M_\mathrm{d} = 0.03$ M$_\odot$ as seen in the top panel of Fig. 34. There is a large difference in the ISM flux level between the north and south of this remnant making it difficult to obtain an accurate value for the ISM level, as indicated by the large error bars in the SNR fluxes. At wavelengths longer than 70 μm, the error bars indicate that a dust mass cannot be determined as the source flux is at a similar level to that of the ISM. The median dust temperature from the Monte Carlo analysis is low compared to that of the best fit, resulting in a larger estimate for the dust mass. This discrepancy is caused by large uncertainty in the flux at long wavelengths, as indicated by the error bars in Fig. 34. A large fraction of the simulated fluxes at long wavelengths are much greater than the measured value, forcing the SED to peak at a longer wavelength. Therefore the Monte Carlo analysis is unable to give a constrained dust mass in these cases, although we clearly detect SN dust at a warmer temperature than the local ISM. This will be revisited in Section 4, where the dust temperature and mass will be analysed with a more rigorous routine.

4 ANALYSING THE DUST PROPERTIES WITH POINT PROCESS MAPPING (PPMAP)

Although SED fitting, as described in Section 3, can provide approximate dust mass and temperature estimates, as well as the synchrotron contribution, it is limited. We assume that the dust has a uniform temperature and a fixed emissivity index of 1.9. Next, we employ point process mapping (PPMAP) (Marsh, Whitworth & Lomax 2015; Marsh et al. 2017) in order to overcome these shortfalls

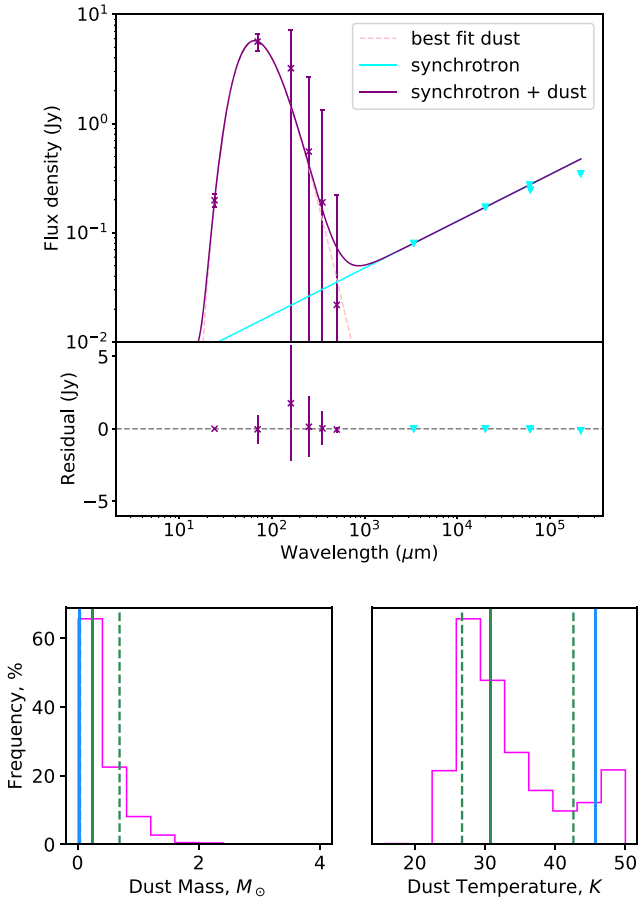

Figure 34. *Top*: Far-infrared SED of G29.7–0.3. *Bottom*: The distribution of source masses obtained by the Monte Carlo routine where SEDs were fit to 1000 normally distributed samples of flux values. The colour schemes are the same as for Fig. 32. The best-fitting and median values derived for dust temperature and mass are shown in Table 5.

and produce maps of differential column density across our objects at different temperatures and values of emissivity index. Using point spread function (PSF) information PPMAP is able to create column density maps without smoothing data to a common resolution. We can therefore use the highest resolution available to disentangle the dust emissivity index β and temperature components at any point, and to evaluate their variation across the source. We apply this technique to study G11.2–0.3, G21.5–0.9, and G29.7–0.3 using the 24–500 μm maps, and compare with the surrounding ISM for which we use only the *Herschel* maps due to potential issues with optical thickness, discussed in more detail later.

PPMAP operates in different dimensions to conventional (β, T) pixel-to-pixel fits, instead estimating a density distribution of mass throughout the 4D state space (x, y, T, β). The PPMAP procedure is described by Marsh et al. (2015). In this procedure, astrophysical systems such as SNRs are represented as a collection of primitive objects that each have unit column density. An object is characterized by its dust temperature ($T_{\rm D}$), emissivity index (β), and location on the 2D plane of the sky (x, y). Assuming that structures are optically thin, flux maps are considered as the total instrumental response to all objects. The distribution of column density is then defined by the number of objects appearing at any point in the 4D state space (x, y, T_D, β). PPMAP aims to find the optimal estimate for the distribution of objects by using a procedure based on Bayes' theorem. The expectation number of objects per unit volume in the 4D state space, $\rho(x, y, T_D, \beta)$, can be equated to the differential column density and is found through a stepwise approach. Initially, the measurement noise is artificially increased to the point at which no information can be obtained from the data. At this point the optimal solution is the a priori value of ρ. In the absence of further prior information, this function is flat everywhere. The noise is then decreased over a series of time-steps until the original signal-to-noise ratio is obtained; ρ is updated at each step, using the previous optimal solution as the new prior. The data at each stage can be described by a model of the form

$$\boldsymbol{d} = \mathbf{A}\boldsymbol{\Gamma}(\boldsymbol{t}) + \nu(t) \quad (5)$$

where $\boldsymbol{d}$ is the data vector at a given time step whose m-th component gives the pixel value at x_m, y_m for the wavelength λ_m; the vector $\boldsymbol{\Gamma}(\boldsymbol{t})$ describes the actual distribution of objects in state space; $\nu(t)$ gives the measurement noise at each time step, t, and is assumed to be Gaussian; and $\mathbf{A}$ is the system response matrix where the m-th element gives the m-th measurement response to an object in the n-th cell of state space i.e. (x_n, y_n, T_n, β_n). It is given by

$$A_{mn} = H_{\lambda_m}(X_m - x_n, Y_m - y_m)K_{\lambda_m}(T_n)B_{\lambda_m}(T_n)\kappa_{\lambda_m}(\beta_n)\Delta\Omega_m \quad (6)$$

where $H_{\lambda_m}(x, y)$ is the convolution of the PSF at λ_n with the profile of a source object; $K_{\lambda_m}(T_n)$ is a colour correction; $B_{\lambda_m}(T_n)$ is the Planck function; $\Delta\Omega_m$ is the solid angle subtended by the m-th pixel. By finding an optimal solution for $\mathbf{A}$, we can obtain the most likely distribution of β and $T_{\rm D}$ at each location in (x, y).

The PPMAP procedure is applied to estimate the column density over a grid of 12 temperature bins, centred at temperatures equally spaced in $\log(T_{\rm D})$, and up to seven values of β between 0 and 3 (Marsh et al. 2015). As the PWN dust has best-fitting modified blackbody temperatures of > 25 K, we initially use a temperature grid ranging from 25 to 75 K. If there is emission from components outside of this temperature range, PPMAP will return higher column density at the bounding temperatures. We therefore repeat the analysis extending our temperature range (20–90 K) to search for cooler and warmer components. For this study a Gaussian prior is assumed for distribution of material across β, with a mean of 1.9 (Planck Collaboration XXXI 2016) and standard deviation of 0.25. Providing PPMAP with prior information suppresses the temperature–β anticorrelation by excluding unrealistic results.

We estimate the cool dust mass of each SNR by summing the column density within the apertures described in Section 3 across the entire temperature and β grids. By averaging the temperature maps, PPMAP allows the amount of dust column density for each β value to be determined. After summing the differential column density over temperature, we obtain the density-weighted mean β along each line of sight.

4.1 Revised dust masses for our three PWNe

The column density map of dust emission at each of the temperature grid points from PPMAP is shown in Fig. 35 for the three SNRs, G11.2–0.3, G21.5–0.9, and G29.7–0.3. Prior to running the PPMAP analysis, an average ISM level is subtracted from the SNRs. This is estimated from annuli around the SNRs, as shown in Fig. 36, which are sigma-clipped to remove especially bright objects. The dust mass within each PWN is estimated by aperture photometry on the column density maps. This involves a second background subtraction, again using an average level from the annuli in Fig. 36, to ensure that there is minimal ISM contributing to our estimate. Fig. 37 shows the total SED for each remnant and the contribution

Table 5. The estimated mass ($M_\odot$) and temperature (K) of dust within each SNR derived from [a]a least squares SED fit to the data, [b]median results from a Monte Carlo routine as described in Section 3, [c]the PPMAP analysis as described in Section 4, where we do not assume a single dust temperature.

		Best fit[a]				Monte Carlo median[b]				PPMAP[c]
	Distance	Cold dust		Warm dust		Cold dust		Warm dust		Cold dust
SNR	(kpc)	T_d	M_d	T_d	M_d	T_d	M_d	T_d	M_d	M_d
G11.2–0.3	4.4[d]	27.3	0.9	180	7.9×10^{-6}	$26.7^{+1.7}_{-1.3}$	$1.1^{+0.4}_{-0.3}$	$92.4^{+87.6}_{-12.7}$	$(2.2^{+3.5}_{-2.1}) \times 10^{-4}$	0.34 ± 0.14
G21.5–0.9	4.7[e]	25.9	0.12	–	–	26.0 ± 0.7	0.12 ± 0.02	–	–	0.29 ± 0.08
G29.7–0.3	10.6[f]	45.7	0.03	–	–	$30.7^{+11.7}_{-4.0}$	$0.3^{+0.4}_{-0.2}$	–	–	0.51 ± 0.13

Note. Source distances are from [d]the near distance from HI absorption(Green 2004), [e]HI and CO observations (Camilo et al. 2006), and [f]the kinematic distance of an associated molecular cloud (Su et al. 2009).

from each temperature component, as estimated by PPMAP.

G11.2–0.3: In Fig. 35 we can see that the SNR is indistinguishable from the surrounding ISM at 25 K highlighting the difficulty in removing ISM emission where the temperatures are similar to dust in the ISM. Dust in the central region is brightest between 34 and 41 K and is not detected above 46 K. By contrast, there is evidence of two temperature components in the shell as we find that there is dust at 28–41 K and at 75 K. The tightly bound inner shell could indicate that the warmer shell dust may be reverse-shock heated, as seen in Cassiopeia A (Rho et al. 2008). However, it is thought that the reverse shock has already reached the centre of this remnant and expansion into an anisotropic CSM has caused the sharpness of the shell's inner edge (Borkowski et al. 2016) so it is unclear what is heating the shell dust. The dust structures are clearly seen when combining three of the temperature maps from Fig. 35 (31, 41, and 75 K) to produce a 'super-resolved' colour image in Fig. 36 (top panel). The dust emission from the PWN towards the centre is very clear in this image compared to the three-colour image derived using the native *Herschel* maps (Fig. 6) as the PPMAP results match the best available *Herschel* angular resolution i.e. 6.4 arcsec from the 70 μm images (Traficante et al. 2011).

The PPMAP generated SED for G11.2–0.3 in Fig. 37 shows how some of the temperature components revealed using PPMAP contribute to the total SED (here we show the full range investigated using PPMAP i.e. 20–90 K). We can see that the 20–23 K component contributes a significant amount of the total FIR flux measured in the apertures even after background subtracting the ISM. Since we have previously discussed that the PPMAP dust structures seen at temperatures of 20–25 K for this source are likely unrelated to the supernova, we therefore subtract these colder dust components from the final PPMAP derived dust mass. The dust mass is therefore derived by summing the column densities at the range of temperatures where SNR-related emission is seen, providing an estimated dust mass for the central ejecta region of G11.2–0.3 of $M_d = 0.34 \pm 0.14\,M_\odot$ (Table 5).[2]

This dust mass estimate is considerably smaller than the traditional modified blackbody fits in Section 3. This is due to the combination of differences between the two methods in the background subtraction and therefore the final FIR fluxes attributed to the SNR (this discrepancy is larger between 160 and 350 μm) and the fact that by inspecting the temperature components visually with PPMAP, we were able to conclude that dust at temperatures below 25 K was likely not SN-related, hence resulting in an additional subtraction from the final PPMAP dust mass. Indeed Section 3 suggests that the cool dust in G11.2 is at 26.7 K whereas PPMAP finds that part of this dust is at warmer temperatures, thus giving a smaller estimate for the total dust mass.

G21.5–0.9: As shown in Fig. 35, for this source we need to extend the temperature grid down to 20 K to show all the dust features, as there is a clear detection of PWN dust at temperatures of 20–25 K. The cold dust component is visible in the grid at temperatures from 20 to 27 K across the entire PWN region. Warmer dust between 30 and 37 K forms a shell-like structure close around the south-west of the central region in which the pulsar is located. The distribution of dust in this source is similar to that seen in G54.1+0.3; a bright peak of dust is evident to the north-west of the PWN shell that is significant and is robust to changes in mapping parameters. The PPMAP three-temperature map for G21.5–0.9 is shown in Fig. 36 (middle panel) where these features are clearly visible (with the coldest dust emission highlighted in red).

Using PPMAP, we retrieve a dust mass for G21.5–0.9 of $M_d = 0.29 \pm 0.08\,M_\odot$ (including all the emission from 20 to 90 K). This is ~2.5 times larger than both the best-fitting and median dust masses quoted in Section 3. Fig. 37 indicates that the fluxes used for the PPMAP analysis are greater than those used in Section 3. This is due to a combination of differences in the level of the background emission derived between PPMAP and Section 3 (this leads to a factor of 1.5–2 difference in the FIR fluxes attributed to the SNR) and PPMAP allowing for a wider range of temperatures in each pixel instead of putting all of the dust at a single temperature in the modified blackbody fits.

Thus G21.5–0.9 joins Cas A and G54.1 in the small list of Galactic SNRs for which dust at temperatures <25 K has been detected. PPMAP, with its better resolution and ability to map dust at different temperatures, has revealed significantly more dust in this source than from traditional modified blackbody fits.

G29.7–0.3: In Fig. 35, the PWN structure clearly contains dust at 28–31 K, although the surrounding medium is also at a similar temperature making the detection more confused than the other sources. There is warm (75 K) dust in the shell around the south-east of the SNR at the location of 24 and 70 μm emission observed in Fig. 15. This emission likely arises from shocked dust. Similar to G11.2–0.3, there is some evidence for warm dust in filaments within the shell, however this is much fainter and more confused in this case.

Similarly to G11.2–0.3, when inspecting the temperature grid of G29.7–0.3 between 20 and 90 K, we do not see evidence for any material related to the SNR structure at temperatures below 25 K. The PPMAP-derived SED shown in Fig. 37 shows that dust below these temperatures contributes significantly to the total FIR emission of this source, yet we have no evidence that this is associated with the SNR. Therefore we only use the temperature components revealed by PPMAP at 25 K and above when determining the dust mass for this source. For the central ejecta region in G29.7–0.3, PPMAP

[2]If we were to include the PPMAP dust components at temperatures below 25 K, the dust mass for G11.2–0.3 would be $M_d = 0.50 \pm 0.22\,M_\odot$.

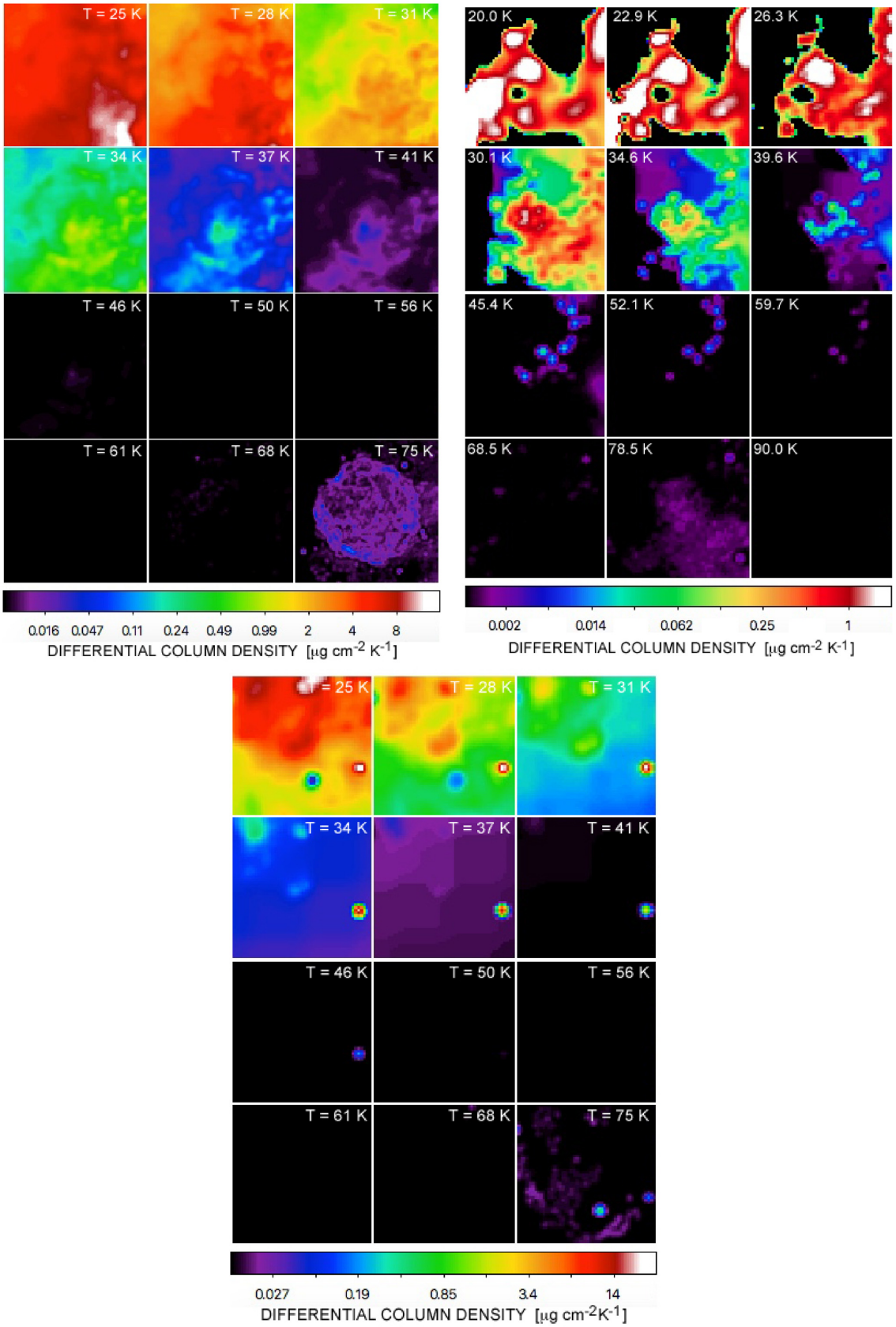

Figure 35. PPMAP-generated maps of differential dust column density split in different temperature ranges for *top-left:* G11.2–0.3, *top-right:* G21.5–0.9, and *bottom:* G29.7–0.3. The corresponding dust temperature is indicated in the top right of each panel. At temperatures less than 25 K in G11.2–0.3 and G29.7–0.3, the column density map begins to be dominated by unrelated interstellar dust along the line of sight and thus temperatures below 25 K for these sources are not used in the analysis.

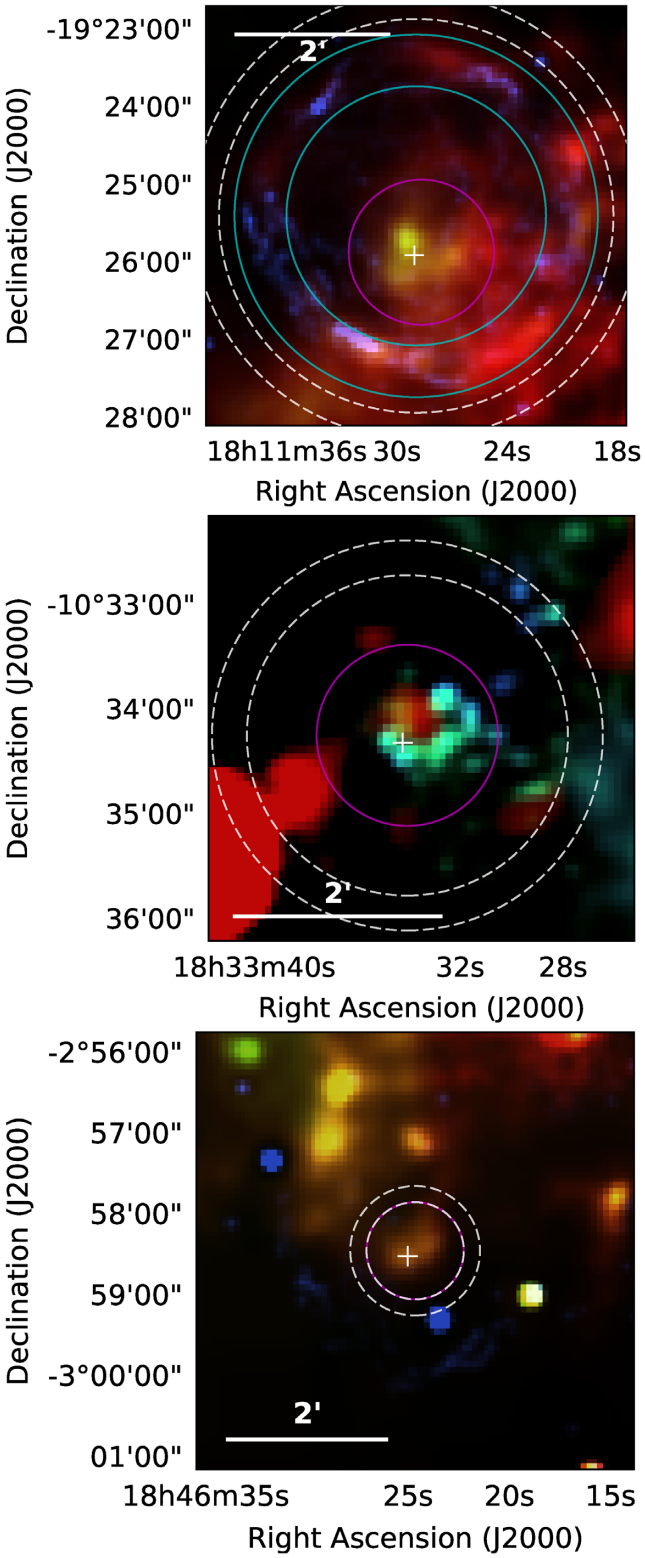

Figure 36. PPMAP-generated three-colour maps of differential dust column density created using dust temperature slices from Fig. 35. Colours show dust in G11.2–0.3 (*top*): 31 K (red), 41 K (green), and 75 K (blue). In G21.5–0.9 (*middle*): 20 K (red), 34.6 K (green), and 39.6 K (blue). In G29.7–0.3 (*bottom*): 28 K (red), 31 K (green), and 75 K (blue). The white crosses indicate the X-ray centres. The magenta circles show the apertures used for PWN dust, and the cyan and white circles were used to analyse shell and/or ISM emission, respectively.

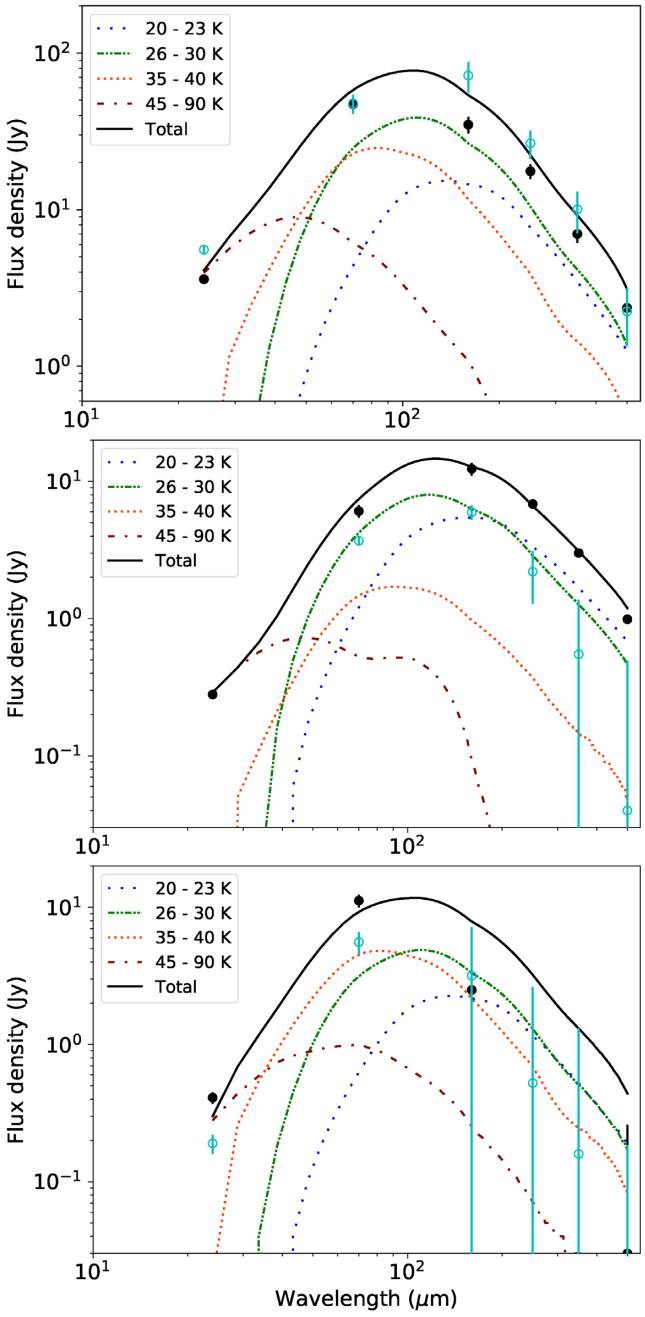

Figure 37. FIR SED as measured with PPMAP, analysing dust at temperatures between 20 K and 90 K, for the PWN in G11.2–0.3 (*top*), G21.5–0.9 (*middle*), and G29.7–0.3 (*bottom*). The open markers indicate the thermal flux estimated by aperture photometry in Section 3 and the filled markers indicate the estimated PPMAP flux in Section 4, where the difference is due to a variation in the estimate of the ISM level. Both sets of fluxes are background and synchrotron subtracted. There is a considerable contribution to the SEDs of both G11.2–0.3 and G29.7–0.3 from a cold dust (20–23 K) component. By visually inspecting the columns density maps for these sources, we find that dust at temperatures below 25 K is not related to the SNR. These cool dust components are therefore excluded when estimating the dust masses to avoid contamination from the ISM.

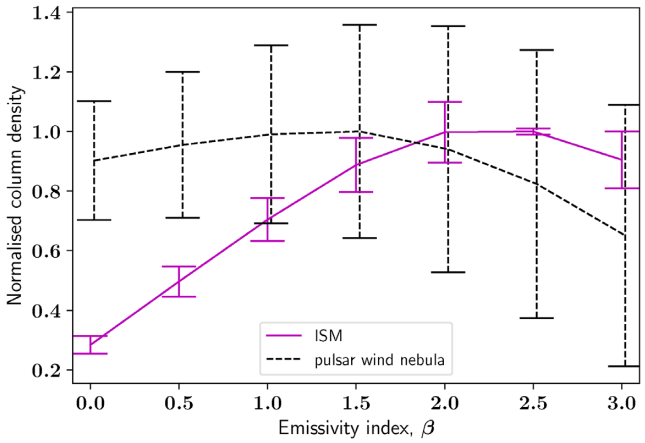

Figure 38. Estimated column density within each region at a given β for G21.5–0.9, measured from temperature averaged PPMAP images. The column density in each region is normalized by dividing by the peak column density of that region for easier comparison of the two curves. This is the resulting dust column density β profile assuming a flat β prior. (Fig. B1 shows the same profile from PPMAP assuming a Gaussian prior instead). The broad PWN profile reflects our inability to discriminate different values of β with low S/N.

therefore estimates a dust mass of $M_{\rm d} = 0.51 \pm 0.13\,{\rm M}_{\odot}$.[3] Again this is significantly larger than the best-fitting values derived in Section 3, although within the uncertainties it is consistent with the median from the Monte Carlo fits. This is not surprising since the single temperature best-fitting SEDs can be biased towards allocating a warmer dust temperature (∼46 K), whereas the Monte Carlo estimate allows for random selection of lower temperature components (∼30 K) and therefore higher dust masses than the best-fitting SED. The temperature grid from PPMAP in Fig. 35 shows emission from SN-related dust at lower temperatures than the best fit and therefore is more in agreement with the Monte Carlo estimate from Section 3.

4.2 Is the dust emissivity index different in SNe ejecta?

PPMAP allows us to evaluate β of the SNR and ISM dust as shown in Fig. 38. We estimate the density-weighted mean value of β within an aperture around the PWN and within in annuli encapsulating the surrounding medium and, for G11.2–0.3, the SNR shell (Fig. 36). We can therefore compare the emissivity index of material within the SNR components to that of the surrounding ISM using a β profile (Fig. 38). As the SNR β parameter is sensitive to the estimate of the ISM level, a lack of careful analysis can result in spurious variations in β. We therefore subtract the ISM from the source flux prior to analysis of the column density using the annuli shown in Fig. 36; this process is only applied to the SNRs, not to the ISM. This provides more robust results than subtracting the background of the resulting column density maps.

Additionally, the PPMAP analysis assumes that all media are optically thin, however, we find that the optical depth of the surrounding ISM in the 24 μm image is not negligible. We therefore disregard this band when evaluating β for the dust emission originating in the ISM, although this does not have a significant impact on any results for the cool dust components. The SNR material is likely optically thin and therefore the PPMAP analysis can be applied to this region using the 24 μm image.

We compare the dust column density in the PWN and surrounding (unrelated) interstellar dust found in each β 'bin' using the standard PPMAP assumption of a Gaussian prior with peak 1.9 and $\sigma = 0.25$. However, we find inconclusive results for β variations between the PWN and ISM in all three of our sources. These profiles are shown in Fig. B1 for completeness. Although the dust column density profiles with β appear to have a 'peak' column density for β of 1.8–2.0, we believe this is simply returning the prior distribution of β for the dust in the shell, ISM emission, and the PWN. To confirm this, we vary the prior to a lower mean, in which case PPMAP returns a correspondingly lower peak value of β. Thus, there is a systematic difference in the β of the ISM, shell, and PWN. However, the value of β depends on the prior.

Next we test how robust the PPMAP β analysis is given changes to the prior assumptions. Assuming a flat β prior instead of the Gaussian assumed earlier, we see no differences in the results for G11.2–0.3 and G29.7–0.3, but the column density-β profile for G21.5–0.9 does change (Fig. 38). The dust column density in the ISM now appears to peak at $\beta_{\rm ISM} \sim 2.5$ whereas the PWN peaks at lower values of $\beta_{\rm PWN} = 1.4 \pm 0.3$, though the error bars are large. The wide dispersion in β of the PWN is a result of the large uncertainties, reflecting our inability to discriminate different values of β at the low signal-to-noise ratio. As we do not apply a β prior in this case we are more susceptible to β-temperature anticorrelation, which is included in this uncertainty. Although there is a range of possible solutions, as indicated by the large uncertainty, there is some indication of a variation.

The density-weighted mean value of β along the line of sight for the ISM aperture is $\beta_{\rm ISM} = 1.8 \pm 0.1$ (this takes into account which values of β represents more of the mass), whereas for the PWN, this value is still consistent with the peak profile of $\beta = 1.4$.

Finally we re-ran PPMAP using a Gaussian prior with a mean of 1.4 (instead of 1.9). Again we found no differences in the results for SNRs G11.2–0.3 and G29.7–0.3. However, for G21.5–0.9, the new β profile is very similar to Fig. 38, but with a reduced χ-squared by ∼10 per cent, supporting the (marginal) result that the dust emissivity index in this PWN is smaller than the canonical ISM value.

4.3 Testing the reliability of our PPMAP results

In order to check whether the results from PPMAP have been affected by any assumptions, we test for potential biases due to overestimating the flux from hot dust, our chosen grids of dust temperatures and on the prior assumptions for β.

(i) The warmer dust components detected in the shells of G11.2–0.3 and G29.7–0.3 may artificially arise from contributions due to line emission at 24 μm. We therefore tested the PPMAP process for our SNRs after subtracting 30 per cent of the flux in the 24 μm band. This level was chosen as it is similar to the fraction of the Crab Nebula 24 μm flux expected to originate from line emission (Temim et al. 2012). We find this does not affect any of the dust mass or β results.

(ii) We next check if PPMAP is, in fact, able to extract values of β or is simply returning its prior value. We test this by simulating several 26 K Gaussian sources with a 1′ FWHM, varying β between

[3] If we were to include the PPMAP dust components at temperatures below 25 K, the dust mass for G29.7–0.3 would be $M_{\rm d} = 0.64 \pm 0.18\,{\rm M}_{\odot}$. In this case we expect that the estimate suffers from contamination by unrelated ISM and is superficially large.

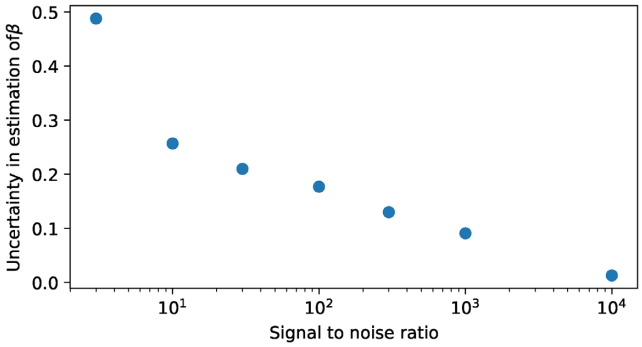

Figure 39. The root-mean-square uncertainty of the β value derived by PPMAP based on simulations for a 26 K source with Gaussian noise applied.

1.5 and 2.4. The images are convolved to the *Herschel* beam sizes and add Gaussian noise for a signal-to-noise ratio between 3 and 10 000, which is constant across the spectrum. Assuming a flat β prior between 0 and 3, we then use PPMAP to estimate β for each simulated source in order to verify if PPMAP can return the correct value from the simulations. We find that the ability of PPMAP to pull out precise values of β is critically dependent on the signal-to-noise ratio of the FIR data. At high signal-to-noise ratios ($\sim$100), we find that the returned β matches the original value with an error less than 0.15. Fig. 39 shows how the uncertainty in the PPMAP estimated values of β varies with the signal-to-noise ratio of the input simulations. The lowest signal-to-noise ratio in this test ($\sim$3) is typical of our most resolved PWN source, G21.5–0.9. The other two SNRs have larger FIR uncertainties (due to the high background levels) and therefore this confirms that we would not be able to derive the value of β in G11.2–0.3 and G29.7–0.3 with any precision. For G21.5–0.9, this suite of simulations therefore suggests that our uncertainty in the β value derived in Section 4.2 is slightly larger, i.e. $\beta_{\rm PWN} = 1.4 \pm 0.5$.

In our images the signal-to-noise ratio is not constant across the spectrum as we have much more confusion at longer wavelengths. In order to constrain β, our tests show that higher signal-to-noise ratio at the Rayleigh-Jeans end of the spectrum is required. This is difficult given the current large uncertainties and variation in the ISM flux for most Galactic SNRs observed with *Herschel*. With higher resolution or longer wavelength data, we could constrain β to within a smaller uncertainty range and potentially draw out any differences in the dust properties between different SNR regions. It may be easier to constrain β for SNRs in the regions of the Galactic plane at $|l| > 60^\circ$ which, on average, suffer from lower levels of background interstellar dust emission.

5 CONCLUSIONS

We follow R06 and PG11 and classify the FIR structures in Galactic SNRs in levels 1–4, where 1 = detection (FIR emission that is clearly correlated with radio, MIR, or X-ray structures and can be distinguished from ISM) and level 4 is not detected in the FIR. We add 27 new SNRs to the current sample of 3 in our Galaxy that contain cool dust (<50 K) associated with the SNR. This is a lower limit to the number of dusty SNRs in our sample as we suffer from a number of biases.

Dust is detected from the central region of eight sources, one of which was recently discussed elsewhere (Temim et al. 2017; Rho et al. 2018) and three of which (G11.2–0.3, G21.5–0.9, and G29.7–0.3) are *new detections of FIR emission coinciding with the locations of PWNe.* We analyse the dust content of these three PWNe by fitting their SED to NIR-radio data using modified blackbody fits. The best fits from this analysis give estimated cold dust temperatures for G11.2–0.3, G21.5–0.9, and G29.7–0.3, respectively, of 27.3 K, 25.9 K, and 45.7 K, and dust masses of 0.9 $M_\odot$, 0.12 $M_\odot$, and 0.03 $M_\odot$. We also carry out a Monte Carlo analysis, randomly sampling a set of 1000 flux values at each wavelength with a Gaussian distribution centred at the measured flux. This provides 1000 sets of results for each SNR, with median dust temperatures for G11.2–0.3, G21.5–0.9, and G29.7–0.3, respectively, of $26.7^{+1.7}_{-1.3}$ K, 26.0 ± 0.7 K, and $30.7^{+11.7}_{-4.0}$ K, and dust masses of $1.1^{+0.4}_{-0.3}$ $M_\odot$, 0.12 ± 0.02 $M_\odot$, and $0.3^{+0.4}_{-0.2}$ $M_\odot$. Large uncertainties in our fluxes at the longest FIR wavelengths for G29.7–0.3 pull the median estimate to a lower dust temperature and larger dust mass than that of the best fit.

We use PPMAP to more rigorously analyse the material within the three SNRs. This confirms the presence of cold dust (20–40 K) within the PWN regions, which is clearly distinguishable from the surrounding ISM, and warm dust in the shells of G11.2–0.3 and G29.7–0.3. Through this analysis we estimate significant cold dust masses within the PWNe of 0.34 ± 0.14 $M_\odot$, 0.29 ± 0.08 $M_\odot$, 0.51 ± 0.13 $M_\odot$, for G11.2–0.3, G21.5–0.9, and G29.7–0.3 respectively. For both G11.2–0.3 and G29.7–0.3 these estimates are much more constrained than those of the traditional SED-fitting routine. PPMAP allows for a range of dust temperatures across the SNRs making these results more reliable.

Using PPMAP, we also analyse the variation in the dust emissivity index, β, across the SNRs and compare with the values derived for the SN shell and ISM regions. We are unable to constrain β within G11.2–0.3 and G29.7–0.3 due to the low signal-to-noise at long wavelengths. For G21.5–0.9, we estimate $\beta_{\rm PWN} = 1.4 \pm 0.5$ in the PWN (with uncertainty in β derived from simulated data sets), and find $\beta_{\rm ISM} = 1.8 \pm 0.1$ in the ISM dust based on using a flat β prior. We show that with higher signal-to-noise in the FIR (or indeed longer wavelength data), our simulations suggest that in future, we could further constrain β within the PWNe and potentially draw out any differences in the dust properties with respect to dust in the interstellar medium. This may be easier for Galactic plane SNRs at $|l| > 60^\circ$ where there are lower levels of background interstellar dust emission on average.

ACKNOWLEDGEMENTS

We thank the anonymous referee for their thorough and careful reading of this paper and many constructive suggestions. We acknowledge Nicolas Peretto for help with CO data at the locations of some of our sources. HC, HLG, and PC acknowledge support from the European Research Council (ERC) in the form of Consolidator Grant COSMICDUST (ERC-2014-CoG-647939). MJB and IDL acknowledge support from the ERC in the form of Advanced Grant SNDUST (ERC-2015-AdG-694520). MM acknowledges support from an STFC Ernest Rutherford fellowship (ST/L003597/1). *Herschel* is an ESA space observatory with science instruments provided by European-led Principal Investigator consortia and with important participation from NASA.

REFERENCES

Andersen M., Rho J., Reach W. T., Hewitt J. W., Bernard J. P., 2011, ApJ, 742, 7
Anderson L. D., et al., 2017, A&A, 605, A58
Arendt R. G., 1989, ApJ, 70, 181

Arendt R. G., Dwek E., Moseley S. H., 1999, ApJ, 521, 234
Arendt R. G. et al., 2011, ApJ, 734, 54
Balog Z. et al., 2014, Exp. Astron, 37, 129
Barlow M. J. et al., 2010, A&A, 518, L138
Becker R. H., Helfand D. J., 1984, ApJ, 283, 154
Bendo G. J. et al., 2013, MNRAS, 433, 3062
Bietenholz M. F., Bartel N., 2008, MNRAS, 386, 1411
Bietenholz M. F., Matheson H., Safi-Harb S., Brogan C., Bartel N., 2011, MNRAS, 412, 1221
Biscaro C., Cherchneff I., 2016, A&A, 132, 1
Bocchino F., van der Swaluw E., Chevalier R., Bandiera R., 2005, A&A, 442, 539
Bocchino F., Bandiera R., Gelfand J., 2010, A&A, 71, 1
Bocchio M., Jones A. P., Slavin J. D., 2014, A&A, 570, A32
Bock D. C. J., Gaensler B. M., 2005, ApJ, 626, 343
Borkowski K. J., Reynolds S. P., Roberts M. S. E., 2016, ApJ, 819, 160
Braun R., Gull S. F., Perley R. A., 1987, Nature, 327, 395
Brogan C. L., Devine K. E., Lazio T. J., Kassim N. E., Tam C., Brisken W. F., Dyer K. K., Roberts M. S. E., 2004, ApJ, 127, 355
Brogan C. L., Gelfand J. D., Gaensler B. M., Kassim N. E., Lazio T. J., 2006, ApJ, 639, 5
Camilo F., Lorimer D. R., Bhat N. D. R., Gotthelf E. V., Halpern J. P., Wang Q. D., Lu F. J., Mirabal N., 2002, ApJ, 574, 5
Camilo F., Ransom S. M., Gaensler B. M., Slane P. O., Lorimer D. R., Reynolds J., Manchester R. N., Murray S. S., 2006, ApJ, 637, 11
Carey S. J. et al., 2009, PASP, 121, 76
Carter L. M., Dickel J. R., Bomans D. J., 1997, PASP, 109, 990
Caswell J. L., Haynes R. F., Milne D. K., Wellington K. J., 1983, MNRAS, 203, 595
Chen Y., Su Y., Slane P. O., Wang Q. D., 2004, ApJ, 616, 27
Chevalier R. A., 2005, ApJ, 619, 839
Clark C. J., Schofield S. P., Gomez H. L., Davies J. I., 2016, MNRAS, 459, 1646
Combi J. A. et al., 2010a, A&A, 522, A50
Combi J. A. et al., 2010b, A&A, 523, A76
Cruciani A. et al., 2016, MNRAS, 459, 4224
Davidson K., Fesen R. A., 1985, ARA&A, 23, 119
De Looze I. et al., 2017, MNRAS, 465, 3309
Dempsey J. T., Thomas H. S., Currie M. J., 2013, ApJ SS, 209, 8
Douvion T., Lagage P. O., Pantin E., 2001, A&A, 369, 589
Draine B. T., 1981, ApJ, 245, 880
Dubner G., Giacani E., Reynoso E., 1999, AJ, 118, 930
Dubner G. M., Giacani E. B., Goss W. M., Moffett D. A., Holdaway M., 1996, ApJ, 111, 1304
Dunne L., Eales S., Edmunds M., Ivison R., Alexander P., Clements D. L., 2000, MNRAS, 315, 115
Dunne L., Eales S., Ivison R., Morgan H., Edmunds M., 2003, Nature, 424, 285
Dunne L. et al., 2009, MNRAS, 394, 1307
Dwek E., 1987, ApJ, 322, 812
Dwek E., 1998, ApJ, 501, 643
Dwek E., Arendt R. G., 2015, ApJ, 810, 75
Dwek E., Galliano F., Jones A. P., 2007, ApJ, 662, 927
Engelbracht C. W. et al., 2007, PASP, 119, 994
Frail D. a., Goss W. M., Whiteoak J. B. Z., 1994, AJ, 437, 23
Frail D. A., Reynoso E., Giacani E., Green A., Otrupcek R., 1996, AJ, 111, 1651
Frank K. A., Burrows D. N., Park S., 2015, AJ, 810, 113
Gaensler B. M., Manchester R. N., Green A. J., 1998, MNRAS, 296, 813
Gaensler B. M., Gotthelf E. V., Vasisht G., 1999, ApJ, 526, L37
Gall C., Hjorth J., Andersen A. C., 2011, A&A Rev., 19
Ghavamian P., Williams B. J., 2016, ApJ, 831, 188
Giacani E., Smith M. J. S., Dubner G., Loiseau N., 2011, A&A, 531, A138
Giacani E. B., Dubner G. M., Kassim N. E., Frail D. a., Goss W. M., Winkler P. F., Williams B. F., 1997, AJ, 113, 1379
Gomez H. L. et al., 2012a, MNRAS, 420, 3557
Gomez H. L. et al., 2012b, ApJ, 760, 96
Goss W. M., Shaver P. A., Skellern D. J., Watkinson A., 1979, A&A, 78, 75
Green D. A., 2004, BASI, 32, 335
Green D. A., 2009, MNRAS, 399, 177
Green D. A., 2014, BASI, 42, 47
Green D. A., Dewdney P. E., 1992, MNRAS, 254, 686
Griffin M. et al., 2010, A&A, 518, L3
Halpern J. P., Gotthelf E. V., 2010, ApJ, 710, 941
Harrus I. M., Slane P. O., 1999, ApJ, 516, 811
Helfand D. J., Collins B. F., Gotthelf E. V., 2003a, ApJ, 582, 783
Helfand D. J., Agueros M. A., Gotthelf E. V., 2003b, ApJ, 592, 941
Helfand D. J., Becker R. H., White R. L., Fallon A., Tuttle S., 2006, AJ, 131, 2525
Hwang U., Petre R., Hughes J. P., 2000, ApJ, 532, 970
Indebetouw R. et al., 2014, ApJ Lett., 782, L2
Jackson J. M. et al., 2006, ApJ SS, 163, 145
James A., Dunne L., Eales S., Edmunds M. G., 2002, MNRAS, 335, 753
Jones A. P., Tielens A. G. G. M., Hollenbach D. J., McKee C. F., 1997, AIP Conf. Proc., 402, 19
Jones L. R., Smith A., Angelini L., 1993, MNRAS, 265, 631
Junkes N., Furst E., Reich W., 1992, A&A, 261, 289
Kaspi V. M., Roberts M. E., Vasisht G., Gotthelf E. V., Pivovaroff M., Kawai N., 2001, ApJ, 560, 371
Kassim N. E., Weiler K. W., Baum S. A., 1991, ApJ, 374, 212
Keohane J. W., Reach W. T., Rho J., Jarrett T. H., 2007, ApJ, 654, 938
Kilpatrick C. D., Bieging J. H., Rieke G. H., 2016, ApJ, 816, 1
Klochkov D., Suleimanov V., Sasaki M., Santangelo A., 2016, A&A, 12, 8
Koo B.-c., Moon D., Lee H., Lee J.-j., Matthews K., 2007, ApJ, 657, 308
Koo B.-C. et al., 2008, ApJ, 673, 225
Kothes R., Dougherty S. M., 2007, A&A, 1000, 993
Kothes R., Reich W., 2001, A&A, 372, 627
Kozasa T., Nozawa T., Tominaga N., Umeda H., Maeda K., Nomoto K., 2009, in Henning T., Grun E., Steinacker J., eds, Cosmic Dust - Near and Far ASP Conference Series, Vol. 414. Heidelberg, Germany
Kumar H. S., Safi-Harb S., Slane P. O., Gotthelf E. V., 2014, ApJ, 781, 41
Lau R. M., Herter T. L., Morris M. R., Li Z., Adams J. D., 2015, Science, 348, 413
Leahy D., Green K., Tian W., 2014, MNRAS, 438, 1813
Leahy D. A., Ranasinghe S., 2016, ApJ, 817, 74
Leahy D. A., Tian W. W., 2008, A&A, 480, L25
Leahy D. A., Tian W., Wang Q. D., 2008, ApJ, 136, 1477
Lopez L. A., Ramirez-Ruiz E., Castro D., Pearson S., 2013, ApJ, 764, 50
Macalpine G. M., Satterfield T. J., 2008, ApJ, 136, 2152
Mancini M., Schneider R., Graziani L., Valiante R., Dayal P., Maio U., Ciardi B., Hunt L. K., 2015, MNRAS, 451, L70
Marsh K. A., Whitworth A. P., Lomax O., 2015, MNRAS, 454, 4282
Marsh K. A. et al., 2017, MNRAS, 471, 2730
Matsuura M. et al., 2009, MNRAS, 396, 918
Matsuura M. et al., 2011, Science, 333, 1258
Matsuura M. et al., 2015, ApJ, 800, 50
Matthews B., Wallace B., Taylor A., 1998, ApJ, 20, 312
Micelotta E. R., Dwek E., Slavin J. D., 2016, A&A, 590, A65
Michałowski M. J., 2015, A&A, 80, 1
Michałowski M. J., Murphy E. J., Hjorth J., Watson D., Gall C., Dunlop J. S., 2010, A&A, 522, A15
Misanovic Z., Kargaltsev O., Pavlov G. G., 2010, ApJ, 725, 931
Moffett D. A., Reynolds S. P., 1994, ApJ, 437, 705
Molinari S. et al., 2010, PASP, 122, 314
Molinari S. et al., 2013, A&A, 518, L100
Moon D.-S., Koo B.-C., Lee H.-G., Matthews K., Lee J.-J., Pyo T.-S., Seok J. Y., Hayashi M., 2009, ApJ, 703, L81
Morgan H. L., Edmunds M. G., 2003, MNRAS, 343, 427
Morsi H. W., Reich W., 1987, A&A SS, 69, 533
Morton T. D., Slane P., Borkowski K. J., Reynolds S. P., Helfand D. J., Gaensler B. M., Hughes J. P., 2007, AJ, 667, 219
Nozawa T., Kozasa T., Umeda H., Maeda K., Nomoto K., 2003, ApJ, 598, 785
Nozawa T., Kozasa T., Habe A., Dwek E., Umeda H., Tominaga N., Maeda K., Nomoto K., 2007, ApJ, 666, 955

Nozawa T., Kozasa T., Tominaga N., Maeda K., Umeda H., Nomoto K., Krause O., 2010, ApJ, 713, 356
Nugent J. J., Pravdo S. H., Garmire G. P., Becker R. H., Tuohy I. R., Winkler P. F., 1984, ApJ, 284, 612
Oliva E., Moorwood A. F. M., Danziger I. J., 1990, A&A, 240, 453
Oliva E., Moorwood A. F. M., Drapatz S., Lutz D., Sturm E., 1999, A&A, 343, 943
Ostriker J., Silk J., 1973, ApJ, 184, L113
Owen P. J., Barlow M. J., 2015, ApJ, 801, 141
Pannuti T. G., Rho J., Heinke C. O., Moffitt W. P., 2014, AJ, 147, 55
Park G. et al., 2013, ApJ, 777, 14
Paron S., Giacani E., Rubio M., Dubner G., 2011, A&A, 530, A25
Patnaik A., Hunt G., Salter C., Shaver P., Velusamy T., 1990, A&A, 232, 467
Petriella A., Paron S. A., Giacani E. B., 2013, A&A, 554, A73
Pilbratt G. L. et al., 2010, A&A, 518, L1
Pinheiro Goncalves D. et al., 2011, AJ, 142, 42
Planck Collaboration XIV, 2014, A&A, 564, A45
Planck Collaboration XXXI, 2016, A&A, 586, A134
Planck Collaboration XXIX, 2016, A&A, 586, A132
Poglitsch A. et al., 2010, A&A, 518, L2
Pye J. P., Becker R. H., Seward F. D., Thomas N., 1984, MNRAS, 207, 649
Rakowski C. E., Badenes C., Gaensler B. M., Gelfand J. D., Hughes J. P., Slane P. O., 2006, ApJ, 646, 982
Rea N., Borghese A., Esposito P., Zelati F. C., Bachetti M., Israel G. L., Luca A. D., 2016, ApJ Lett., 828, L13
Reach W. T., Rho J., Jarrett T. H., 2005, ApJ, 618, 297
Reach W. T. et al., 2006, AJ, 131, 1479
Reich W., Furst E., Sofue Y., 1984, A&A, 133, L4
Reynolds S. P., 2006, ApJ, 652, L45
Reynoso E. M., Mangum J. G., 2000, ApJ, 20, 874
Reynoso E. M., Green A. J., Johnston S., Giacani E. B., Goss W. M., 2006, PASA, 21, 82
Rho J., Petre R., Schlegel E. M., Hester J. J., 1994, ApJ, 430, 757
Rho J. et al., 2008, ApJ, 673, 271
Rho J. et al., 2018, MNRAS, 479, 5101
Rowlands K., Gomez H. L., Dunne L., Aragón-Salamanca A., Dye S., Maddox S., da Cunha E., van der Werf P., 2014, MNRAS, 441, 1040
Saken J. M., Fesen R. A., MIchael S. J., 1992, ApJ SS, 81, 715
Salter C. J., Emerson D. T., Steppe H., Thum C., 1989a, A&A, 225, 167
Salter C. J. et al., 1989b, ApJ, 338, 171
Sato T., Koyama K., Lee S. H., Takahashi T., 2016, PASJ, 68, S81
Sezer A., Gök F., Hudaverdi M., Ercan E. N., 2011, MNRAS, 417, 1387
Simpson R. J. et al., 2012, MNRAS, 424, 2442
Slane P., Chen Y., Lazendic J. S., Hughes J. P., 2002, ApJ, 580, 904
Smith A., Jones L. R., Peacock A., Pye J. P., 1985, ApJ, 296, 469
Stupar M., Parker Q. A., 2011, MNRAS, 414, 2282
Su Y., Chen Y., Yang J., Koo B.-c., Zhou X., Jeong I.-g., Zhang C.-g., 2009, ApJ, 694, 376
Sugizaki M., Mitsuda K., Kaneda H., Matszaki K., Yamauchi S., Koyama K., 2001, ApJ SS, 134, 77
Takata A., Nobukawa M., Uchida H., Tsuru T. G., Tanaka T., Koyama K., 2016, PASJ, 68, S31
Tam C., Roberts M. S. E., 2003, ApJ, 598, L27
Taylor J. H., Manchester R. N., Lyne A. G., 1993, ApJ SS, 88, 529
Taylor A. R. et al., 2003, AJ, 125, 3145
Temim T., Slane P., Reynolds S. P., Raymond J. C., Borkowski K. J., 2010, ApJ, 710, 309
Temim T., Sonneborn G., Dwek E., Arendt R. G., Gehrz R. D., Slane P., Roellig T. L., 2012, ApJ, 753, 72
Temim T., Dwek E., Tchernyshyov K., Boyer M. L., Meixner M., Gall C., Roman-Duval J., 2015, ApJ, 799, 158
Temim T., Dwek E., Arendt R. G., Borkowski K. J., Reynolds S. P., Slane P., Gelfand J. D., Raymond J. C., 2017, ApJ, 836, 129
Tian W. W., Leahy D. A., 2008, MNRAS, 58, 54
Tian W. W., Leahy D. A., 2012, MNRAS, 421, 2593
Tian W. W., Leahy D. A., 2014, ApJ, 783, L2
Todini P., Ferrara A., 2001, MNRAS, 325, 726
Torii K., Tsunemi H., Dotani T., Mitsuda K., 1997, AJ, 489, L145
Traficante A. et al., 2011, MNRAS, 416, 2932
Tsuji N., Uchiyama Y., 2016, PASJ, 68, 108
Tuohy I. R., Garmire G. P., 1980, ApJ, 239, L107
Vasisht G., Aoki T., Dotani T., Kulkarni S. R., Nagase F., 1996, ApJ, 456, L59
Vasisht G., Gotthelf E. V., Torii K., Gaensler B. M., 2000, ApJ, 542, L49
Veneziani M. et al., 2013, A&A, 549, A130
Vink J., 2004, ApJ, 604, 7
Voisin F., Rowell G., Burton M. G., Walsh A., Fukui Y., Aharonian F., 2016, MNRAS, 458, 2813
Whiteoak J. B., Green A. J., 1996, A&A SS, 118, 329
Wolszczan A., Cordes J. M., Dewey R. J., 1991, ApJ, 372, L99
Yamaguchi H., Tanaka M., Maeda K., Slane P. O., Foster A., Smith R. K., Katsuda S., Yoshii R., 2012, ApJ, 749, 137
Yamaguchi H. et al., 2015, ApJ, 801, L31
Yamauchi S., Ueno M., Koyama K., Bamba A., 2005, PASJ, 57, 459
Yamauchi S., Minami S., Ota N., Koyama K., 2014a, ASJ, 66, 1
Yamauchi S., Bamba A., Koyama K., 2014b, PASJ, 66, 20
Yusef-Zadeh F., Wardle M., Rho J., Sakano M., 2003, ApJ, 585, 319
Zhou P., Chen Y., 2011, ApJ, 743, 4
Zhou P., Chen Y., Safi-Harb S., Zhou X., Sun M., Zhang Z.-Y., Zhang G.-y., 2016, ApJ, 831
Zhu H., Tian W. W., Torres D. F., Pedaletti G., Su H. Q., 2013, ApJ, 775, 95

APPENDIX A: FIR CATALOGUE OF SNRS WITH *HERSCHEL*

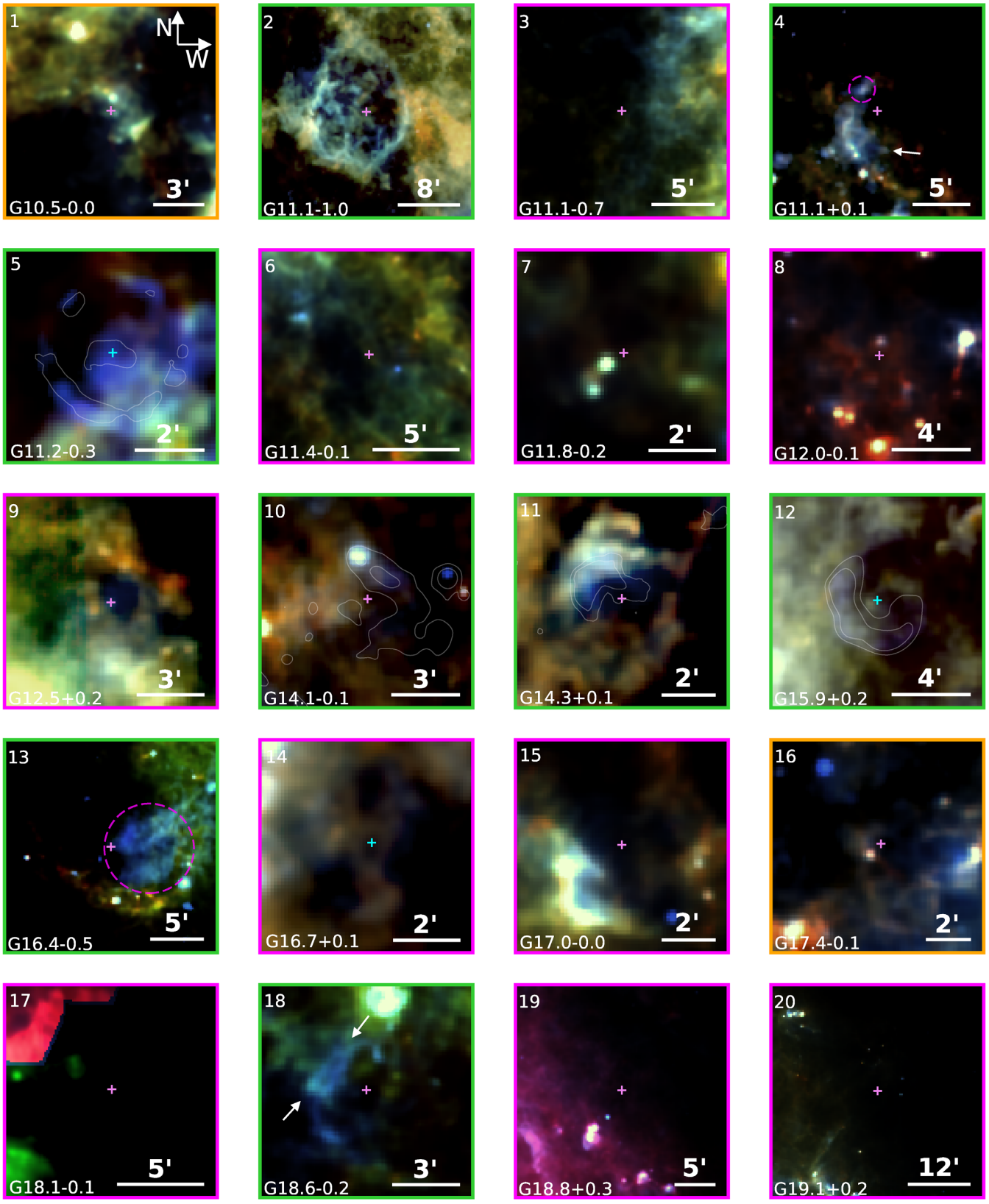

Figure A1. *Herschel* three-colour images of the locations of all SNRs in our sample. Colours are red = 250 μm, green = 160 μm, and blue = 70 μm. Purple crosses indicate the source radio centre from Green (2014) and cyan crosses indicate the X-ray centre. Magenta diamonds indicate the location of 1720 MHz OH masers. The border colour indicates the associated detection level in this study, as given in Table 1, where green = level 1, orange = level 2, magenta = level 3, grey = level 4, and black = unstudied. In some panels, dashed magenta circles and white arrows indicate particular FIR dust emission features associated with the SNR. X-ray contours are overlaid onto the images of G11.2–0.3 and G15.9+0.2, MIPS contours are overlaid onto G14.1–0.1, and radio contours are overlaid onto the image of G14.3+0.1.

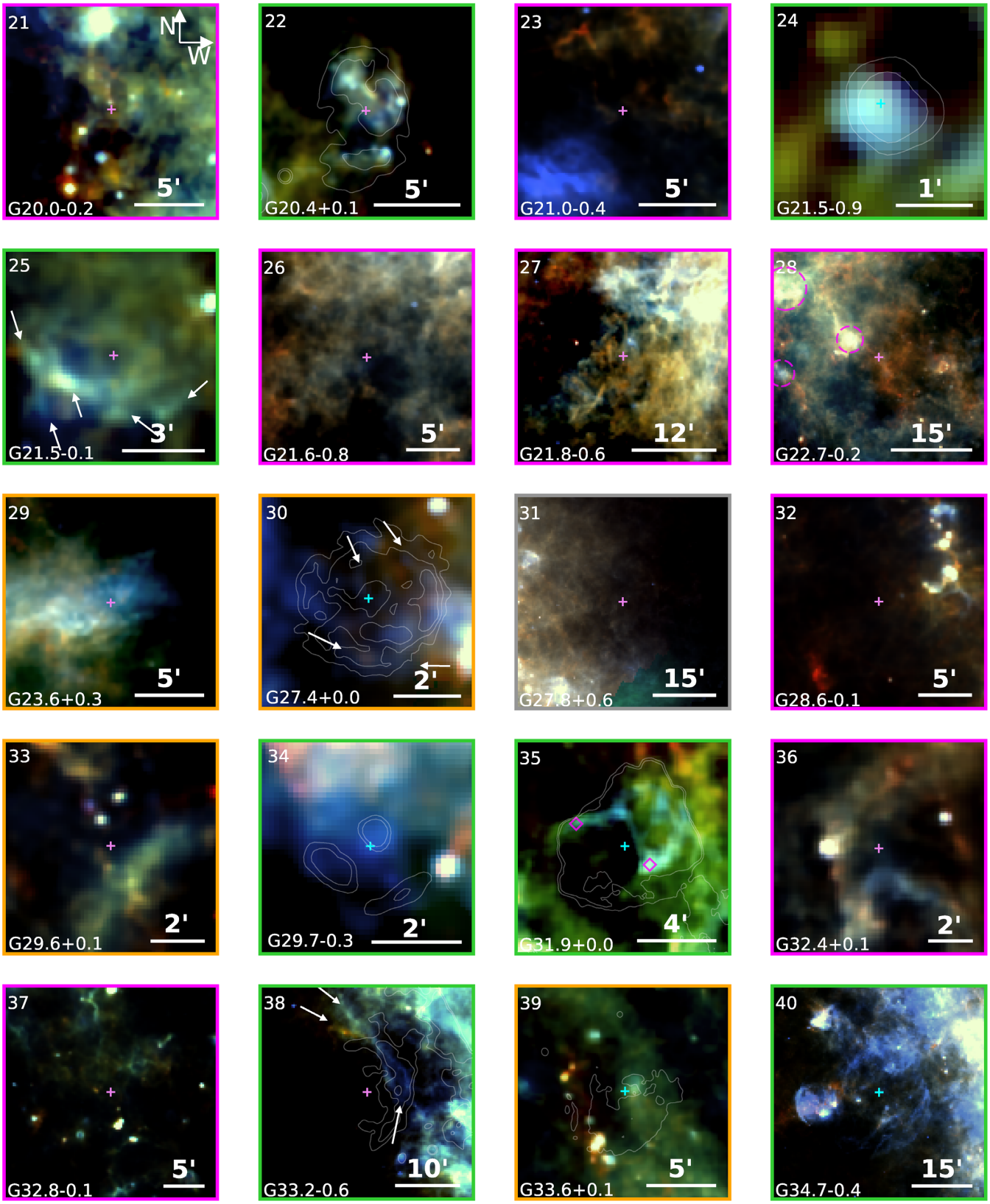

Figure A1. – *Continued.* Radio 20cm contours are overlaid onto the image of G20.4+0.1, G31.9+0.0, and G33.2-0.6. X-ray contours are overlaid onto the imags of G21.5-0.9, G27.4+0.0, G29.7-0.3, and G33.6+0.1.

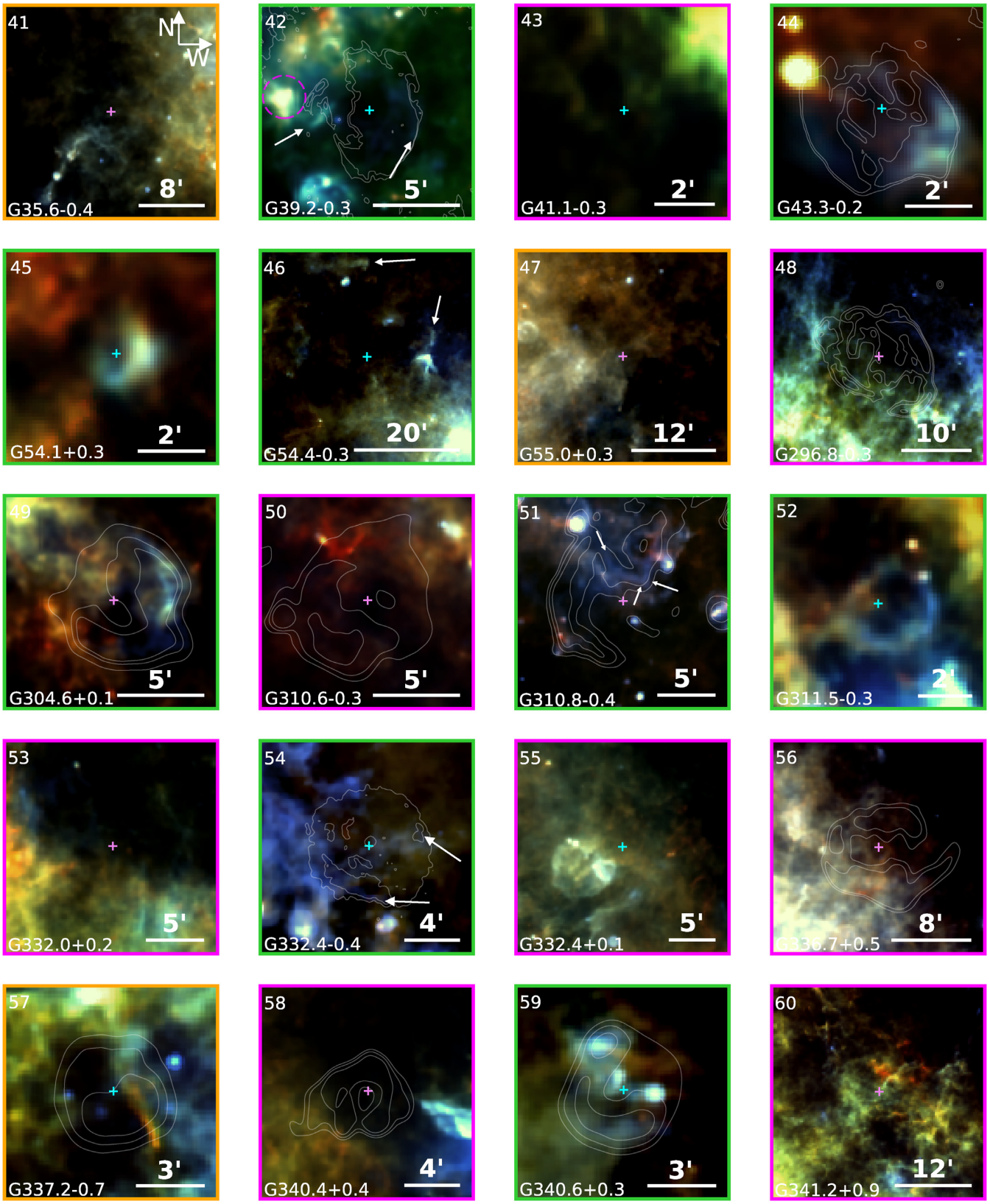

Figure A1. *Continued*. Radio contours are overlaid on to the images of G39.2-0.3, G43.3-0.2, G296.8-0.3, G304.6+0.1, G310.6-0.3, G310.8-0.4, G336.7+0.5, G337.2-0.7, G340.4+0.4, and G340.6+0.3. X-ray contours are overlaid onto the image of G332.4-0.4

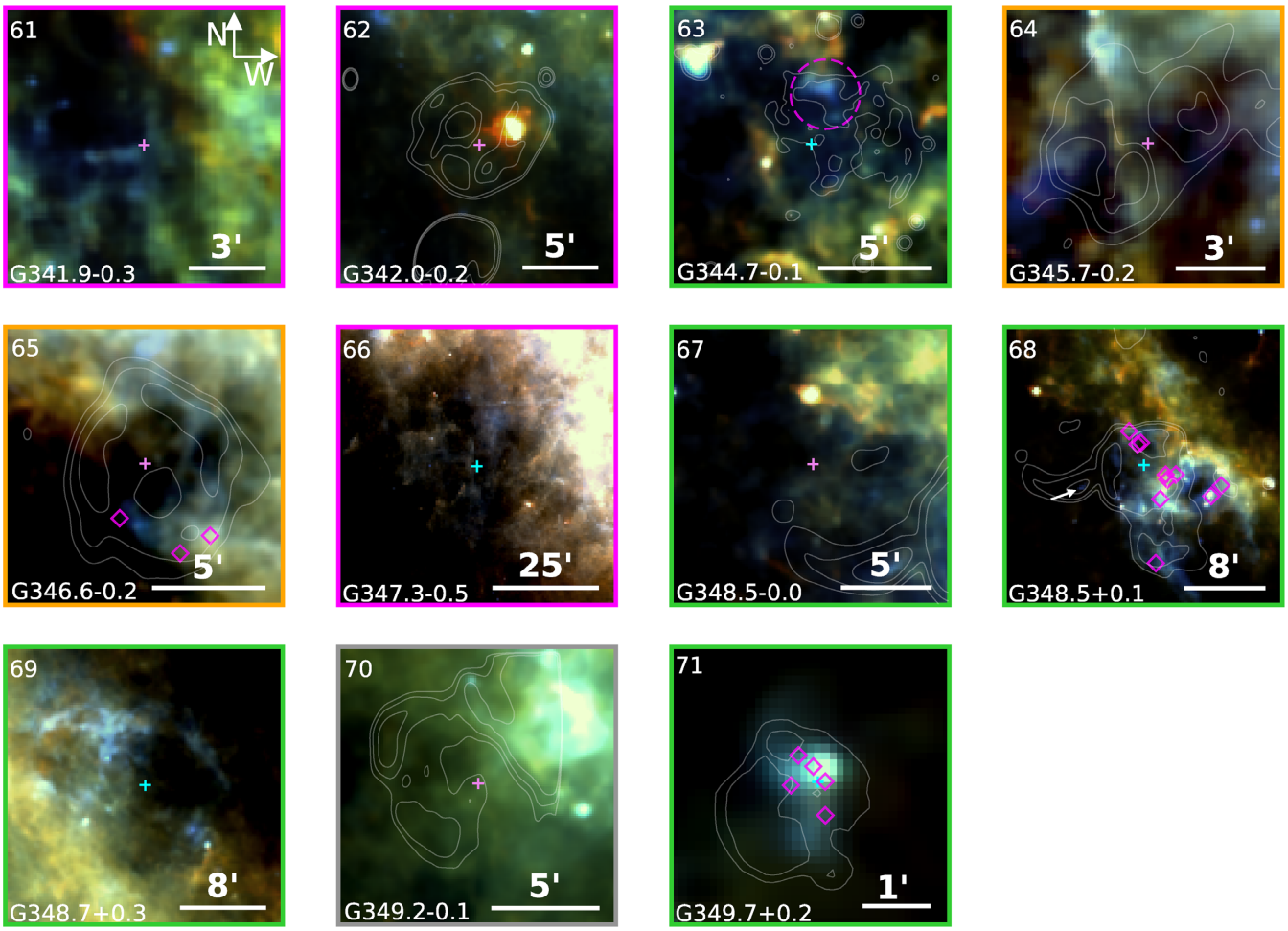

Figure A1. – *Continued*. MIPS contours are overaid onto the image of G344.7-0.1, X-ray contours onto the image of G349.7+0.2, and radio contours onto the images of G342.0-0.2, G345.7-0.2, G346.6-0.2, G348.5-0.0, G348.5+0.1, and G349.2-0.1.

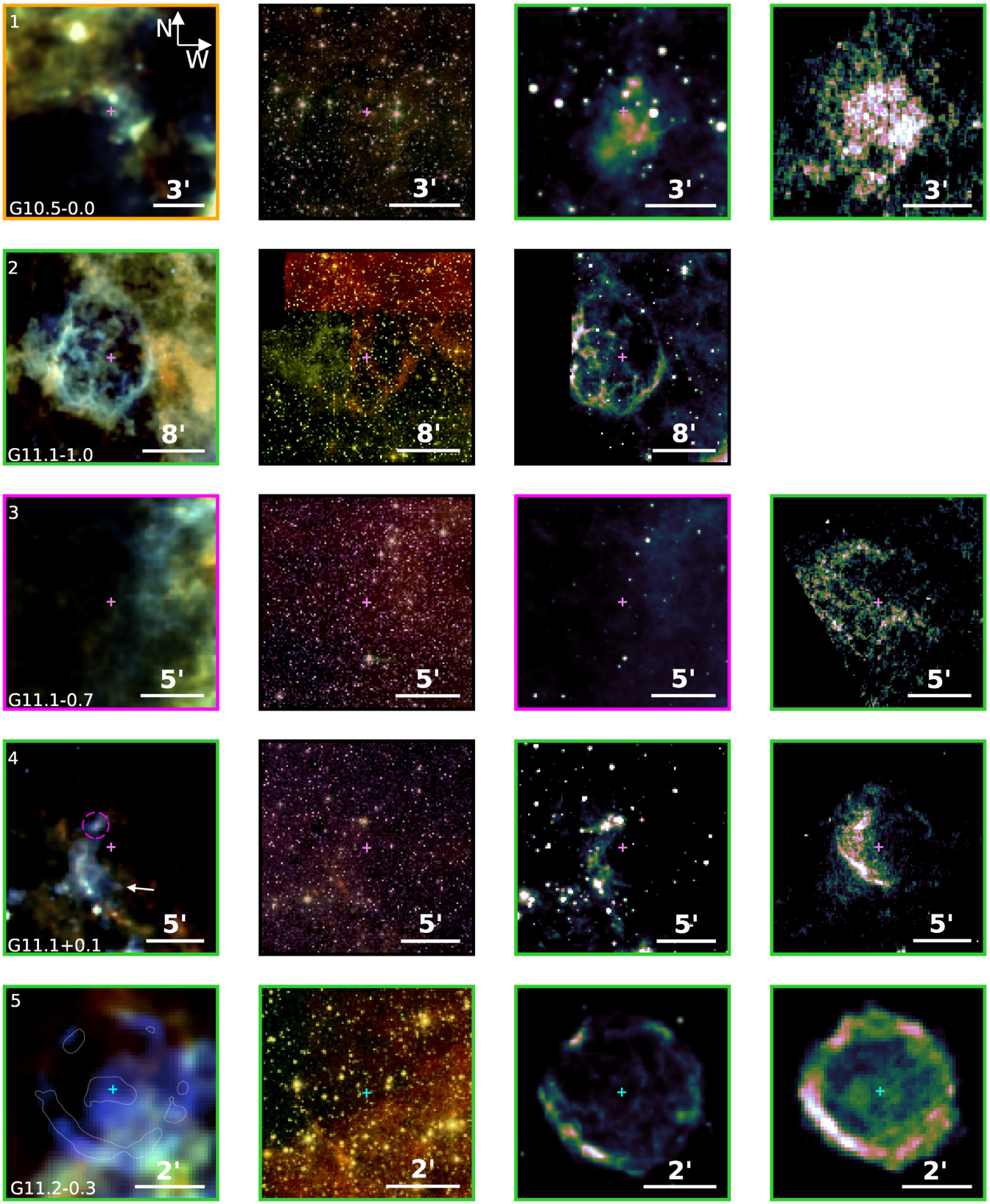

Figure A2. *First column*: *Herschel* three-colour images where colours are red = 250 μm, green = 160 μm, and blue = 70 μm. Overlaid contours are X-ray unless indicated. *Second column*: *Spitzer* IRAC four-colour images. *Third column*: *Spitzer* MIPS 24 μm images. *Fourth column*: Radio images: VLA 20 cm where $l < 48.5^{\circ}$, CGPS 1420 MHz in the range $52 < l < 192^{\circ}$, and MOST 0.843 GHz where $l > 255^{\circ}$. The border colour indicates the associated detection level as given in Table 1, where green = level 1, orange = level 2, magenta = level 3, grey = level 4, and black = unstudied. This is given for this study in the first column, R06 in the second column, and PG11 in the third column. In some panels, dashed magenta circles and white arrows indicate particular FIR dust emission features associated with the SNR. X-ray contours are overlaid onto the *Herschel* image of G11.2–0.3.

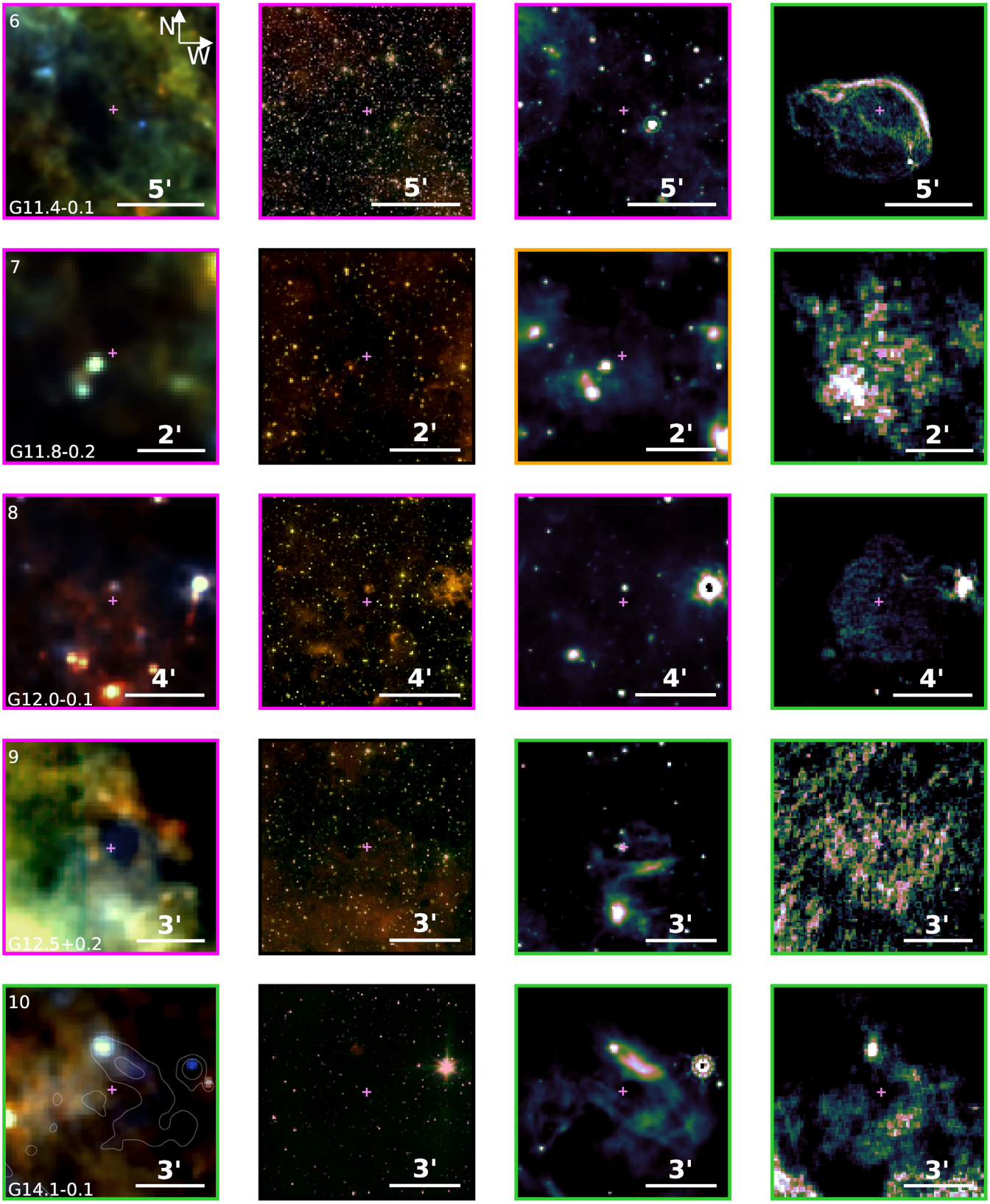

Figure A2. – *Continued*. MIPS 24μm contours are overlaid onto the *Herschel* image of G14.1-0.1.

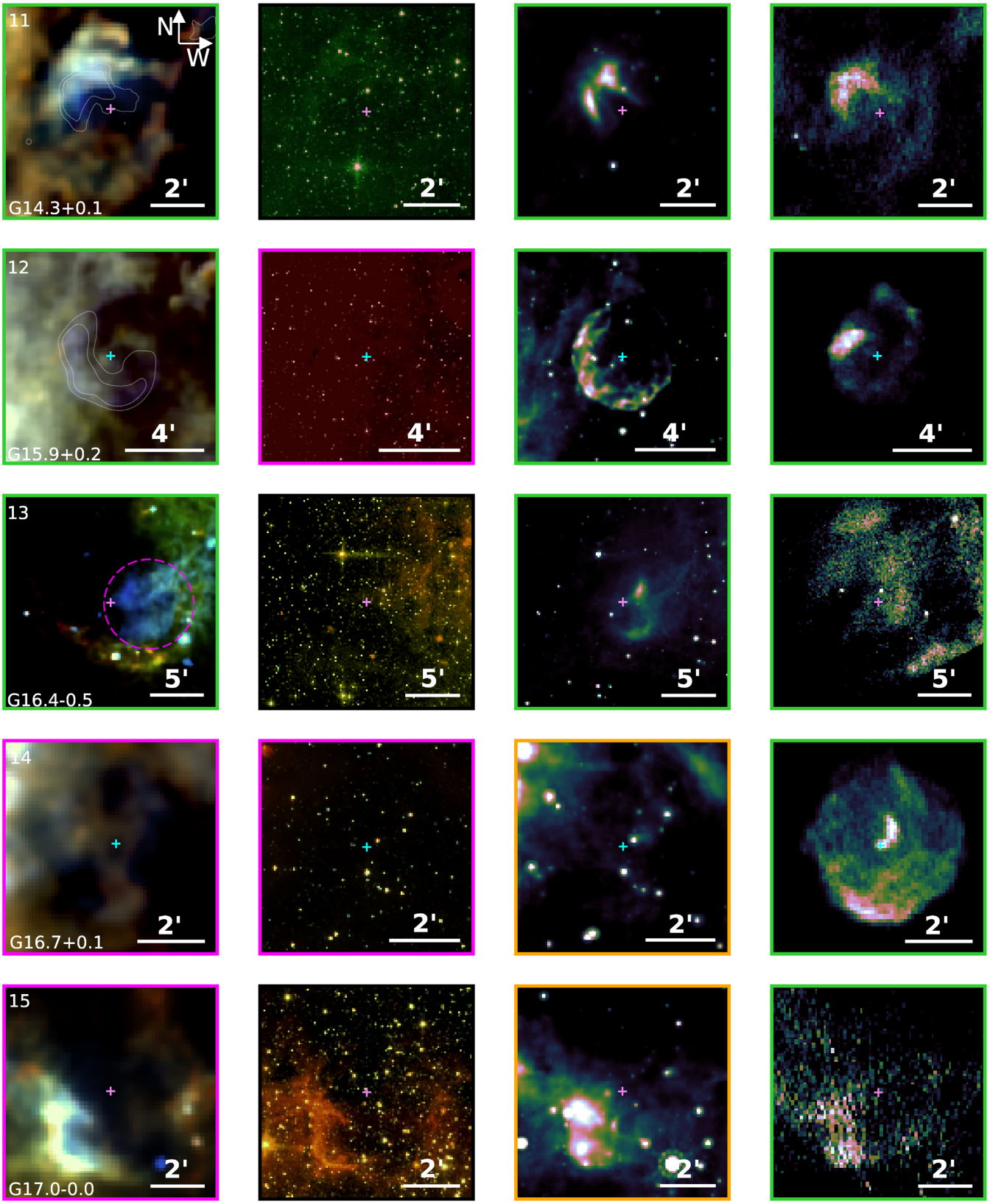

Figure A2. – *Continued.* Radio contours are overlaid onto the *Herschel* image of G14.3+0.1 and X-ray contour onto the *Herschel* image of G15.9+0.2.

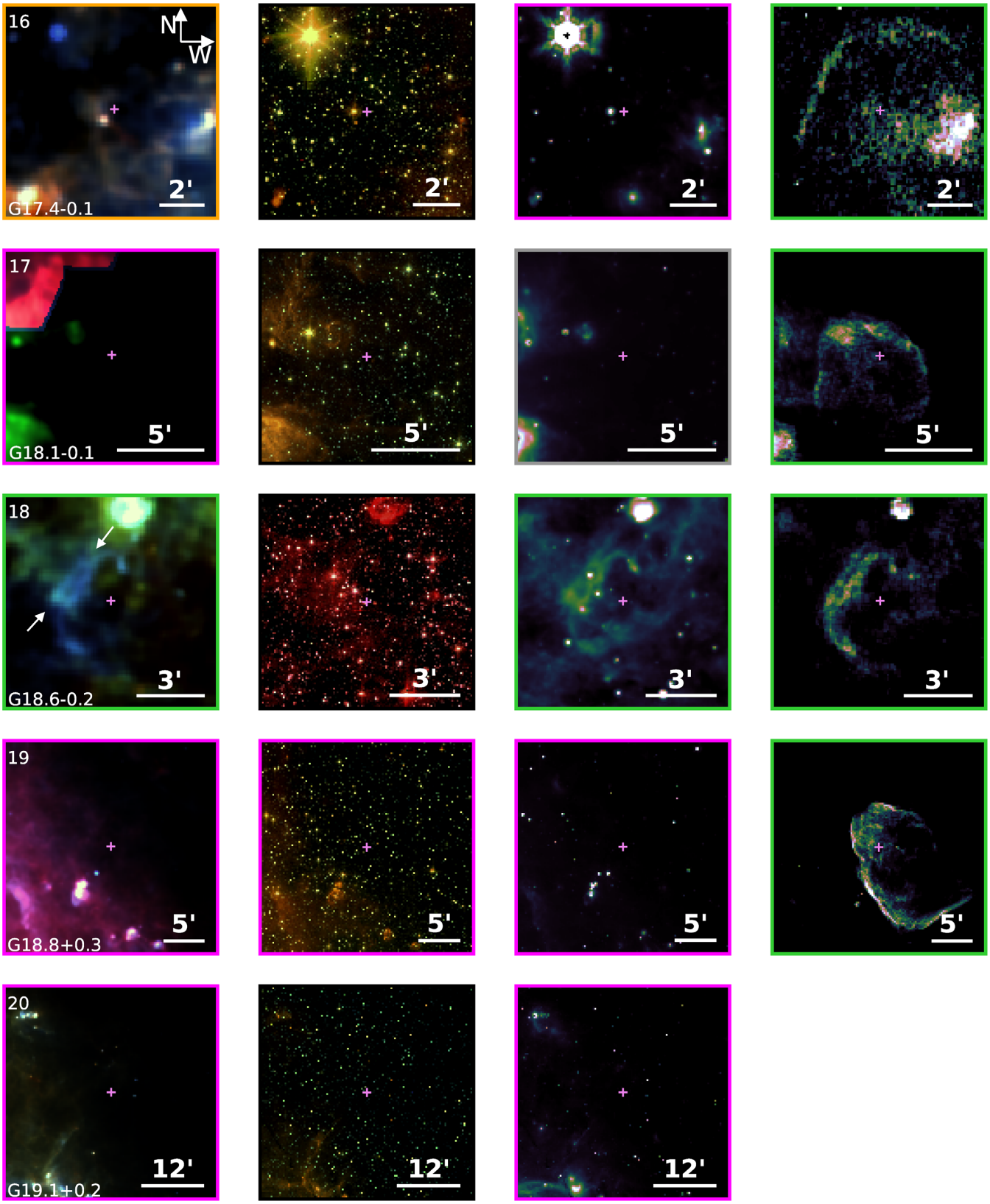

Figure A2. – *Continued*

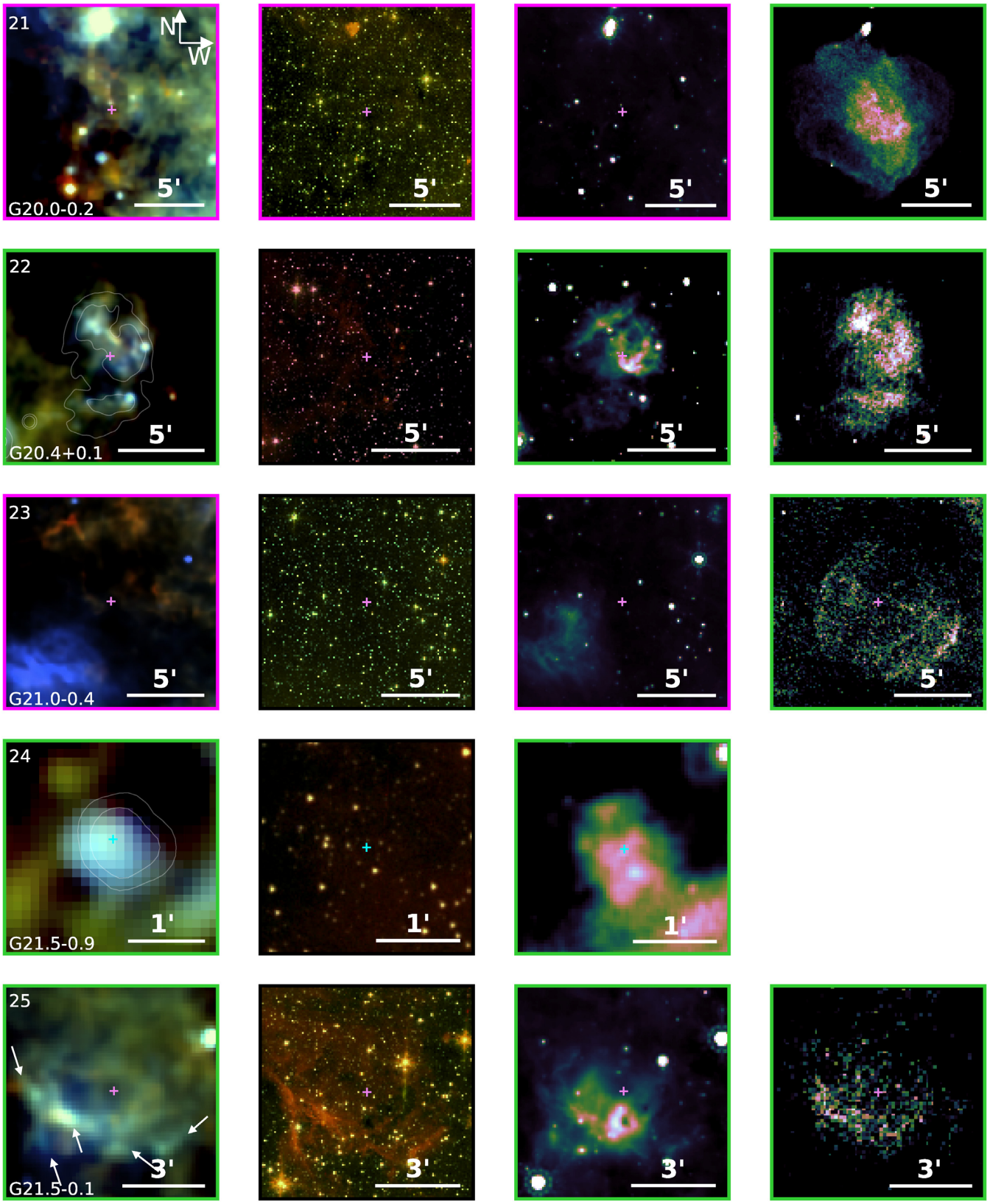

Figure A2. – *Continued*. Radio contours are overlaid onthe the *Herscehel* image of G20.4+0.1 and X-ray contours onto the *Herschel* image of G21.5-0.9.

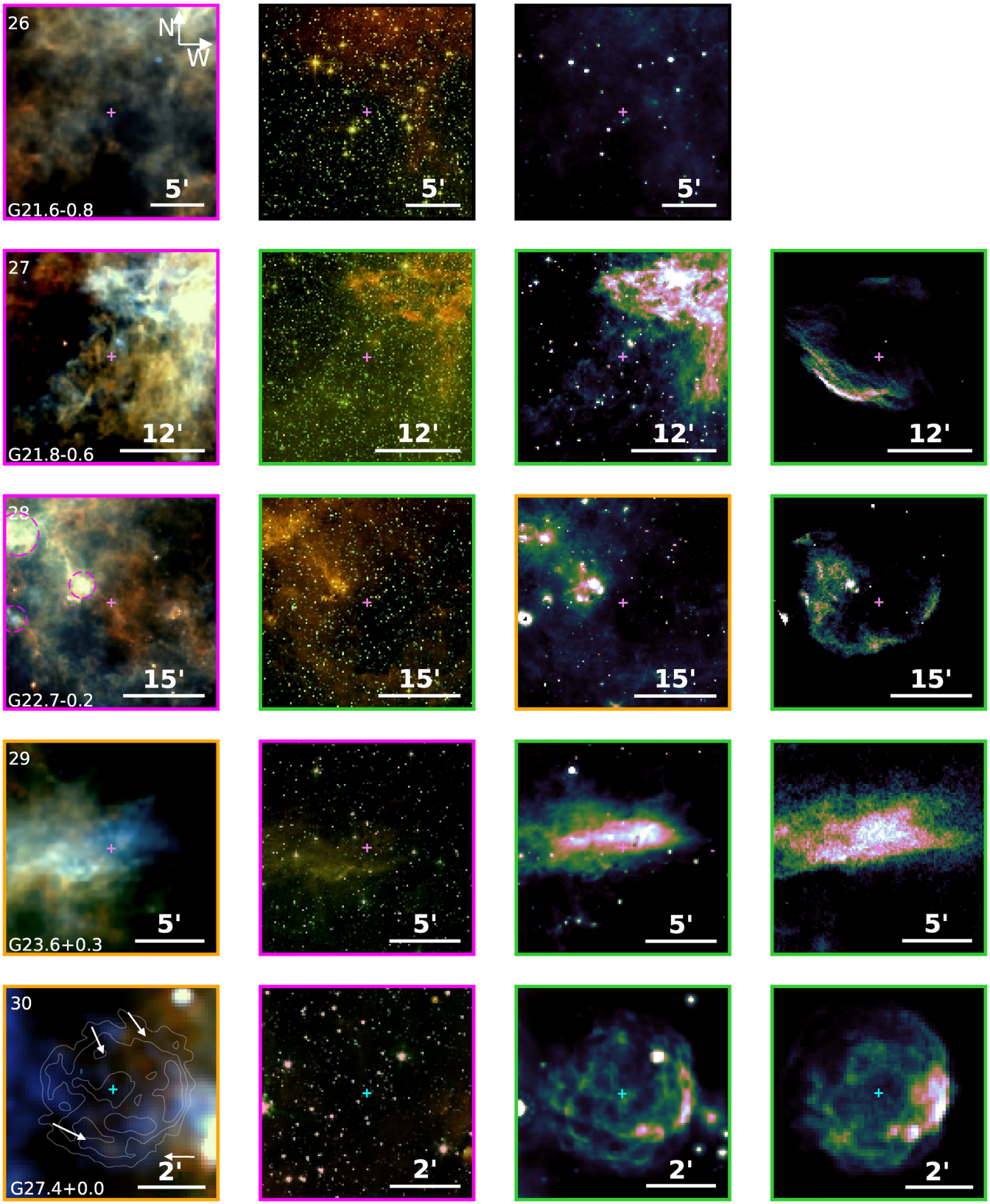

Figure A2. – *Continued*. X-ray contours are overlaid onto the *Herschel* image of G27.4+0.0.

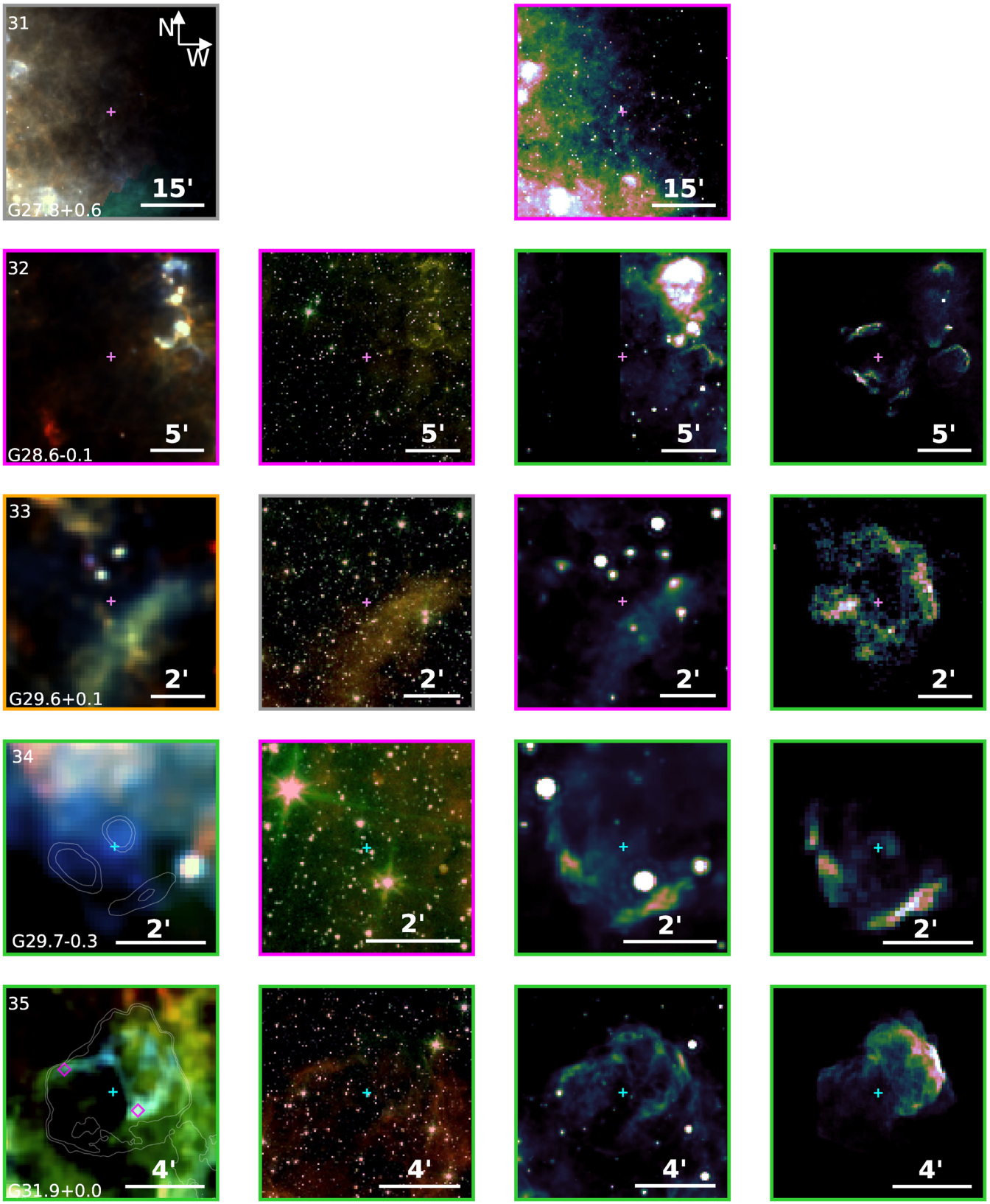

Figure A2. – *Continued*. X-ray contours are overlaid onto the *Herschel* image of G29.7-0.3 and radio contours onto the *Herschel* image of G31.9-0.0.

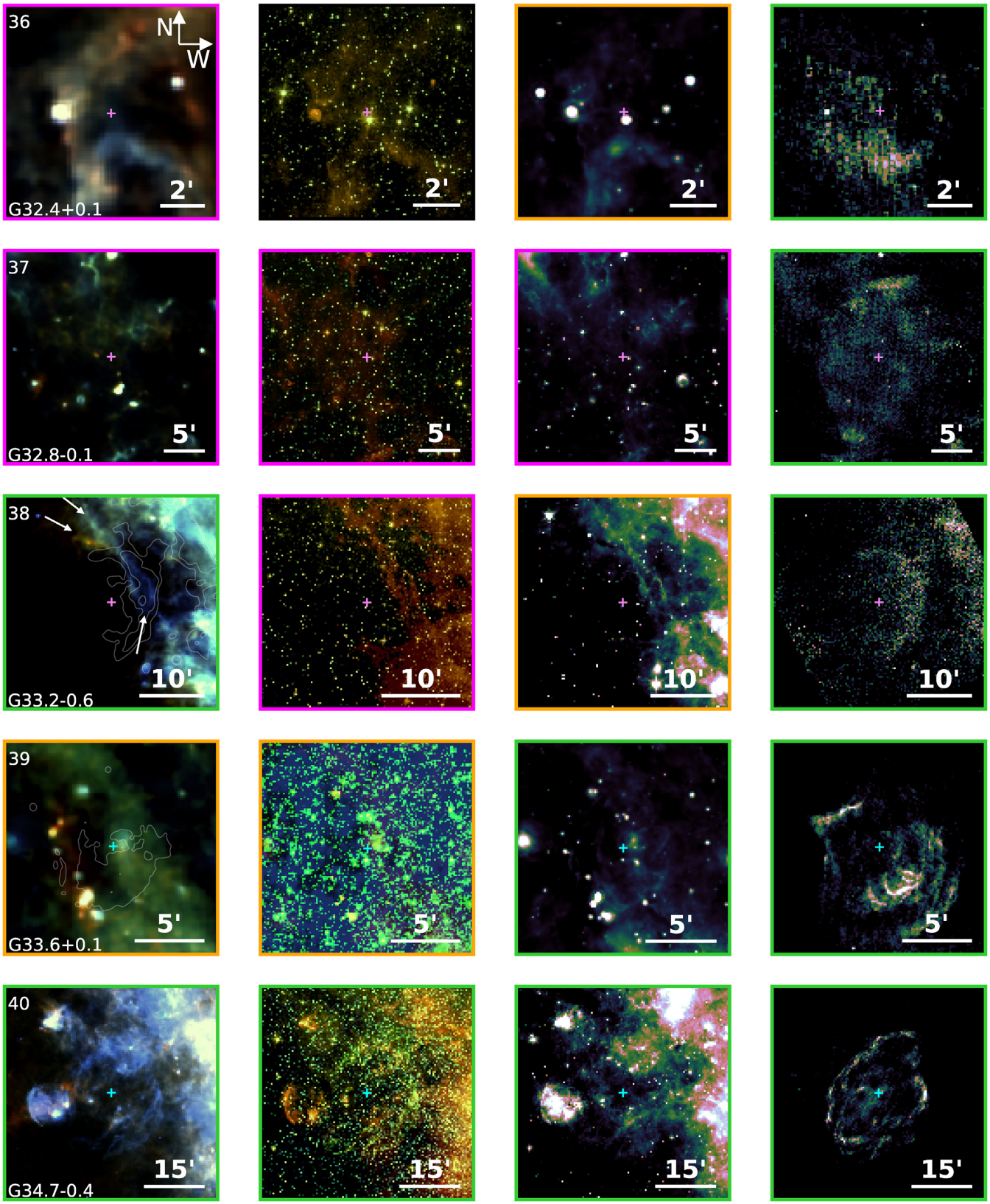

Figure A2. – *Continued*. Radio contours are overlaid onto the *Herschel* image of G33.2-0.6, and X-ray contours onto the *Herschel* image of G33.6+0.1.

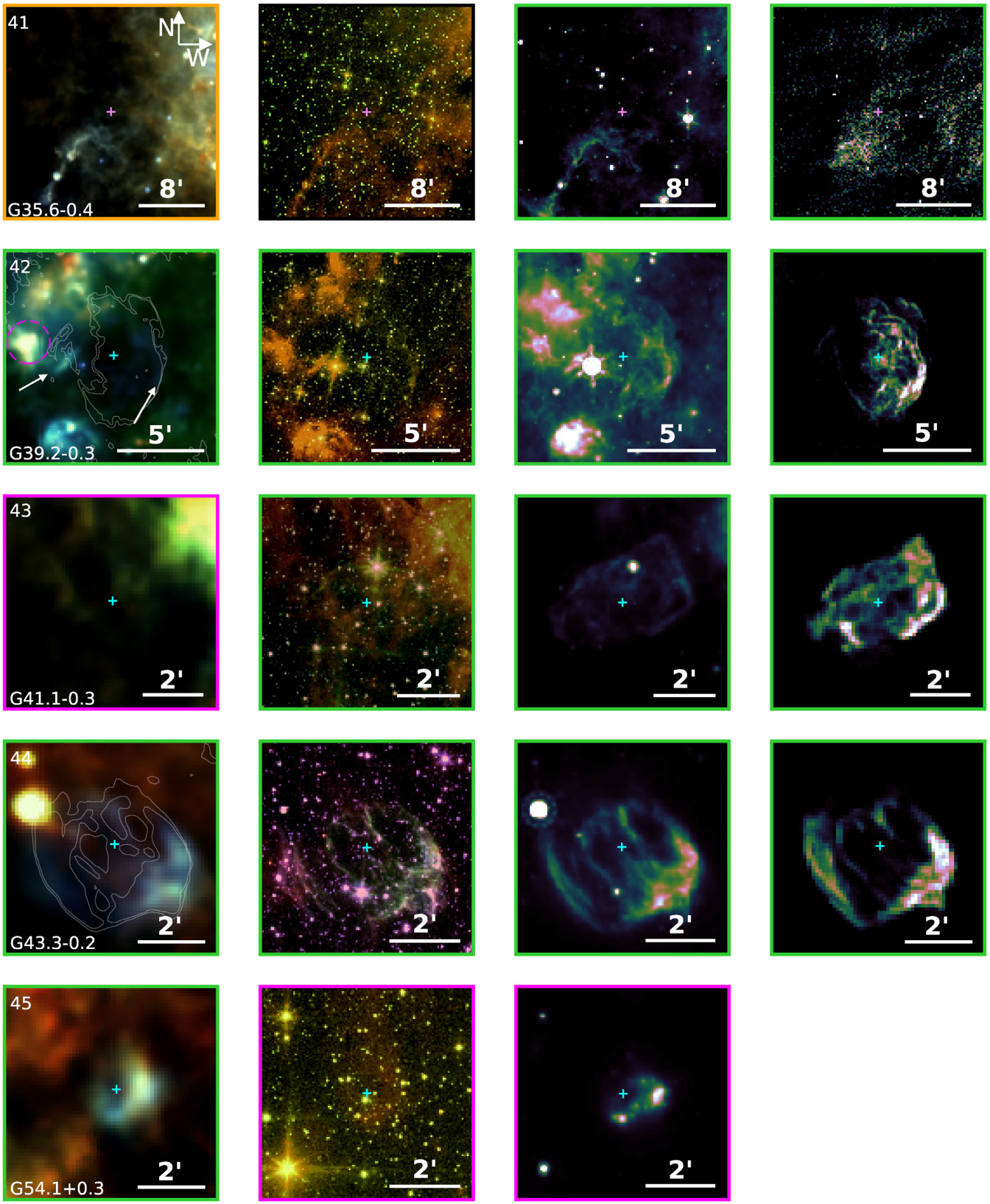

Figure A2. – *Continued*. Radio contours are overlaid onto the *Herschel* images of G39.2-0.3 and G43.3-0.2.

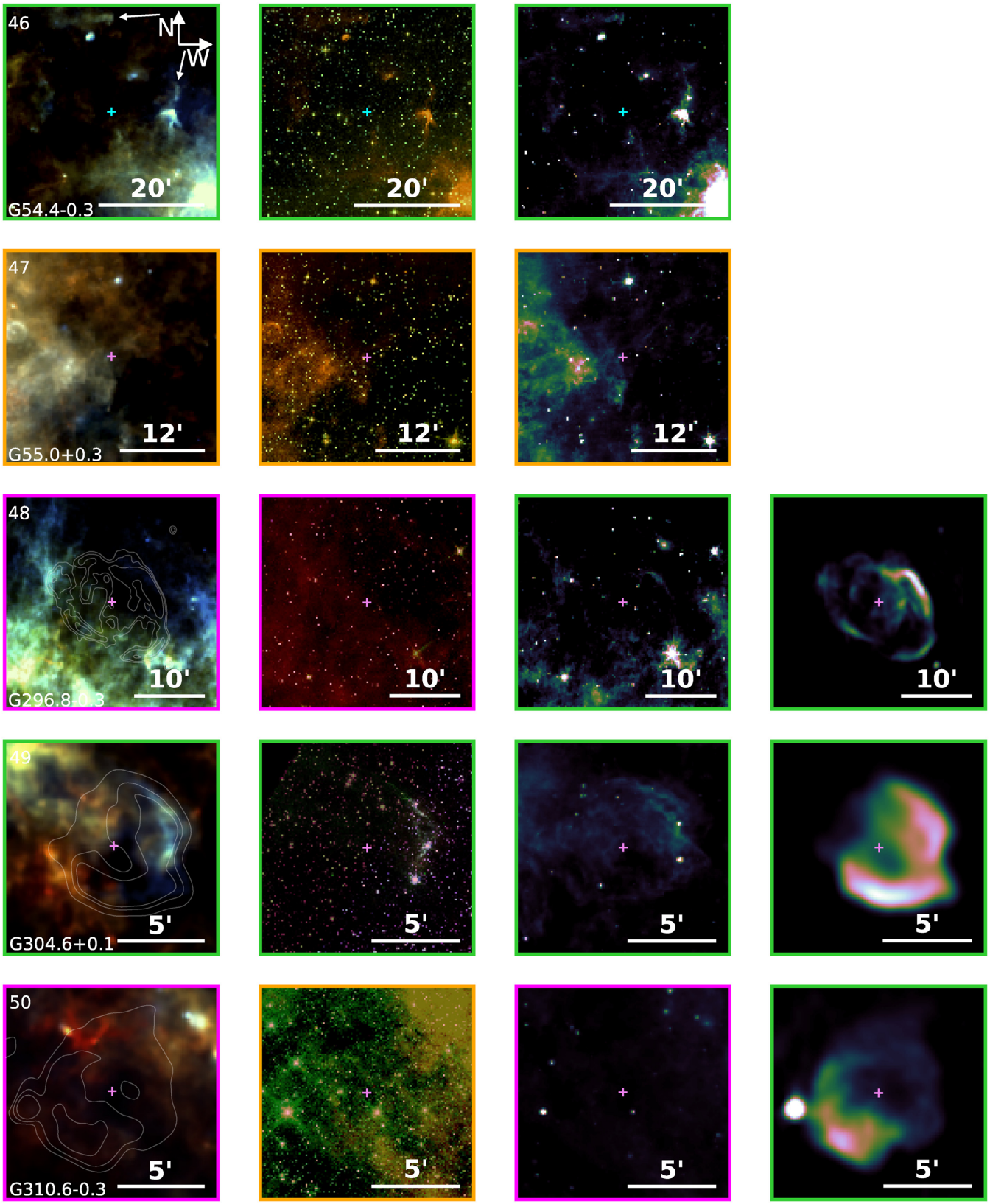

Figure A2. – *Continued*. Radio contours are overlaid onto the *Herschel* imagees of G296.8-0.3, G304.6+0.1, and G310.6

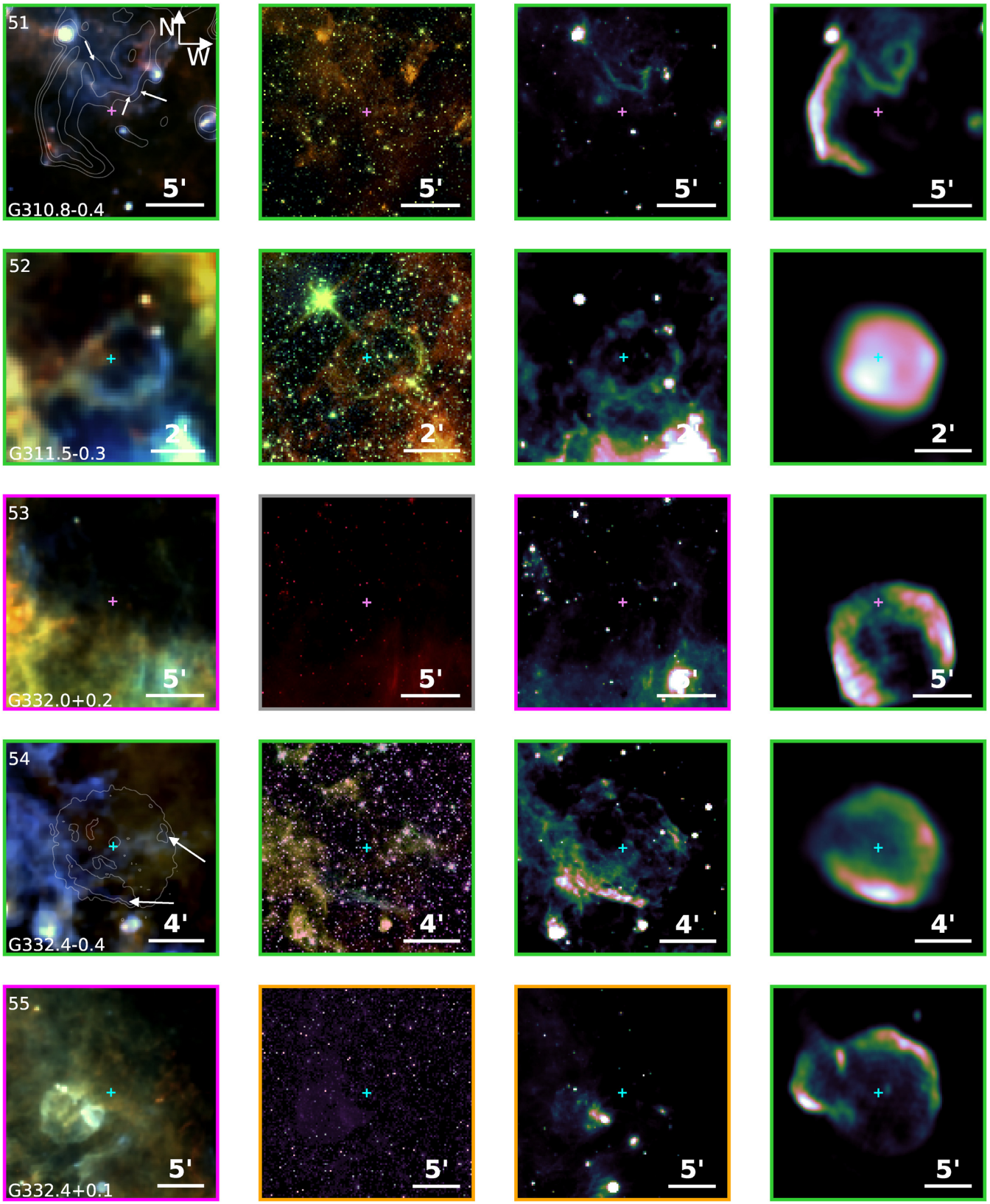

Figure A2. – *Continued.* Radio contours are overlaid onto the *Herschel* image of G310.8-0.4, and X-ray contours onto the *Herschel* image of G332.4-0.4.

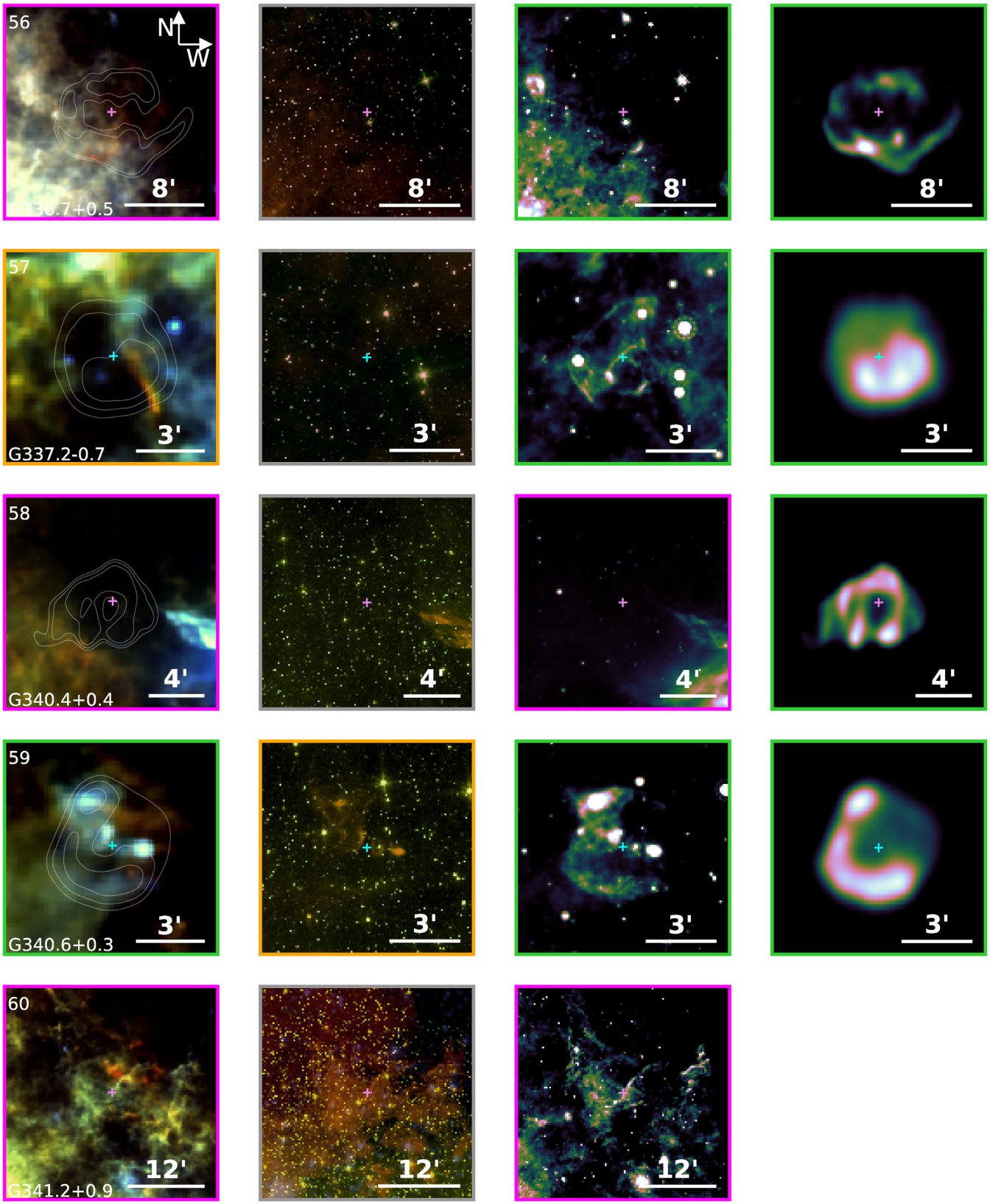

Figure A2. – *Continued*. Radio contours are overlaid onto the *Herschel* images of G336.7+0.5, G337.2-0.7, G340.4+0.4, and G340.6+0.3.

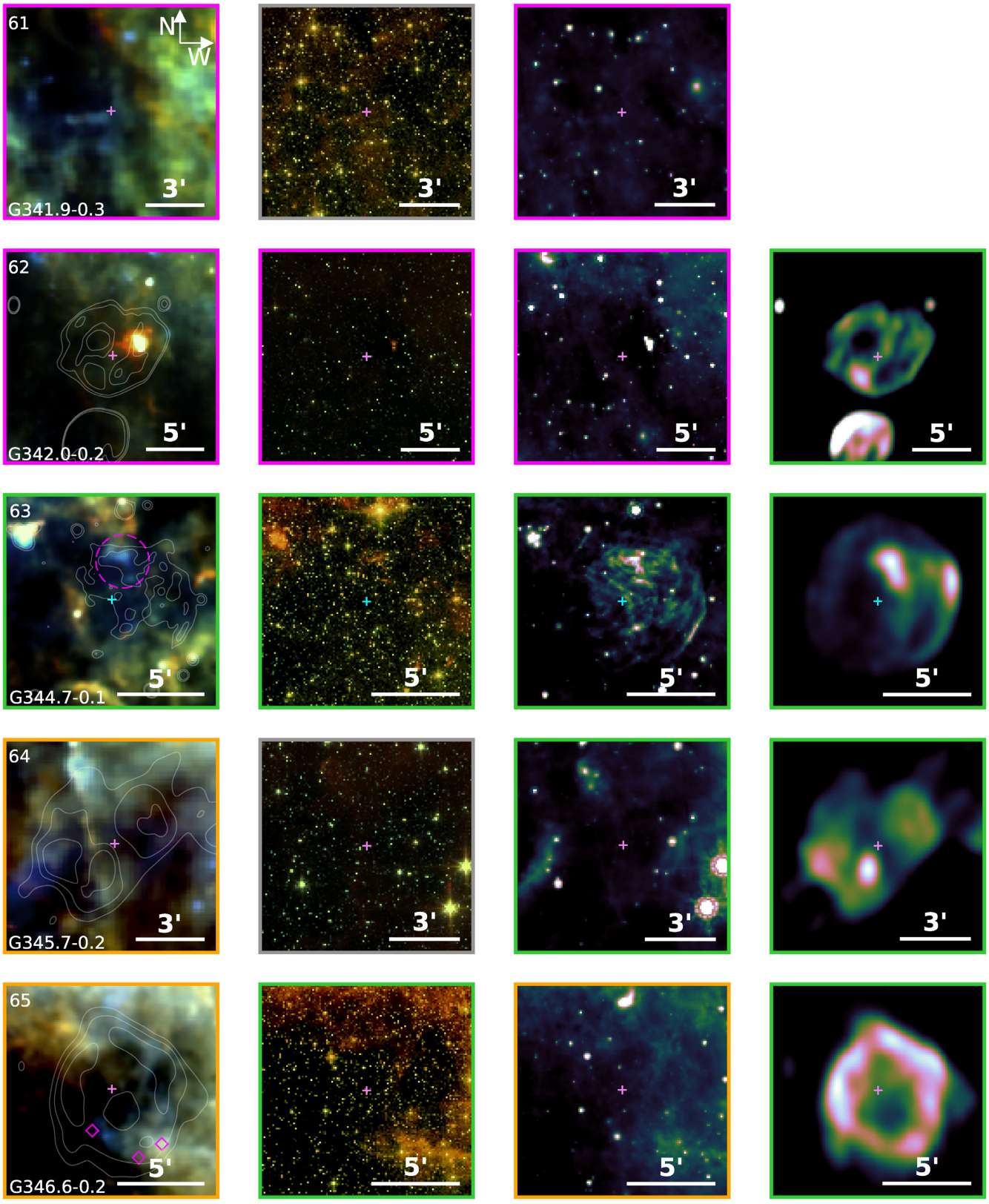

Figure A2. – *Continued*. Radio contours are overlaid onto the images of G342.0-0.2, G345.7-0.2, and G346.6-0.2. MIPS 24 μm contours are overlaid onto the *Herschel* image of G344.7-0.1.

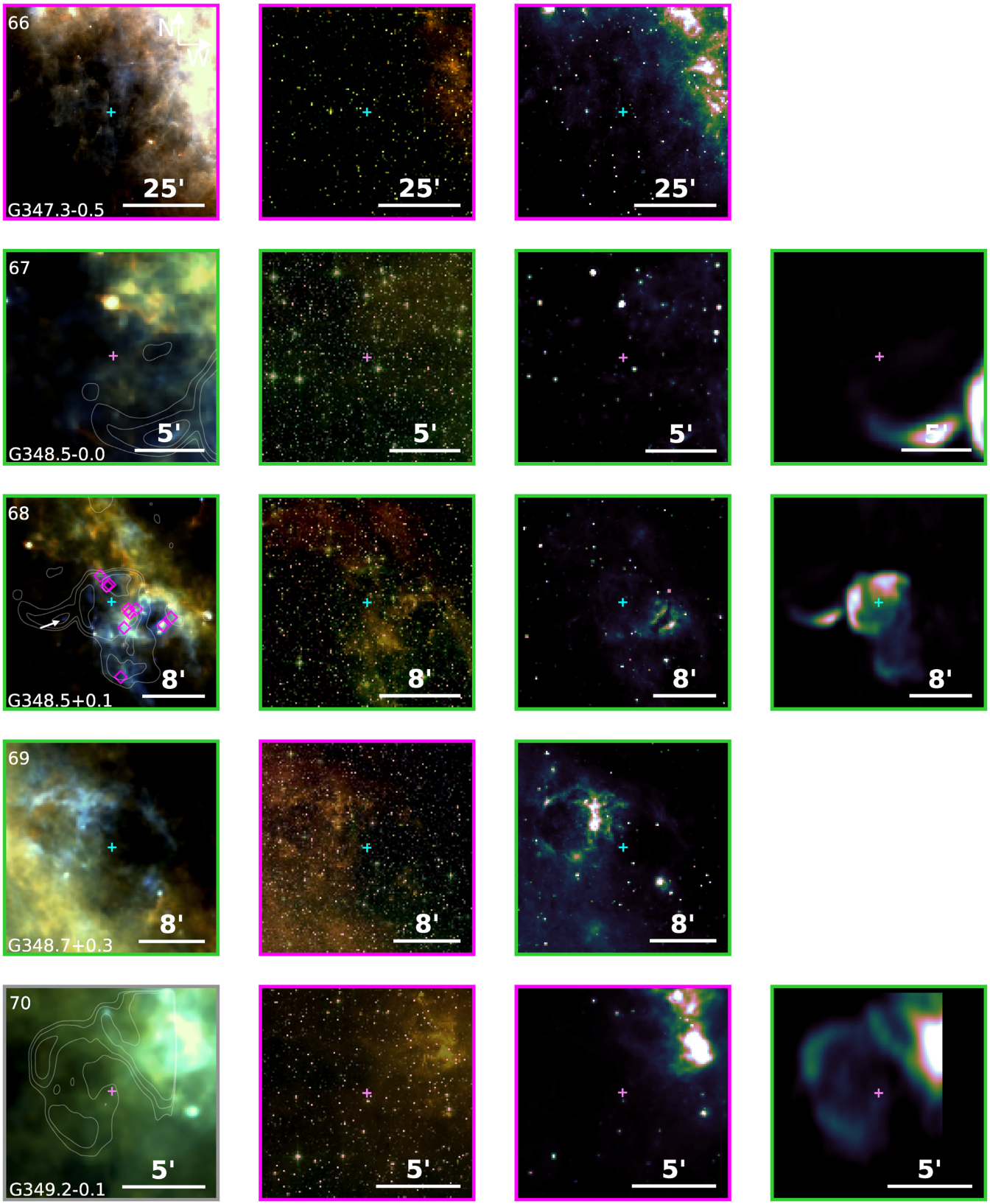

Figure A2. – *Continued*. Radio contours are overlaid onto the *Herschel* images of G348.5-0.0, G348.5+0.1, and G349.2-0.1.

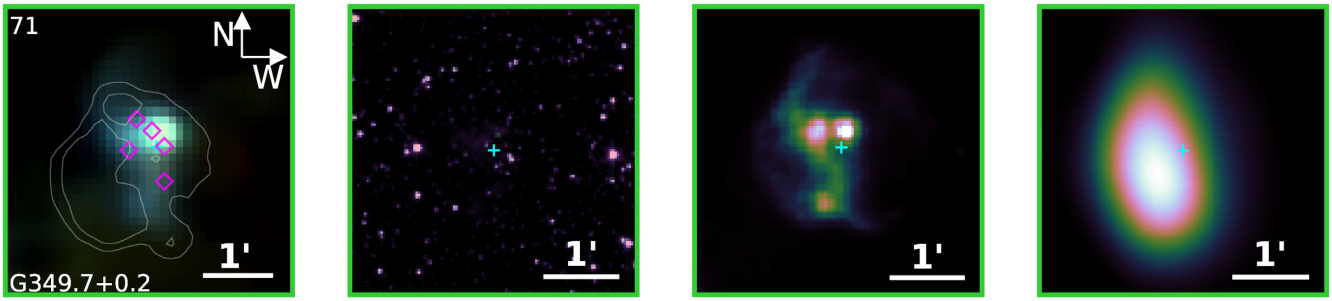

Figure A2. – *Continued*. X-ray contours are overlaid onto the *Herschel* image of G349.7+0.2.

APPENDIX B: PPMAP RESULTS

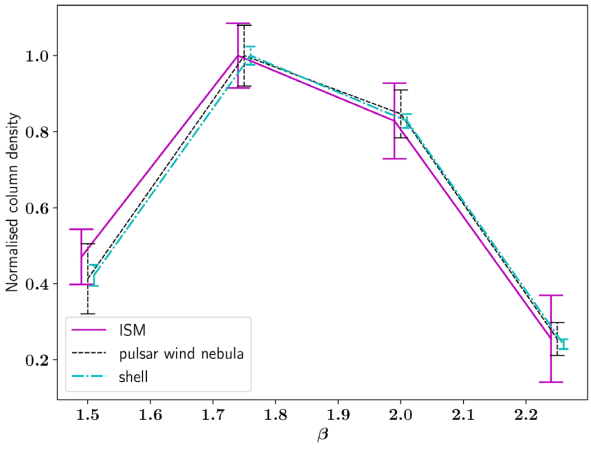

(a) G11.2–0.3

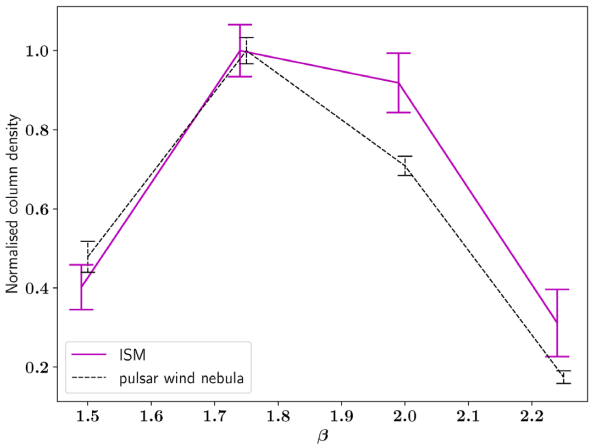

(b) G21.5–0.9

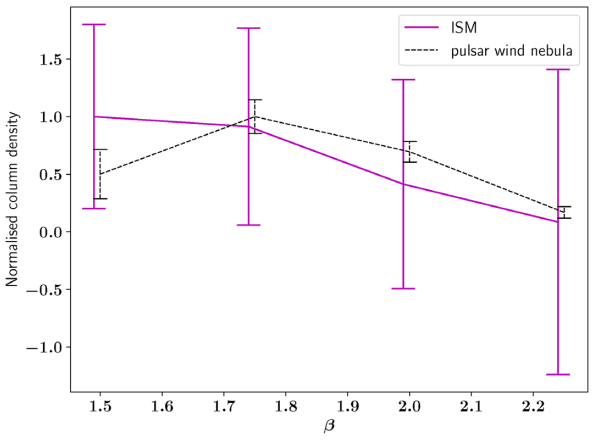

(c) G29.7–0.3

Figure B1. Estimated column density with β using a Gaussian β prior with mean 1.9 and $\sigma = 0.25$. (a) G11.2–0.3: for the PWN, the shell, and the ISM dust; (b) G21.5–0.9: PWN and ISM; and (c) G29.7–0.3. The column density in each region is normalized by dividing by the peak column density for comparison purposes. As we have low signal-to-noise ratio for these SNRs, we cannot constrain β. PPMAP is effectively returning the Gaussian posterior for these three PWNe.

This paper has been typeset from a TEX/LATEX file prepared by the author.